8-2018

Kinematics of Plate Rotation on Europa: Case study in Argadnel Regio

Chad Aaron Melton
University of Tennessee, cmelton3@vols.utk.edu

To the Graduate Council:

I am submitting herewith a thesis written by Chad Aaron Melton entitled "Kinematics of Plate Rotation on Europa: Case study in Argadnel Regio." I have examined the final electronic copy of this thesis for form and content and recommend that it be accepted in partial fulfillment of the requirements for the degree of Master of Science, with a major in Geology.

Joshua P. Emery, Major Professor

We have read this thesis and recommend its acceptance:

Devon M. Burr, William M. Dunne, Louise M. Prockter

Accepted for the Council:
Dixie L. Thompson

Vice Provost and Dean of the Graduate School

(Original signatures are on file with official student records.)

Kinematics of Plate Rotation on Europa: Case study in Argadnel Regio

A Thesis Presented for the
Master of Science
Degree
The University of Tennessee, Knoxville

Chad Aaron Melton
August 2018

Dedication

For my wife Alison…

ACKNOWLEDGEMENTS

First and foremost, I would like to thank Josh Emery for opportunity to work under his guidance for both my undergraduate and graduate research, and for the many lessons that have transformed me into a scientist. I would like to thank my committee – Drs. Devon Burr, Bill Dunne, and Louise Prockter for their superb guidance and for helping make project much better. This work would not be possible without your input. I would like to offer sincere gratitude to the members of the Europa Tectonics group lead by Louise Prockter including: Wes Patterson, Simon Kattenhorn, Geoff Collins, Katie Cooper, and Alyssa Rhoden for their valuable feedback and suggestions for this project. I would like to also thank past and current members of the EMERGE research group as well as other professors and staff from the University of Tennessee for their knowledge and support including Bob Hatcher, Andrew Wunderlich, Nancy Meadows, Jeff Moersch, The Cams, Audrey Martin, The Europa Class Cohort, Abigail Harmon, Nick Stamper, Mike Lucas, Jeff Reinbolt, Dibyendu Mukherjee, Sheng Hu, Angie Staley, Melody Branch, Terresa Parrot, Rita Reagan, and Henry Simpson. I would like to sincerely thank the Earth and Planetary Sciences students who I have been fortunate to know throughout my time at UT with the department.

I would like to offer thanks to F.L. Divine, Jeff Sipe, Pandit Charenjit Chatur Lal, Mike Seal, Bruce Hampton, Nicole Siuti, Salman Khan, James Sousa, and Richard Berendzen This would not have been possible without your inspiration, friendship, lessons, and guidance. I would like to thank my family for their encouragement and providing interesting experiences that made me curious about the universe that find ourselves a part of. Finally, I would like to thank my wonderful wife Alison for hanging in there with me over the last 4.5 years with high spirits. Alison has stuck with me from the chemical formula of tourmaline, to helping me edit my thesis. I am forever grateful for your love and support.

ABSTRACT

Results of recent tectonic reconstructions on the Galilean moon, Europa, have displayed plate-like motions and rotation. Visual analysis of an area in Argadnel Regio suggests similar tectonic behavior in Europa's past with a significant amount of rotation. These rotations appear to be analogous to kinematic behavior of rotating terrestrial microplates. Plate rotation in Argadnel Regio may be driven by either of two mechanisms: subsurface shear flow (i.e. originating from convective forces) or lateral forcing from bounding plates (e.g. edge-driven). The location of the instantaneous axes of rotation (IAR), the axis that passes through the point of instantaneous zero velocity, can be used to assess the driving mechanism of plate rotation. IARs located on the boundary of a rotating plate suggest laterally forced rotation. IARs located away from plate boundaries are indicative of rotation driven by shear flow at the interface of the lithosphere and asthenosphere. The hypothesis motivating the work presented here is that rotation in Argadnel Regio is driven by shear flow within the ice shell. This hypothesis is tested by measuring locations of IARs on Galileo Solid State Imaging Camera images of Argadnel Regio. Cross-cutting relationships were examined to obtain the sequence of plate motions to reconstruct section of Argadnel Regio using GPlates. The reconstruction was used to extrapolate locations of IARs for a circular feature (CF) composed of a group of plates that rotated collectively ~ 40°. IARs detected away from plate boundaries of the CF suggest that rotation was due to shear flow within the ice shell. However, the IARs associated with two plates in the interior of the CF found on plate boundaries suggest that some "edge-driven" forces are responsible for the rotation and rotation related deformation due to location of IARs on plate boundaries. A plate bordering the (CF) appears to be completely "edge-driven" by the rotation of CF due to the detection of IARs on the plate boundary. These results suggest that rotation in Argadnel Regio was driven from edge-driven forces and forces originating in the subsurface. The detection of convective driven tectonics makes Argadnel Regio a landing site candidate for future missions.

TABLE OF CONTENTS

LIST OF TABLES

LIST OF FIGURES

1. INTRODUCTION

The Galilean satellite, Europa, is one of the most geologically interesting and tectonically active bodies in the Solar System. The first Voyager images of Europa in 1979 displayed a unique surface that appeared to have "little or no record of intense bombardment" and "a system of overlapping bright and dark linear features" (Smith et al. 1979). In the 1990s, the Galileo spacecraft returned even more images at higher resolution, but a malfunction of Galileo's high-gain antenna resulted in only approximately 10% of Europa's surface being imaged at resolutions appropriate to interpret surface geology (Belton et al. 1996).

The relatively young (40- 90 million years) (Bierhaus et al., 2009), icy surface of Europa is riddled with tectonic features including: dilation bands, lenticulae, chaos terrain, double ridges, convergent zones, and, most recently, inferred subduction or subsumption zones (e.g., Kattenhorn and Hurford 2009, Kattenhorn and Prockter 2014). Galileo's magnetometer detected an induced field emanating from Europa (Khurana et al. 1998), providing strong evidence for a liquid, briny H_2O ocean beneath Europa's complex crust with an estimated volume twice that of Earth's oceans. The presence of a subsurface ocean, sustained by diurnal tidal heating, has placed Europa as a prime candidate for investigation of extraterrestrial life in the Solar System (e.g., Kargel et al., 2000).

The majority of the heat available to drive tectonics on Europa is derived from tidal stretching resulting from Europa's eccentric orbit around Jupiter. Tidal dampening would normally drive a moon like Europa into a circular orbit, but Europa is in a Laplace resonance with Ganymede and Io, whereby Io, Europa, and Ganymede orbit Jupiter with relative periods of 4:2:1 for Ganymede, Europa, and Io, respectively. This orbital configuration leads Europa to have a forced eccentricity of 0.009, causing Europa to be continually kneaded or flexed over its 3.6-day orbital period (Peale and Lee 2002).

Continual tidal flexing causes heat to dissipate throughout the icy shell and the true silicate mantle, though the majority is thought to dissipate near the brittle-ductile transition (Sotin et al., 2009). It is suggested that hydrothermal plumes originate from geothermal vents on the silicate crust, travel to the ocean – ice interface, and eventually contribute to the surface geology (Goodman and Lenferink 2012).

Regardless of where heat dissipates, it all must travel through Europa's ice shell. Conduction, as well as solid-state convection, is a way to transmit heat to the exterior of the ice shell (Barr and Showman, 2009). It is still debated whether convection can fully drive the tectonics of the Europan icy shell (Sotin et al., 2009, Barr and Showman 2009, Nimmo and Manga 2009, Schubert et al., 2001). Solid-state convection is of particular interest due to the ability for convective currents to transmit material from the putative subsurface ocean to the surface (Rudolph and Manga 2012). A primary goal for future Europa missions is to sample material that has been in contact with the subsurface ocean. The ice shell is most likely too thick (approximately10 – 30 km) to realistically penetrate with a lander (Nimmo and Pappalardo 2003). Therefore, understanding the evolution of Europa's icy shell may be vital to future missions such as the Europa Clipper. Detecting areas that may contain material from the subsurface will ensure that possible points of interest can be investigated by orbiters and future landers.

Based on the observable geomorphology, a section of Argadnel Regio, near the equatorial-trailing hemisphere, is one of these regions of interest. Preliminary analysis of a western section in Argadnel Regio (Fig. 1) suggested that rotation of a circular feature (CF) consisting of 12 plates occurred in an anticlockwise direction with respect to the surrounding icy lithosphere. Plate rotation could be caused by edge-driven forces or shear forces associated with subsurface flow. Determining the mechanism driving rotation will provide constraints about how heat is transferred in the ice shell of this region. The mechanism that drives plate-like motion is also of interest due to the ability for convection or plumes to transport material from the subsurface to the surface. If convective related tectonics can be detected at a specific region, the region could a potential landing site for a future Europa Lander.

A useful aspect of plate rotation is that the location of the instantaneous axes of rotation (IAR) can be used to determine the mechanism driving rotation. IARs that are located on the boundary of a rotating plate and the bounding plates suggest laterally forced rotation. If the IARs are located within the bounding plates and away from the plate boundaries, the mechanism behind rotation is likely from subsurface shear flow (e.g., McKenzie and Morgan 1969). Plate rotation should cause deformation at plate boundaries and plate interiors (Lamb et al., 1989). This deformation can be expressed as tears, fractures, or pseudofaults (Schouten et al., 1993). In terrestrial oceanic settings, pseudofaults are attached to IAR on opposite sides of a rotating plates. As plates rotate,

translate, grow and/or deform, these features will follow and trace the path of the IAR's (Katz et al. 2005). Detection and geometric analysis of deformation features can be extremely useful in interpreting plate rotation mechanisms and history, especially when no magnetic data are available. These deformational features can also be useful in determining the relative duration of plate rotation.

The purpose of this thesis is to kinematically analyze the history of the motions of the pieces or plates of ice in Argadnel Regio for the purpose of determining the contribution of solid-state convection as a driving force for these motions, and hence, as a mechanism for transmitting material from the underlying ocean to the surface (Fig.1).

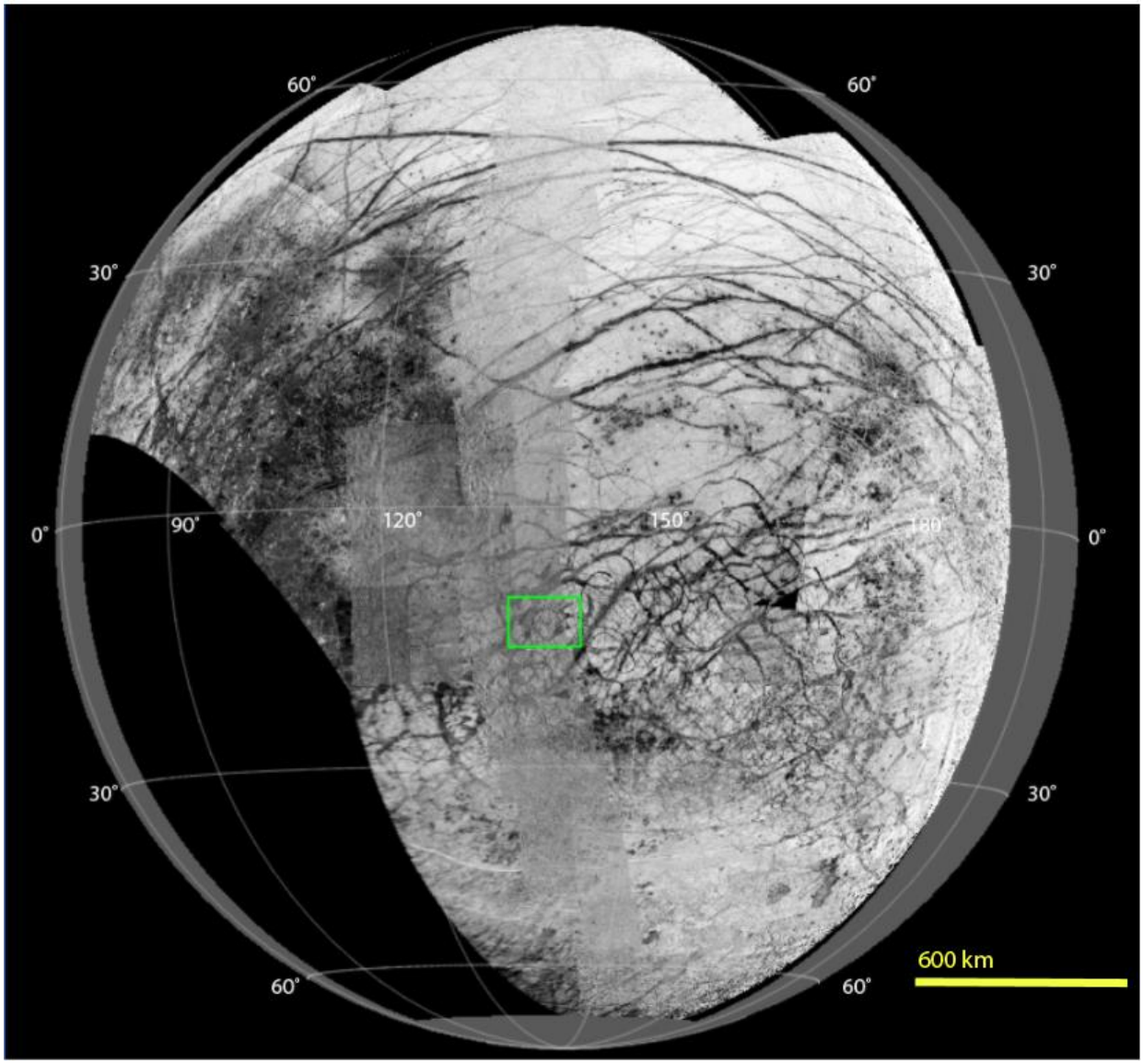

Figure 1: *Europa. The "Super Mosaic" is combined from Voyager and Galileo images. The study area in western Argadnel Regio (12.98 S, 139.86 W) is in the trailing southern hemisphere and highlighted in the green rectangle. Courtesy of Geoff Collins.*

2. BACKGROUND

2.1 Geologic Setting

Argadnel Regio is located on Europa's southern trailing hemisphere (Fig 1), south of the equator. It is one of the most complex of the imaged regions on the moon, with a network of intertwining pull-apart bands, wedge-shaped bands or "saw tooth" bands, chaos terrains, double ridges, and evidence of cryovolcanism (e.g., Prockter et al. 2017). One notable sub-region in western Argadnel Regio contains a ~100 km wide circular feature bounded by pull-apart bands and chaos terrain (Fig. 2). The CF is composed of 12 smaller plates. The CF is flanked by two large chaos terrains/intrusions, one to the northwest and one to the southeast. Several smaller units of chaos terrain are present within the concentric structure as well. The presence of chaos terrain on Europa indicates the surface has experienced stresses sufficient to break surface ice in some locations and raise the topographic relief approximately 300 meters in others (Schenk and Pappalardo 2004). Pull-apart bands surrounding the CF intersect with orthogonally oriented pull-apart bands at four large-scale triple junctions. The geometric orientation and location of offset markers immediately around the CF appear to require some amount of rotation to connect pair back together. Two examples of this is illustrated by two sets of piercing points (see Fig.2, and Appendix Fig.A).

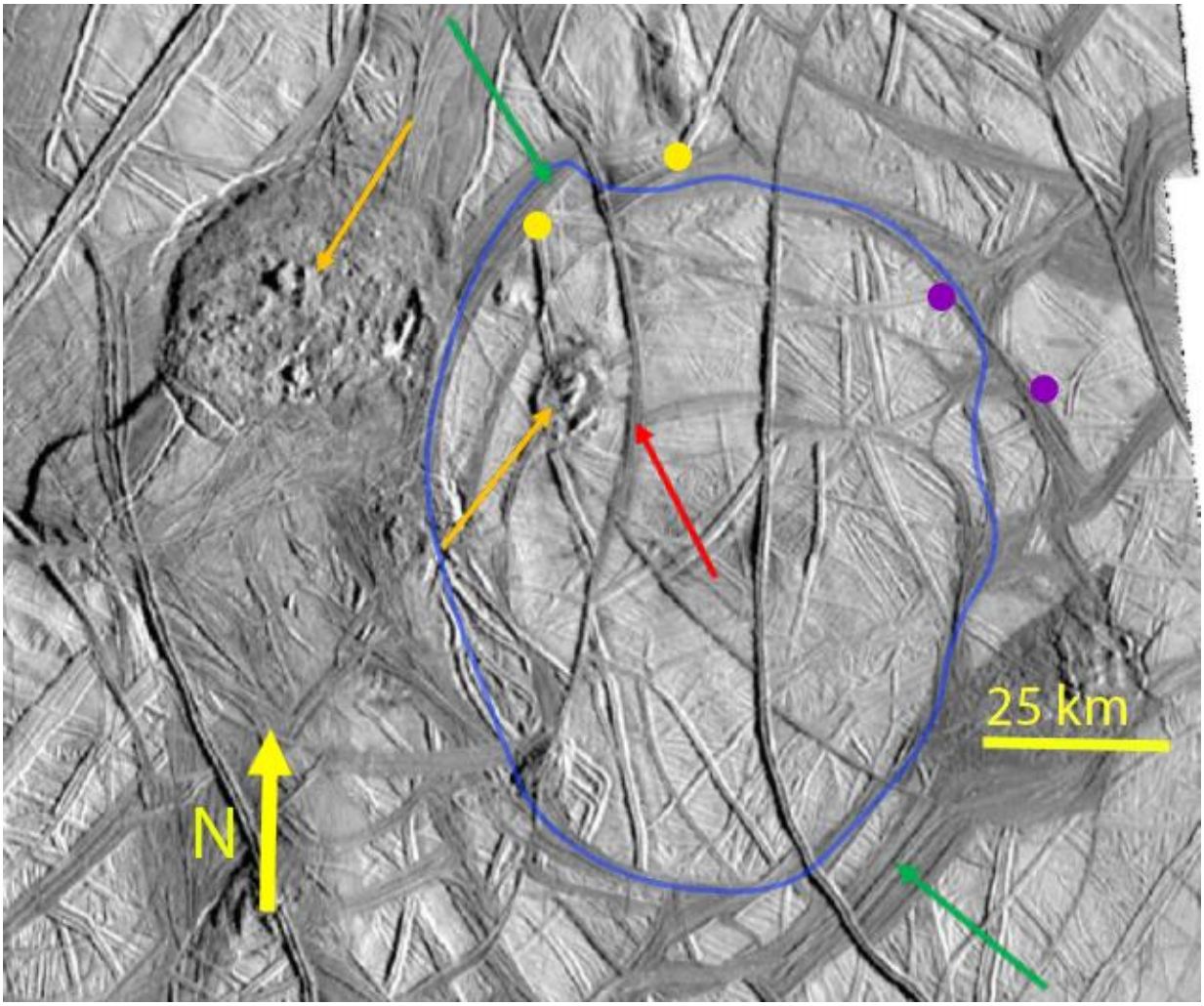

Figure 2: *Current state of the study area in western Argadnel Regio. Orange arrows point to chaos terrains. Green arrows point to pull-apart bands. Red arrows point to double ridges that appear to change into dilational bands. The circular area referred to as the "CF" is outlined in blue. Two examples of piercing point pairs are represented by yellow and purple circles.*

2.2 Terrestrial Microplate Kinematics

Study of terrestrial rotating microplates began in the early 1980s. These previous studies of microplate kinematics provide useful insights that are applicable to tectonic reconstructions of Argadnel Regio. The "pinned block" model (PBM) and "floating block" model (FBM) were first described by McKenzie and Jackson (1983), McKenzie and Jackson (1986), and then refined by Jackson and Molnar (1990). Further exploration into how plate shape and aspect ratio affect plate rotation was conducted by Lamb (1987), and Lamb (1988). The FBM places instantaneous axis of rotation (IAR) within the bounding plate, and records ubiquitous slip. Rotation rates that occur with the FBM are expected to be more slowly than the PBM. The PBM places IARs on the margin of the plate boundary, records minimal slip, and rotates much more rapidly than the FBM. The PBM eventually developed into what is known as the "edge-driven" rotation model. The model for edge-driven rotation is illustrated by a simple single gear, a double gear, or a combination, depending on angular velocity and whether extension has occurred (Schouten et al. 1993) (Fig. 3). Terrestrial microplate rotation is a useful analog to Europan plate rotation due to similarities of the angle of rotation (~30-40) relative to binding that have been recorded on both bodies. Kinematic analysis seems especially appropriate to Europa due to the fact that many physical parameters used in mechanical analysis remain enigmatic.

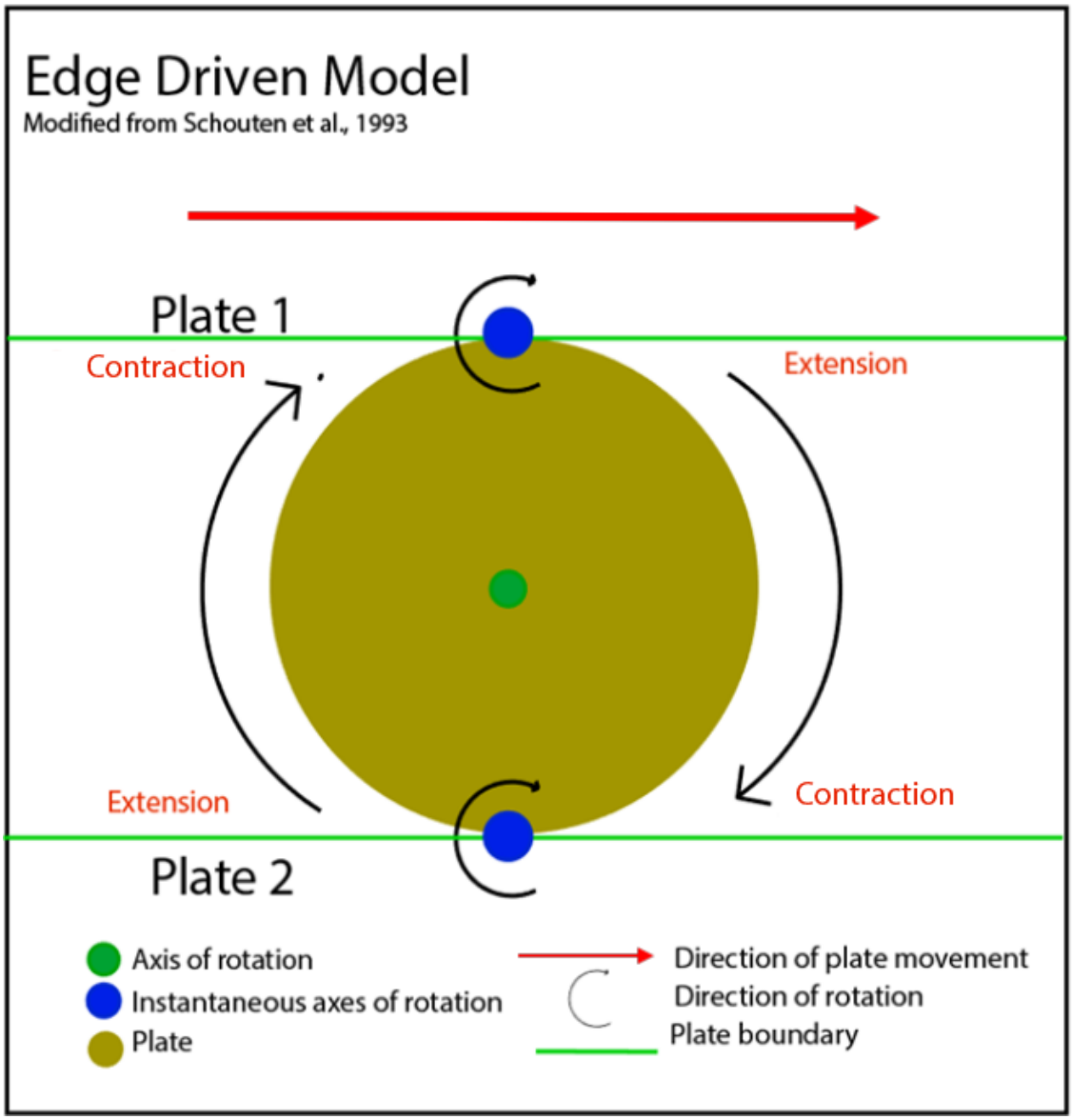

Figure 3: *Idealized simple gear model (Schouten, 1993). Blue circles represent IARs. The green circle represents the vertical axis. Red arrows represent motion of bounding plate. Location of contractional and extensional features are useful in determining locations of IARs.*

In rotational kinematics, the IAR is the axis that passes through the point of instantaneous zero velocity (e.g., intersection of a road with a tire not experiencing slip). By locating instantaneous axes of rotation, it is possible to distinguish among models for microplate dynamics and thereby gain insight into the mechanisms that drive rotation. IARs that are located on the boundary of a rotating plate and bounding plates suggest laterally forced rotation. In this situation, the microplate is affixed or pinned in between some configuration of bounding plates and rotation occurs due to forces at lateral boundaries produced by movement of the binding plates. This edge-driven type of movement is essentially driven at instantaneous poles. (McKenzie and Jackson 1983, Neves et al., 2003). IARs located at a distance within plates bounding a microplate (i.e., exterior to the rotating microplate itself) indicate rotation is occurring due to shear flow within the subsurface of the ice shell. The FBM places the IAR at some distance within bounding plates. Physically, this type of rotation occurs when a plate exists within a shear flow. The plate is rotated by a torque produced on the plate boundary (Crummet 1994, Lamb et al., 1987).

An IAR's location is based on the relationship between angular velocity and translational velocity. First, if angular velocity and translational velocity are equal, an IAR will be located directly on the boundary of the rotating body (i.e., the intersection of a tire with the road when there is no slip occurring) (Reinbolt 2013). Geologically, this situation occurs due to laterally forced or edge-driven rotation. Second, if angular velocity is less than translational velocity, IARs will be located exterior to the rotating body (i.e., a car skidding while decelerating) (Crummet 2004). A terrestrial geologic analog to this occurrence would be related to rotating plates or blocks within a shear zone. Lastly, if angular velocity is greater than translational velocity, an IAR would be located with some distance within the rotating body (i.e., tire on road that is slipping while rotating) (Reinbolt 2013). Geologically, an interiorly located IAR has not been considered terrestrial microplate rotation models (e.g., Schouten et al., 1993).

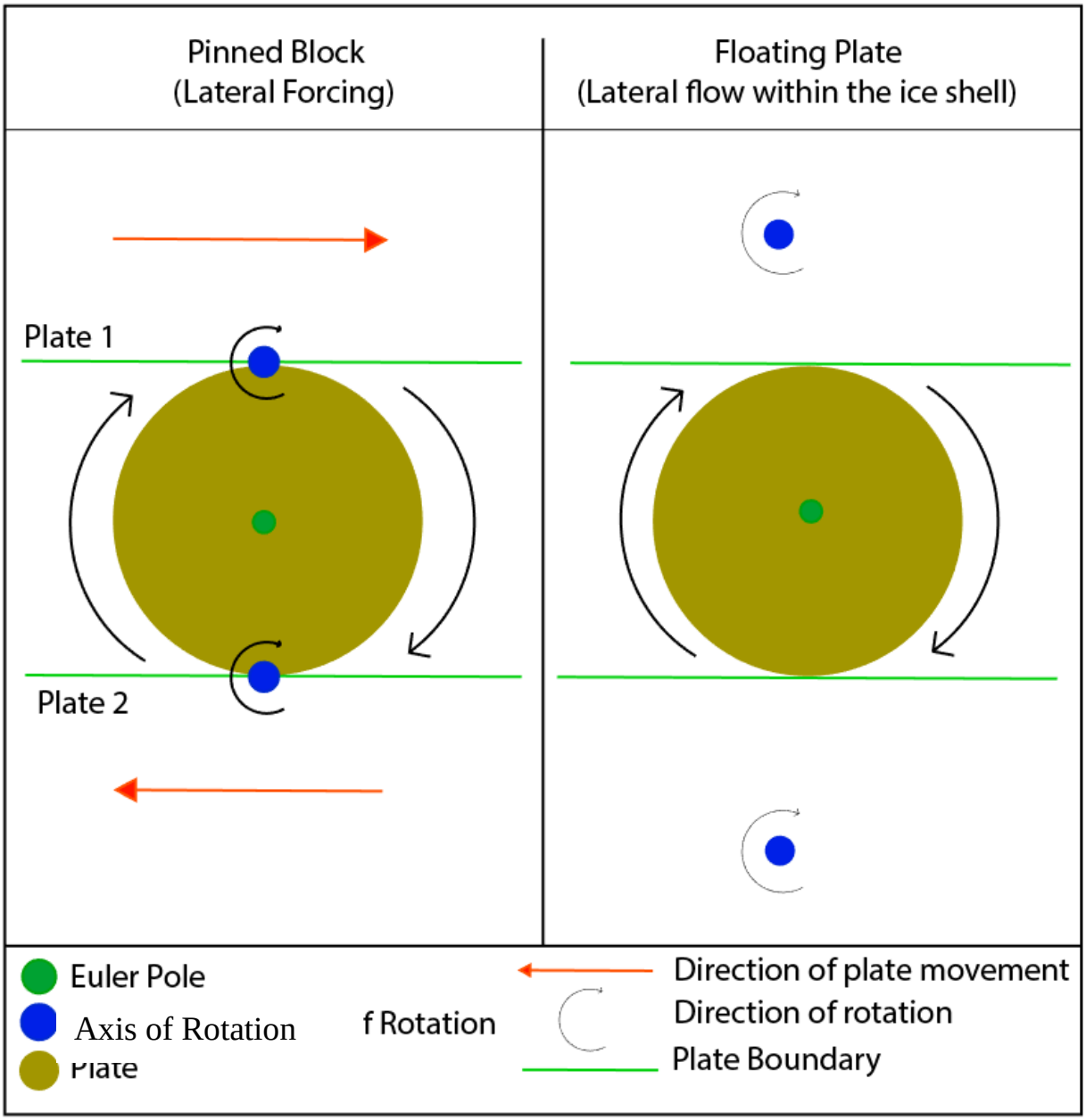

Figure 4**:** *Modified from Schouten et al., 1993. Idealized models for the two end members of microplate rotation. Left: IARs located on boundary of microplate and bounding plate indicate lateral forcing. Right: IARs located within bounding plate suggest rotation occurs from lateral flow within the ice shell.*

The application of a single or double gear model should, in theory, produce contractional and extensional features on a rotating plate at locations near an IAR (Schouten et al., 1993). Therefore, if a plate is rotating clockwise, and IARs are located exactly N-S, then extensional features near the northeastern and southwestern plate boundaries and contractional features at northwestern and southeastern plate boundaries would be expected (Figs. 3, 4).

The single and double gear models are helpful to understand kinematics of plate rotation, but they do not take into account that a plate is bound in a material. Unlike a free-floating gear, tectonic plates are bound, or at least embayed, by material of some varying viscosity and/or rigidity, causing friction or shear stress that would affect plate rotation. Because of these effects, it is highly unlikely that sweeping extensional and contractional features would be found along entire plate boundaries, as is predicted in the simple gear model (Kattenhorn, *pers.comm)*. Realistically, any contractional or extensional features are expected to be localized. The amount of deformation present on or within a rotating plate is highly dependent on the original shape of the plate before rotation is initiated. If conditions are equal and a similar magnitude of stress is applied, a circular shaped plate would rotate with less effort than a jagged plate. Therefore, more evidence of internal deformation should be present on a plate that was originally more inequant than circular (Lamb 1987).

Internal deformational features including fractures and pseudofaults have been observed on terrestrial microplates (e.g., Easter microplate, Juan Fernandez microplate) between the Nazca and Pacific plates (Fig. 5). IARs on the northern and southern boundaries of the plate are located by tracing the orientation and placement of pseudofaults within the Easter plate's interior and bounding plates. Considering the multiple generations of tectonic structures expressed on the Europan surface, pseudofault identification may be somewhat more challenging than in a terrestrial setting. However, orientation of relatively old ridges in the Europan ridged plains may prove useful in the identification of pseudofaults and IARs.

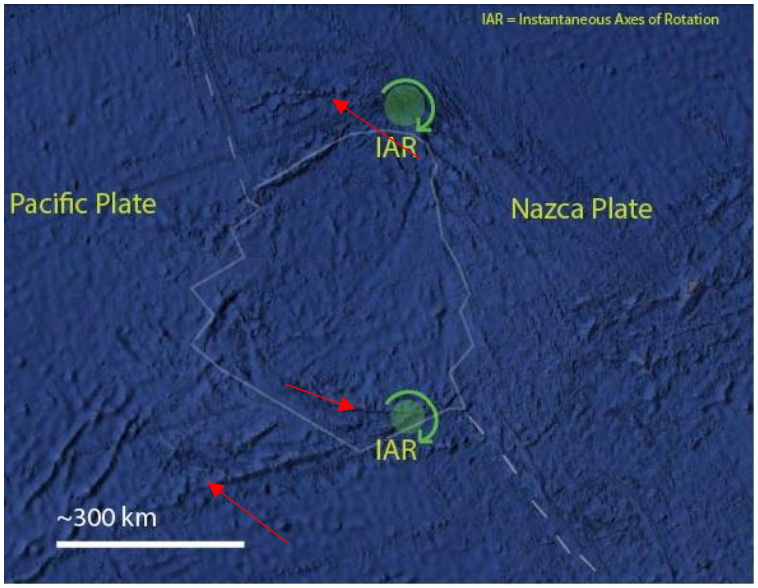

Figure 5*: Oceanic topographical view of the Easter microplate courtesy of Google Earth (-25.280781 S, -113.900194 W). Red arrows illustrate the location of pseudofaults that trace IAR location. Faint white represents approximate plate boundary.*

2.3 Stress Origins

Origins of stress hypothesized to contribute to deformation on Europa's observable surface include: nonsynchronous rotation (NSR), true polar wander (TPW), obliquity, diurnal stress, convection, impacts, and a thickening ice shell (Geisler 1998, Schenk 2002, Bills 2005, Greenberg 2003, Nimmo 2004). These different types of stresses are responsible for forming observable tectonic surface features. For example, orientations of cycloids are strongly correlated with modeled diurnal tidal stress fields with a 1° contribution of NSR (e.g., Kattenhorn and Hurford 2009). Though the stress magnitudes produced from these phenomena are strong enough to influence deformation, it is highly unlikely that dilation/rifting and rotation could be initiated from one source alone. On Earth, for example, Buck (2006) found that magmatic intrusion was needed to accompany rifting and extension of the Afro-Arabian rift system. On Europa, most modeled stress magnitudes do not appear strong enough to rotate large plates (Nimmo and Manga 2009). Therefore, it is highly plausible that a combination of different stress origins may similarly contribute to plate-like movement on Europa's surface.

2.4 Chaos Terrain in Argadnel Regio

A large contributor to Europa's surface deformation is the intrusion of chaos terrains. Chaos terrains comes in a variety of morphologies on Europa. The outward appearance of these terrains may be described as either matrix-like, blocky, or a combination of the two (Collins and Nimmo 2009). Regional chaos terrains can exceed diameters of 1200 km, while lenticulae, pits, and domes can be two orders of magnitude smaller (Collins and Nimmo 2009). Though smaller "chaotic terrain" species are mostly observable at higher latitudes, larger examples and regional chaos terrains tend to dominate equatorial regions (Riley et al., 2000) The physical process of chaos terrain intrusion is not well understood. Several studies have considered mechanisms for chaos intrusion. Earlier models invoked localized warm anomalies in the ice that were amplified by tidal heating, "whole shell" melting, and partial melting of the subsurface (e.g., McKinnon 1999, Collins et al., 2000., Carr et al., 1998). These models were eventually refined and expanded to include diapirism, dike injection, sill injection, brine mobilization, melt through lenses, and impacts (e.g., Collins and Nimmo 2009, Schmidt et al., 2009). Diapirism and associated brine mobilization satisfy most formation criteria, but no one hypothesis can fully explain the ubiquitous presence of chaos terrains (Collins and Nimmo 2009).

More recently, Parro et al (2016) mapped chaos terrain in the "Wedges", an area in eastern Argadnel Regio. Their study found two episodes of chaos terrain intrusion that were separated by the formation of a dark band. Generally, chaos terrain intrusions are among the youngest features on Europa (Kattenhorn and Hurford 2009, Collins and Nimmo 2009).

2.5 Previous Tectonic Reconstructions

Planar tectonic reconstructions have been conducted on several regions of Europa including: Castalia Macula (Rezza et al., 2016), Astypalaea Linea (Perkins et al., 2016), Phaidra Linea (Prockter et al., 2002), Libya Linea (Perkins et al., 2016), and Falga Regio (Collins et al., 2016, Kattenhorn and Prockter 2014). More recently, a planar reconstruction of Falga Regio (55.2 N, 135.35 W) was presented by Kattenhorn & Prockter (2014). Falga Regio was later reconstructed by Collins et al. (2016) using *GPlates*, spherical reconstruction software that employs Euler's fixed-point theorem to achieve better accuracy than planar methods. Euler's theorem states that motion of a rigid body on a sphere can be described in terms of rotation about an axis, projected radially from the center of the sphere (e.g., Euler 1775). The Collins et al. (2016) reconstruction

displayed plates that exhibited clockwise rotations of approximately 45° over a 50-million-year period. Notably, the Collins (2016) reconstruction found a large amount of missing surface area as Kattenhorn and Prockter (2014), though slightly less (Collins, *pers.comm*). Overall, Collins (2016) broke up larger plates defined by Kattenhorn and Prockter (2014) into smaller plate-like fragments. Accuracy of the reconstruction and plate rotations is particularly important in Falga Regio for assessing the first identified occurrence of subsumption bands on Europa and possible plate-like motions in this region (Kattenhorn and Prockter 2014).

2.6 Hypothesis

The apparently large amounts of rotation of plates in the CF area of Argadnel Regio indicate significant tectonic activity. The driving mechanism for that activity, however, is not known. To gain insight into the geologic history in this region, and perhaps the nature of Europan microplate kinematics in general, the work described in this thesis tests the following hypothesis:

Plate rotations in Argadnel Regio are driven by shear flow within the ice shell.

Predictions of this hypothesis are:

- The instantaneous axes of rotation of rotating plates that compose the CF are predicted to be located within surrounding plates or the pull-apart bands that surround the structure.
- Internal deformational features including pseudofaults, tearing, and/or fractures are predicted to be present, and relate to the trajectory of instantaneous axes of rotation.

3. METHODOLOGY AND ANALYSIS

3.1 Data Acquisition

Visible-wavelength images of the surface of Europa were taken by the Galileo Solid State Imaging Camera (SSI) and are available for download on NASA's Planetary Data Systems website (https://pds.nasa.gov/). The images used in this study were taken as part of observation E17ESTREGMAP01 for Argadnel Regio. Resolution of the images is approximately 220 meters/pixel. The E-nth naming convention relates to "E" for Europa and nth for the observation number. This naming convention was used here to circumvent the possibility of changes that can occur in the PDS without notice. Level 0 data were downloaded and processed through the USGS Integrated Software for Imagers and Spectrometers (ISIS3). Images were then calibrated radiometrically and photometrically. These steps ensured lighting was balanced and geometries were appropriate for the required measurements. Imagery data generally were processed to Level 4. These processing steps attached Spacecraft Planet Instrument C-Matrix Events (SPICE) data with pertinent information regarding observations (i.e., solar phase and incidence angles), as well as radiometric calibration. Photometric balancing was applied at this point. Once processing was completed to Level 4, images were projected to a sinusoidal projection. After photometric correction and image projection, cube files were converted to Tagged Image File Format (tiff) files. For accuracy, mosaics were manually adjusted in ArcGIS to correct any misalignment that occurred by employment of the *shift* tool located in the *Georeferencing toolbar*. Measurement of features and distances were executed in GPlates and ISIS3. These mosaics and imaged were used in cross-cutting relationship mapping and geomorphic features characterization (Appendix Fig.A). Level 0 data were used in the characterization of surface features. The Galileo spacecraft contained an algorithm that averages and smooths out pixels that do not contain significant heterogeneity (Prockter, *pers. comm*). This smoothing effect can appear to emulate the appearance of surface flows or cryovolcanic features, potentially leading to incorrect identification of surface features in processed images.

The sinusoidal projected mosaic "Super Mosaic" (SM) (Fig. 2) was used for the tectonic reconstruction and was composed of a combination of images mainly from Europa's trailing hemisphere that range in resolution from approximately 200-400 meters/pixel. Higher resolution images that form this expansive mosaic are from Galileo (SSI) and Voyager images fill in data

gaps. The SM was used for GPlates reconstructions and obtained courtesy of Geoff Collins. Image brightness and contrast were adjusted as needed with Adobe Photoshop for the Argadnel Regio reconstruction to facilitate interpretation of the surface features.

3.2 Tectonic Reconstruction Methods

This study included a reconstruction of the western portion of Argadnel Regio (Fig 2). The first step in the tectonic reconstruction was to map cross-cutting relationships over a larger area (~80,000 km^2) in western Argadnel Regio than the reconstructed area (~30,000 km^2). The larger viewing window enabled a more accurate assessment of the cross-cutting relationships. These cross-cutting relationships provide the basis for interpreting the sequence of plate motions. Although most cross-cutting relationships in the area are clear, a few in the far western portion of the reconstructed area are more difficult to interpret due to chaos terrain disruption, possible cryogenic flows, and possible convergence (Sarid et al., 2002).

The next step of reconstruction was identification and mapping of piercing points and laterally offset features. The identification criteria were that features be laterally offset or displaced, with portions on both sides of the displacement sharing a similar morphology, width, texture, and albedo. This document refers to piercing points, laterally offset, or displaced features as offset markers. Piercing points are generally linear features, such as double ridges, that are truncated by a fault and then displaced. Laterally offset, or displaced features are similar to piercing points, but are related to non-linear structures, such as chaos terrain or the sinuous bands that are observable in the southwestern portion of the study area. These features are especially useful in detecting slip and transtensional motion. I made initial (i.e., t=0) measurements of displacement distance within GPlates, using the Kinematics tool. The kinematics tool recorded changes in displacement over each timestep. Finally, the mean, standard deviation, and standard error were calculated.

Plate boundaries were defined by using cross-cutting relationships and offset markers according to the following five criteria:

1) Plate boundaries were drawn where there was a discontinuity in preexisting features.
2) Boundaries between plates were closely fit, and not allowed to overlap.
3) Plates were configured, so that piercing points and features that shared similar orientation and morphology can be aligned.

4) If multiple cross-cutting relationships were observed, the youngest features were prioritized (Rezza 2016).
5) Bands and Chaos terrain were defined to act as plates in the reconstruction, even though they are not strictly plates. Defining chaos terrain and bands in this manner was useful because the mechanisms of disruption are not fully known, and some contained remnants of degraded surface features that could be traced to adjacent plates. Such degraded features were helpful in the reconstruction process because they could be used as a connector between two terrains/plates (e.g., Fig. 6).

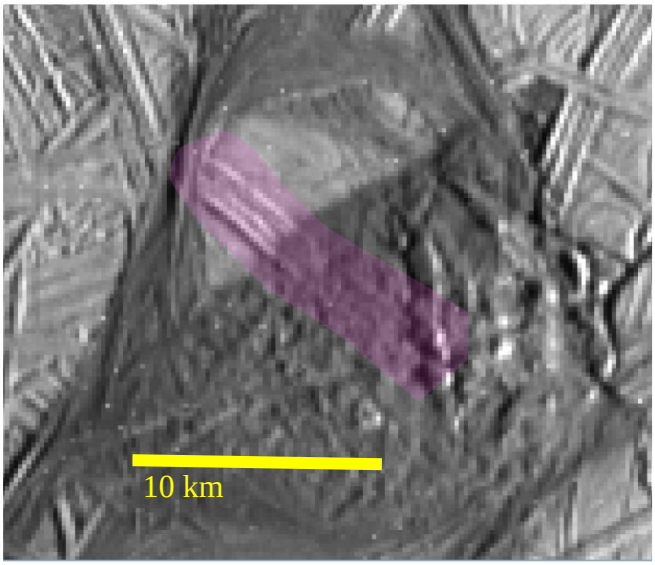

Figure 6: *Remnants of a ridge complex disrupted by chaos terrain southwest of CF in Argadnel Regio (13.65 S, 140.44 W). The faint purple outlines the structure on the plate and the degraded structure in the chaos terrain interior.*

I next developed a planar reconstruction in Photoshop. Once tentative plate boundaries were defined, the image was cut along plate boundaries according to cross-cutting relationships and features that showed the greatest amount of displacement. Features such as double ridges, dilating double ridges, and dilation bands were then sequentially removed so that offset marks could be aligned. Each plate was separated into individual layers to allow freedom for image segments to

be moved laterally or rotated within the Photoshop interface. The planar reconstruction and plate-boundary definition steps were iterated to refine the plate boundaries and to check the identification of piercing points and offset markers. The planar reconstruction provided a basic guide to streamline the more accurate GPlates reconstruction process.

3.3 GPlates

The first step in the GPlates reconstruction was to project a mosaic onto a sphere within GPlates with the "import raster" function. Plate from the planar reconstruction were re-drawn in GPlates, assigned a feature number, and assigned a time period to exist with the "Digitize New Polygon Geometry" tool. Piercing points were marked and attached to their parent plate with the "Digitize New Polyline Geometry" tool. The naming convention of piercing points was based on the identification number and direction towards their corresponding partner. At this point, a rotational file was created where plate number, latitude, longitude, time step, and rotation pole information were stored. Through a Python script, GPlates read through the rotational file to execute plate movement with user-defined timesteps.

To analyze the rotation of the CF, the reconstruction was executed over the five stratigraphically relative timesteps (see section 4.1) with 10 frames per time step. Five timesteps were chosen in order to investigate conditions previous to the rotation of the CF, which was the focus of this study. Timestep t = -50 refers to the oldest sequence and t = 0 refers to the time of Galileo observations. As with the planar reconstruction, the basic procedure was to determine the plate motions that would close the gaps between piercing point and offset markers sequentially for each stratigraphic relative time step. The "Modify Reconstruction Pole" tool was used to adjust plates directly within the GPlates interface. When this tool was used, ROT files were automatically updated. ROT files store information that relates to geographic position, amount of rotation, and duration of time at each position. When groupings of plates were programmed to move collectively, coordinates in the ROT file could be altered directly. Chaos terrain and bands were programmed to appear instantly at the relative time of their formation. The large chaos terrain on the western border of the CF was programmed to exist throughout the duration of the reconstruction because, due its large surface area, its relative stratigraphy could not be established. Once the reconstruction was completed, rotational poles were exported for graphical analysis.

Plates were programed to move directly from one position to another in accordance with a tectonic movement determined from cross-cutting relationships. Another consideration in the reconstruction was to close gaps between plates as much as possible, especially where it was clear that surface area had been augmented during a time step (i.e., band formation). This step is important because missing surface is often expressed as empty space between plates. Finally, reconstructed animations were analyzed to identify and correct any inaccurate events. For example, any overlapping plate movement observed in the animation led to adjustments of the reconstruction as two objects cannot exist in the same space at the same time.

3.4 Geomorphology

The tracking of geomorphic features at five different timesteps was an integral aspect of this study. For each time step, careful attention was given to the search for potential extensional, contractional, and shear deformational features at plate boundaries that should accompany rotation. Contractional and extensional features at plate boundaries are particularly useful in determining whether rotation occurred as a floating block or pinned block (Schouten et al., 1993). Special attention was also given to features such as ridges, older chaos terrains, or cycloids that may become apparent through the reconstruction process at older timesteps. The appearance of such previously unrecognized features at older timesteps was used to corroborate the interpretation of a tectonic reconstruction. Similar attention was given to the identification of deformational features in the interior of rotating plates in the study area. Features such as scarps, faults or pseudofault traces record the evolution of plate rotation and often lead to IARs. This portion of the methodology aided in the identification of IARs and further refined the geometric results of IAR determination. The orientation and geometric changes of structures was recorded and illustrated, especially internal deformation of CF, to document any underlying patterns not readily discernable and was necessary for the identification of rotational deformation features. Visual analysis was bolstered by the measurement of offset markers.

3.5 Instantaneous Axes of Rotation

For the rotation of a rigid body, several methods exist to find the IAR. These methods are derived from the relationship between the velocities of any two points on a rotating solid body:

$$v_b = v_{IC} + \omega \times r_{b/IC}, \qquad \text{(Eq.1)}$$

where v_b is the linear vector velocity of point B in Fig 7, v_{IC} is the velocity of the IAR, ω is angular velocity, and $r_{b/IC}$ is the relative position vector of points B and IC. If v_{IC} is zero at any instance, then Eq.1 simplifies to:

$$v_b = \omega \times r_{b/IC}, \quad \text{(Eq.2)}$$

Because the linear velocity vector is orthogonal to the relative position vector (property of the cross product; Crummett 1994), if a linear velocity direction is known for any two points on a rotating rigid body, orthogonal or normal lines originating from the two vectors will intersect at the IAR. This method was used in the present work based on its kinematic simplicity, the lack of required assumptions, and because the direction of vectors could be determined between timesteps in this work. Other methods have been developed to determine the IAR location. However, those methods require the vector magnitude of offset markers on plate boundaries, which cannot be determined from this data set (Fig.7).

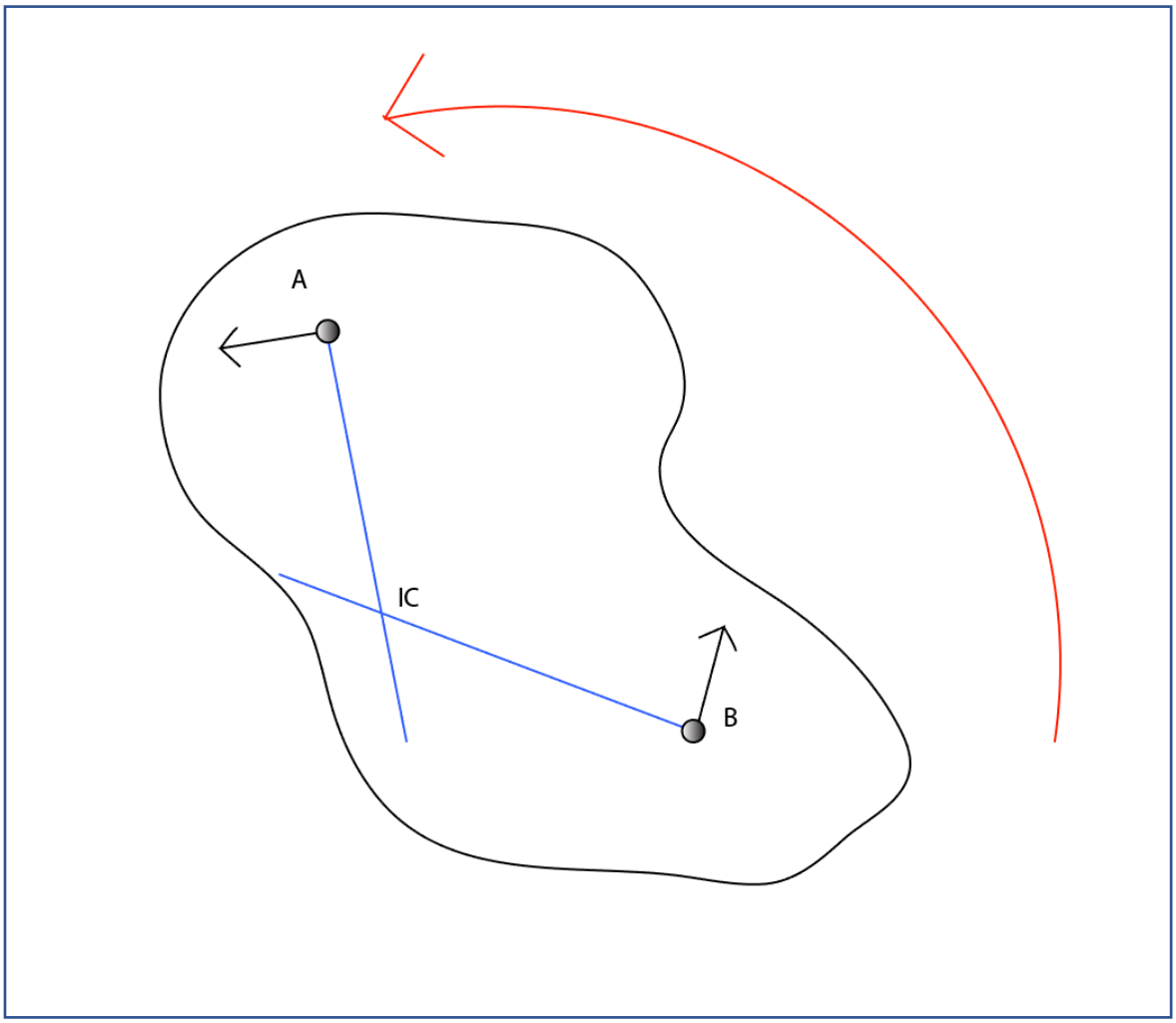

Figure 7: *Example of the rotating rigid body. A and B represent linear vector direction. Blue lines intersect at the instantaneous center of zero velocity or IAR indicated by IC. The red arcuate arrow represents angular velocity and rotational direction.*

Because the rotation of the CF could be perceived as a single rotating system of plates, as well as for individual rotating plates, IAR location was determined for both situations. The only difference in the two methods was the interval of marker placement. Images from t = -50 and t = -40 were captured at the same perspective, imported to Adobe Illustrator, and aligned by the pixel. For the individual plate system, each plate in CF was marked at five separate locations near the outfacing plate boundaries for both timesteps and added into separate layers. For the collective rotating system, markers were made around the outer radius of the CF ~5 km apart in distance. After marking was completed, the images were made transparent, leaving only the corresponding markers from each time step. To obtain the vector direction, vector direction line tips were connected to the center of each spatial marker. Next, squares were created, positioned parallel to the vector direction, and aligned to the vector tail. At this point, normal lines were projected from vector tails. Finally, IARs were marked at intersections of normal lines.

3.6 Workflow

The workflow described in Section 3 is summarized in Fig. 8.

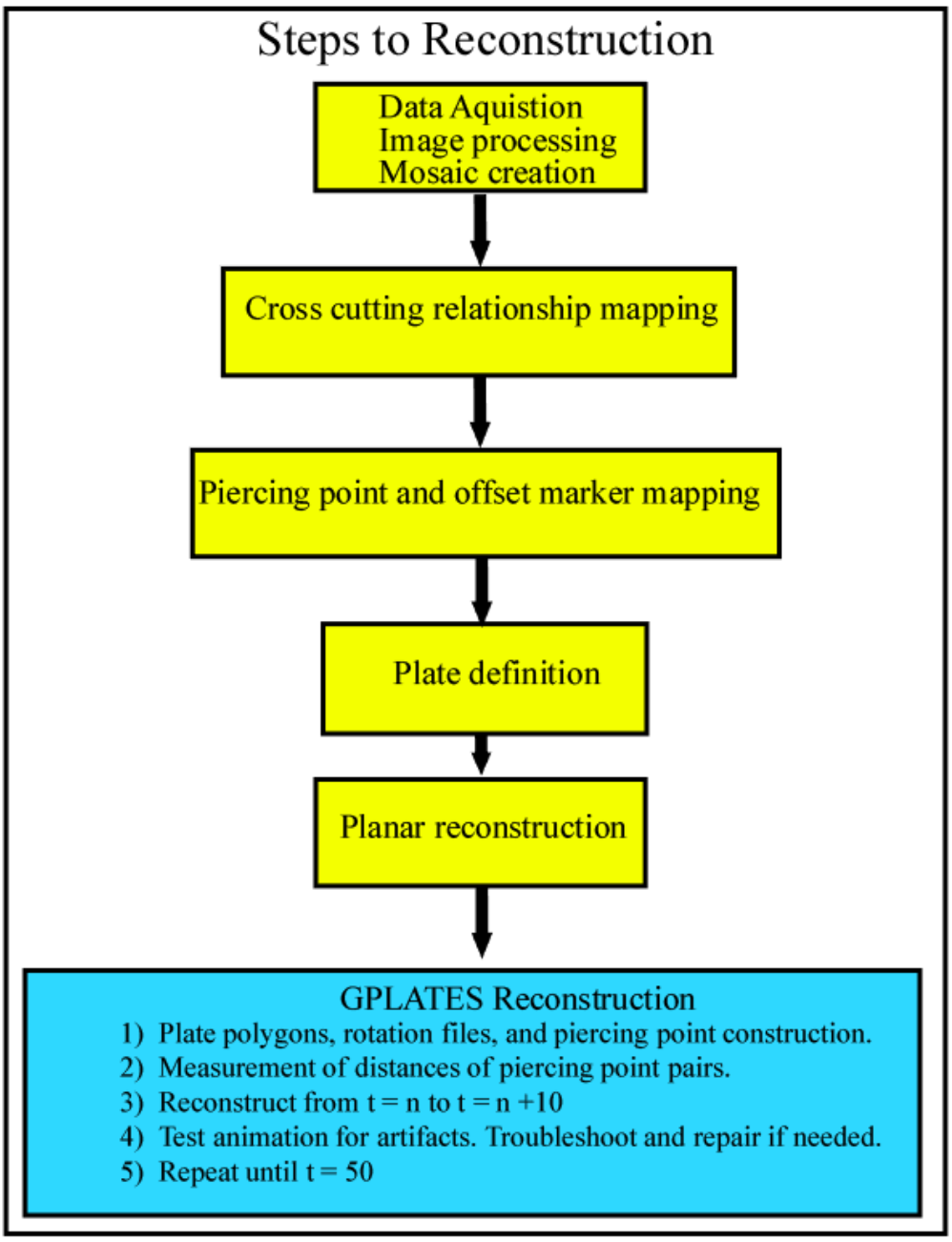

***Figure 8**: Workflow chart for the methods described in this thesis.*

4. RESULTS

4.1 Cross-Cutting Relationships and Brief Description of Episodes

Cross-cutting relationship mapping of the study area in the western portion of Argadnel Regio reveals that the region's tectonics comprise a multi-stage system. At least five generations of tectonic activity were detected: five events that display sub-regional microplate displacements that range from approximately 0.4 to 20.1 km, and two events of chaos intrusion. Current data sets from Voyager and Galileo have only provided a snapshot of surface imagery. Due to limited data from Europa, absolute timing and duration of each generation of activity is not decipherable from the geology.

I visually determined cross-cutting relationships by mapping features that cross-cut or overlap older features. Some features crossed each other outside of the study area, rather than within, so searching for correlation involved tracing features out of the extent of the reconstructed scene to search for a correlation (Appendix Fig.B). For example, not all chaos terrain cross-cuts every other feature in the scene. However, individual examples of chaotic terrain disrupt every episode described below but the western portion of Episode 2. Two NE-trending double ridges at the northern and southern section of the study area were not described as an episode but were used to determine the relative cross-cutting relationships between Episode 1 and Episode 2, as well as Episode 2 and Episode 3 (see orange polyline, Fig.9, and Appendix Fig.B).

Cross-cutting relationships and the resulting stratigraphic episodes are illustrated in Fig. 9 and described here.

- *Episode 1:* Episode 1 displays the youngest features as they are not crossed by any other features. This episode consists of chaos terrains (red areas in Fig 9) and a prominent double ridge (red polyline in Fig 9) that extends N-S through the study area. The ridge and chaos terrains do not cross each other within the scene, but the ridge is cut by other chaos terrains ~200 km south of the scene (20.5 S, 141.52 W). If the chaos terrains in this western portion of Argadnel were all approximately the same age, this cross-cutting relationship outside of the scene would indicate that the chaos terrain in the study area are the younger than the double ridge. The largest two chaos terrains flank a series of plates bounded by arcuate pull-apart bands, which outline the CF circular structure. Three smaller chaotic terrains are found within this structure,

one of which display a small (less than 7 km) conoidal shaped feature that obscures the view of a series of proto-double ridges in the southwest of CF. Observable shadows that are related to this feature suggest that it is relatively topographically higher than the ridged plains, proto-double ridges and pull-apart bands. The second feature in Episode 1 is an approximately 230 km long, N-S oriented, cycloidal double ridge that crosscuts the eastern portion of the CF. The double ridge morphology appears to change as it crosses pull-apart bands north of the CF. The linear feature appears to transition into a band with increasing distance to the north until a data gap border (Appendix Fig.C).

- *Episode 2*: The next youngest episode consists of two linear features, one in the western part of the study area and one in the eastern part (green polylines in Fig. 9). These features do not cross each other in the reconstructed scene, but they appear to have similar relative timing based on cross-cutting relationships to the east (9.46 S, 146.84 W) and to the south (18.89 S, 141.30W). The first of these features is a lineation near the eastern border of CF and is best described as double ridge that transforms to a ridge, with increasing northern distance. The second feature of this pair is a regional scale lineation approximately 160 km in length. The northern half shares a similar appearance to a bright pull-apart band, while the southern half appears more similar to a double ridge. Though challenging to determine with certainty, the transitional point between these two distinct morphologies is near a triple junction with lower albedo, band-like feature (see Appendix Fig.D). The relationship between Episode 1 and Episode 2 was determined with the aid of two double ridges that are cross-cut by Episode 1 yet cross-cut Episode 2.
- *Episode 3*: The next oldest features are two lineations in the western part of the study area (blue polylines in Fig 9). Though they are geographically close to each other, they do not directly overlap, but they are both cross-cut by features in Episode 2 and cross-cut Episode 5. The first is an approximately 135 km long, N-S trending, sinuous, lower albedo double ridge, which is cross-cut by the western lineation of Episode 2 and cross-cuts episodes 4 and 5. The second structure is only 40 km long and is a N-S trending ridge that bisects a bright band which propagates through a relatively small

area (815.7 km^2) of higher albedo ridged plains material. This feature is cross-cut by Episode 2 and cross-cuts Episode 4 and Episode 5.

- *Episode 4*: Episode 4 is composed of an approximately 80 km long, N-S trending lineation and three ridges that line a series of overlapping bands in the NW portion of the study area (yellow polyline and regions in Fig. 9). The lineation is cut by the longer of the two lineations of Episode 3 and directly crosses several features in Episode 5. The lineation is composed of three separate morphologies and cuts through the western third of the CF. The most northern portion of this feature is a double ridge that begins to transition into a possible ridge complex (Appendix Fig.E). The ridge complex transitions into a single ridge that runs south until intersecting with the conoidal feature mentioned in Episode 1. It is possible that the ridge continues far into the south of the study area, but the relationships become increasingly difficult to discern and therefore open to interpretation. The other significant portion of this episode is composed of W-E trending ridges that border a series of overlapping bands that spans the border of Argadnel Regio with Castalia Macula (approximately 800 km). This series of overlapping bands was identified as a convergence zone (Sarid et al., 2002). The ridges of this episode outline the southern portion of these overlapping bands and intersects the large chaos terrain intrusion that borders the west of CF. This feature cross-cuts Episode 5 directly and is cross-cut by Episode 3.
- *Episode 5*: Episode 5 is composed of a maze-like, network of low albedo bands and linear features that range in length, width, and morphology (pink polylines in Fig. 9). These features are cut by features in all other episodes except Episode 6. Despite the vast difference in morphologies, these bands do share a similarly low albedo. The pull-apart bands that border the CF range in shape from sawtooth like to displaying arcuate boundaries. Axial-troughs (Prockter et al., 2002) and escarpments are apparent within most bands around CF. However, the bands display asymmetry with respect to orientation from the axial troughs to the edge of bands. The bands to the southwest display a more anastomosing texture. Some southern bands display axial troughs and bordering escarpments. However, these features are much less apparent than in pull-apart bands near CF. The darker linear features observable in the interior of CF are much smaller in length and width. Though similar albedo is observable between all

features in the unit, the resolution is not adequate to discern if these features are more closely related to bands or scarps.

- Besides the ridged plains, the oldest features observed in the study region was a small area of approximately 923 km^2 with three bright chaos terrains (peach polygon, see Fig.9). that are cross-cut by the arcuate pull-apart bands north of CF. A very small amount of a similar textured material is visible near the southeastern border of the study area but is unfortunately truncated by a data gap. This occurrence is rare in our current dataset of Europa. This feature was not expressed in the GPlates reconstruction.

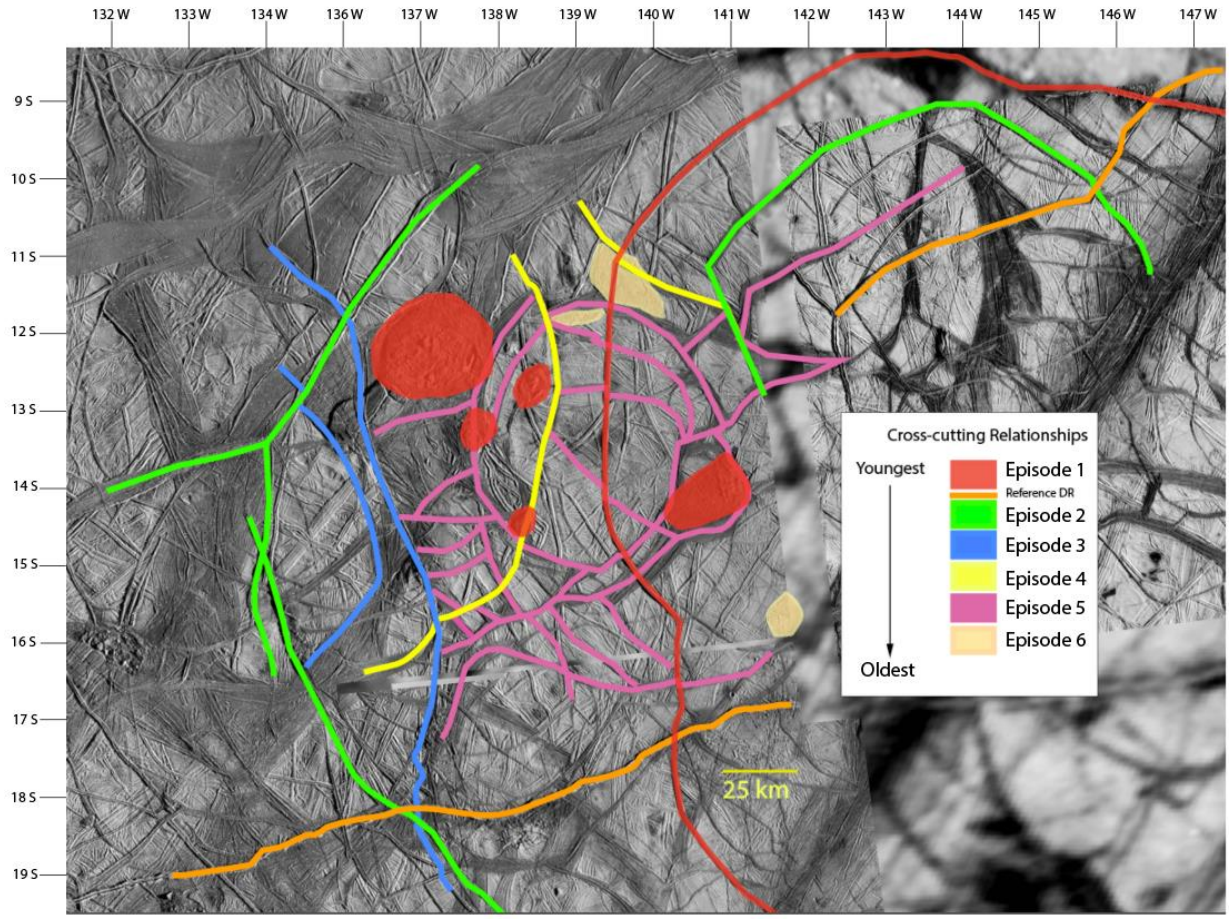

Figure 9: *Map of cross-cutting relationships in western Argadnel Regio. Red polygons symbolize Episode 1. Pea green polyline symbolizes Episode 2. Blue lines represent Episode 3. Yellow lines and polygons symbolize Episode 4. Pink lines represent Episode 5. Episode 6 is represented by peach polygons. The orange line represents two different double ridges which aided in the determination of the cross-cutting relationships between Episode 1 and Episode 2.*

4.2 Planar Reconstruction

At times, the process of reconstructing western Argadnal Regio seemed to be akin to what a paleontologist may experience while trying to reconstruct a fossilized australopithecine or other humanoid skeleton when a specimen is missing many important pieces. Large sections of the study area are highly deformed either from chaos terrain disruption, band formation, strike-slip faulting, convergence, and possible cryovolcanic flows. In some cases, determining a plate boundary with certainty was not possible. Some amount of uncertainty in plate boundaries exist in the plates defined immediately surrounding the large chaos terrain intrusion to the west of CF (green arrow in Fig.10). Most of the uncertainty exists with 10 smaller plates (< ~165 km^2) defined to the immediate southwest of CF, where plates are surrounded by anastomosing band-like features related to Episode 5. In these cases, boundaries were determined based on the presence of subtle albedo changes, apparent texture changes, and the presence of truncated features. However, the boundaries of the majority of plates identified in the study have been defined with confidence by following the aforementioned criteria (section 3.2). I identified 85 separate moving plates for the planar reconstruction, including eight band components and five examples of chaos terrain. The GPlates reconstruction yielded 85 separate defined plates. 13 of the 85 defined plates could possibly be interpreted differently (Fig.10., Appendix Fig.F).

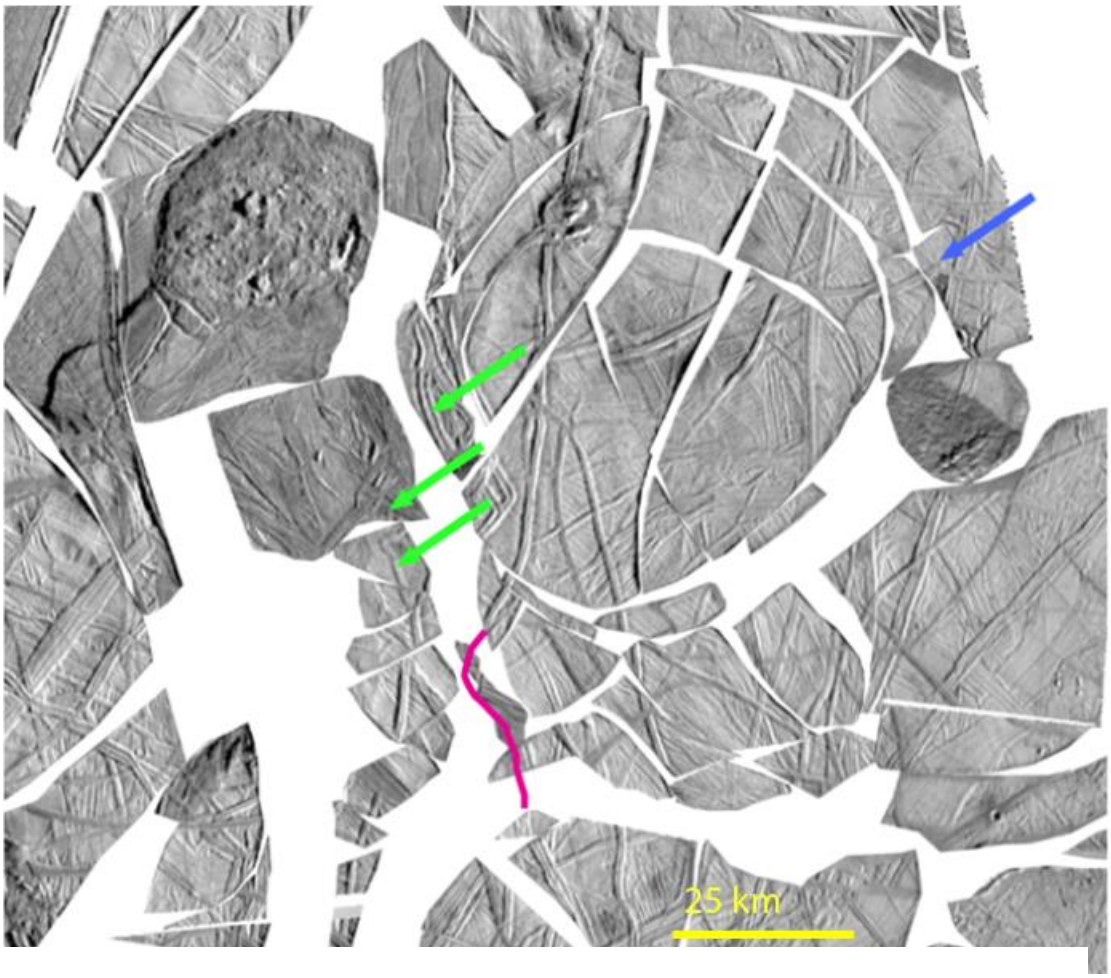

Figure 10: *Planar reconstruction of Argadnel Regio. Green arrows point to examples of plates of uncertainty. The blue arrow points to a reconstructed cycloid. The magenta line indicates a possible deformed double ridge that connects double ridge segments. The blue arrow points to a reconstructed cycloid.*

4.3 GPlates Reconstruction Results

Because of the complexity of tectonically reconstructing a system with a high number of plates, a more detailed illustration of active plates at each timestep is provided in the Appendix of this thesis (Appendix Fig. G.1 -G.5).

Timestep t = 0 to t = -10 is mainly dominated by chaos terrain intrusion. During this timestep, the two large separate units of chaos terrain intrude the area immediately surrounding the CF while three smaller chaos terrain regions disrupt the older surface within the circular structure itself. All but one chaos terrain was programmed to be present before t = 10. The large chaos terrain was included throughout the duration of the reconstruction to avoid a large empty space that could have been misleading in the reconstruction process. Strike-slip movement of less than approximately 2 km for all plates to the east of the N-S trending, cycloidal double ridge (red polygon in Appendix Fig. G-1; see Fig 12-b) also occurs during this timestep.

Timestep t = -10 to t = -20 displays lateral-slip movement on the eastern and western sides of the reconstruction area. To the northwest, plates 1 to 8 move with the opening of a band. These plates exhibit approximately 4.5 km of transtensional movement. To the east of CF, plates 81 and 85 rotate slightly (approximately 3.6 °) and translate northwestwardly approximately 3.5 km (green polygons in Appendix Fig; see Fig.12-c).

At timestep t = -20 to t = -30, most of the plates in the reconstruction remain stationary. However, plates to the southwest of the region (Plate ID #'s 10 – 15) move approximately 6 km to the northwest along a prominent double ridge (blue polygon in Appendix Fig. 11; see Fig.12-d).

Activity increases considerably during t = -30 to t = -40. Approximately 33 plates in the reconstruction to the east of the N-S-trending double ridge (yellow polyline in Fig.12) are laterally displaced up to 8 km. The quantity of displaced plates and the magnitudes of displacements in this timestep represent a significant regional event (yellow polygon in Appendix Fig , see Fig 12-e).

Timestep t = -40 to t = -50 was the most tectonically active periods in the reconstruction. The time period is characterized by a regional band formation event and a large angle of rotation. The reconstruction reveals that the 12 plates composing the CF rotated as a collective unit up to

approximately 40^{o} anticlockwise. The 22 plates to the south appear to be displaced in a southeastwardly fan-like orientation in concert with the rotation of CF. These plates display the greatest displacements in a reconstruction step of up to approximately 30 km. The tectonic activity in this timestep is also responsible for the largest rotation in the reconstruction. One of the relatively smaller plates (Plate 51) exhibits 101.2 ° of clockwise rotation adjacent to the CF during this timestep (Appendix Figs. F and H). Though the driving mechanism would be very different, CF and plate 51 visually appear to rotate analogously to a gear pair with a high gear teeth ratio (greater than 2.5) (pink polygon in Appendix Fig. G.5, and Fig.12-f). The tectonic activity in this timestep is also responsible for the highest amount of rotation in our reconstruction.

The arcuate pull-apart bands immediately surrounding CF are broken into subcomponents: axial troughs with corresponding scarps, and subparallel linear structures (Prockter et al., 2002). Other bands programmed to appear at various times throughout the reconstruction when movement between adjacent plates ceased and space permitted. Past reconstructions generally deleted bands through the duration of the reconstruction. Although deleting the bands closed the space between plates that were once together, bands contain valuable information about relative timing and the propagation of events. Though GPlates does not allow for incremental growth of a feature, the ability to program the feature's appearance to a time step helps the viewer interpret the geologic history of a reconstruction.

Figure 12 is an image series that displays Argadnel Regio at timesteps t = 0 (current), t = -10, t = -20, t = -30, t = -40, and t = -50. The images are displayed from the current timestep (t=0) backwards in time.

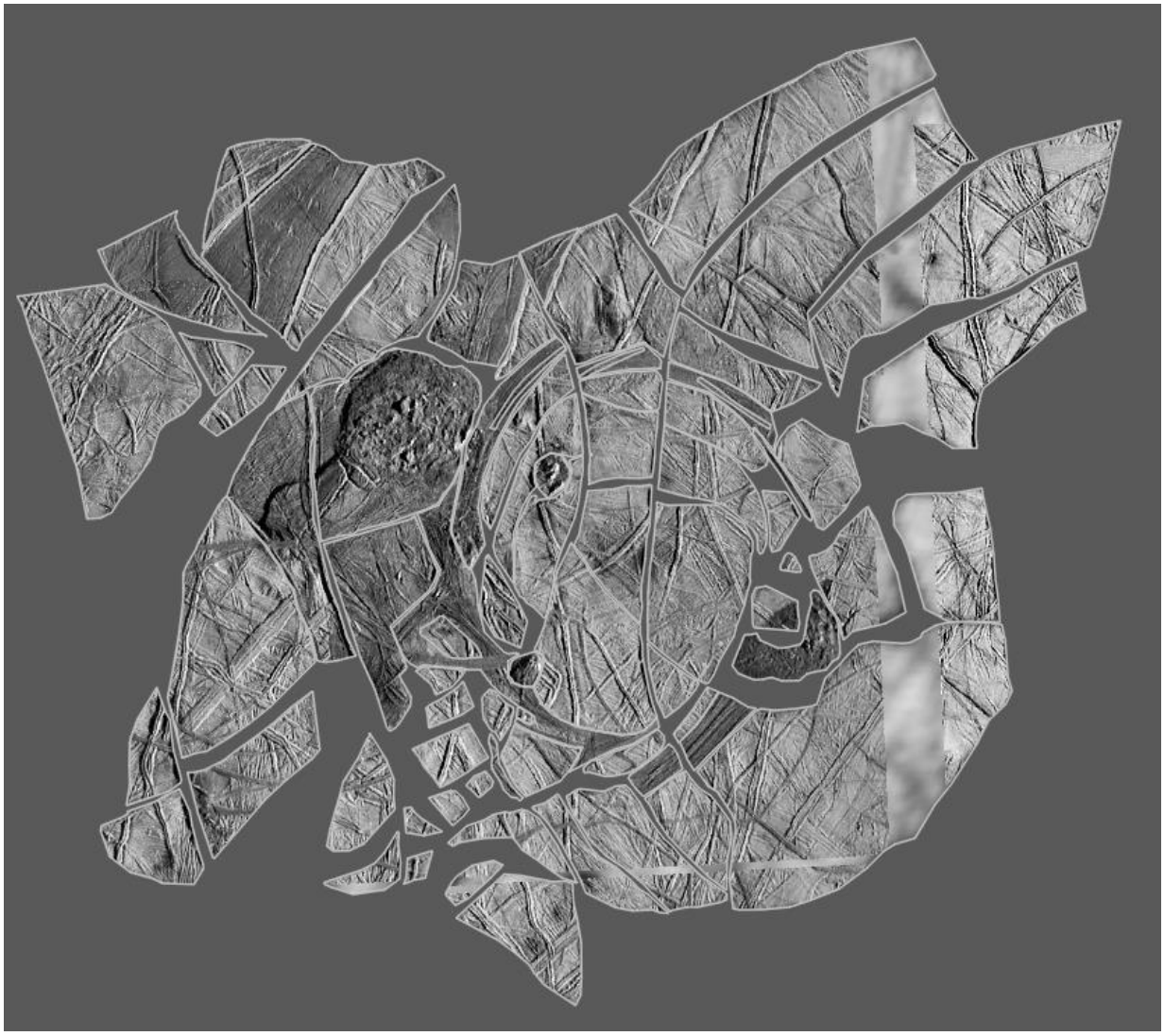

Figure 12-a: *The state of present day (or at least at time of E17 observations). Plates are outlined with silver polygons.*

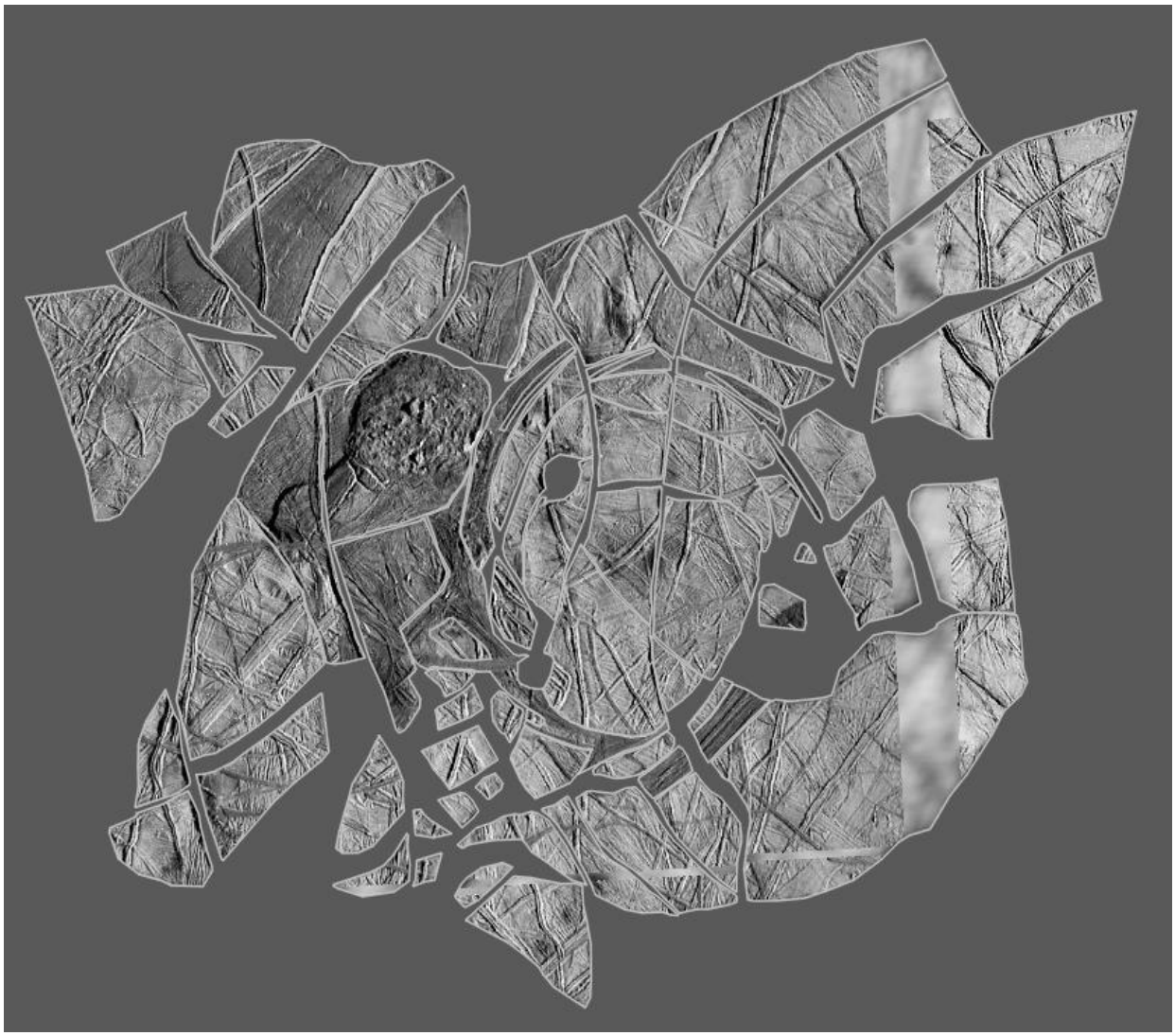

Figure 12-b: *Timestep t = -10.*

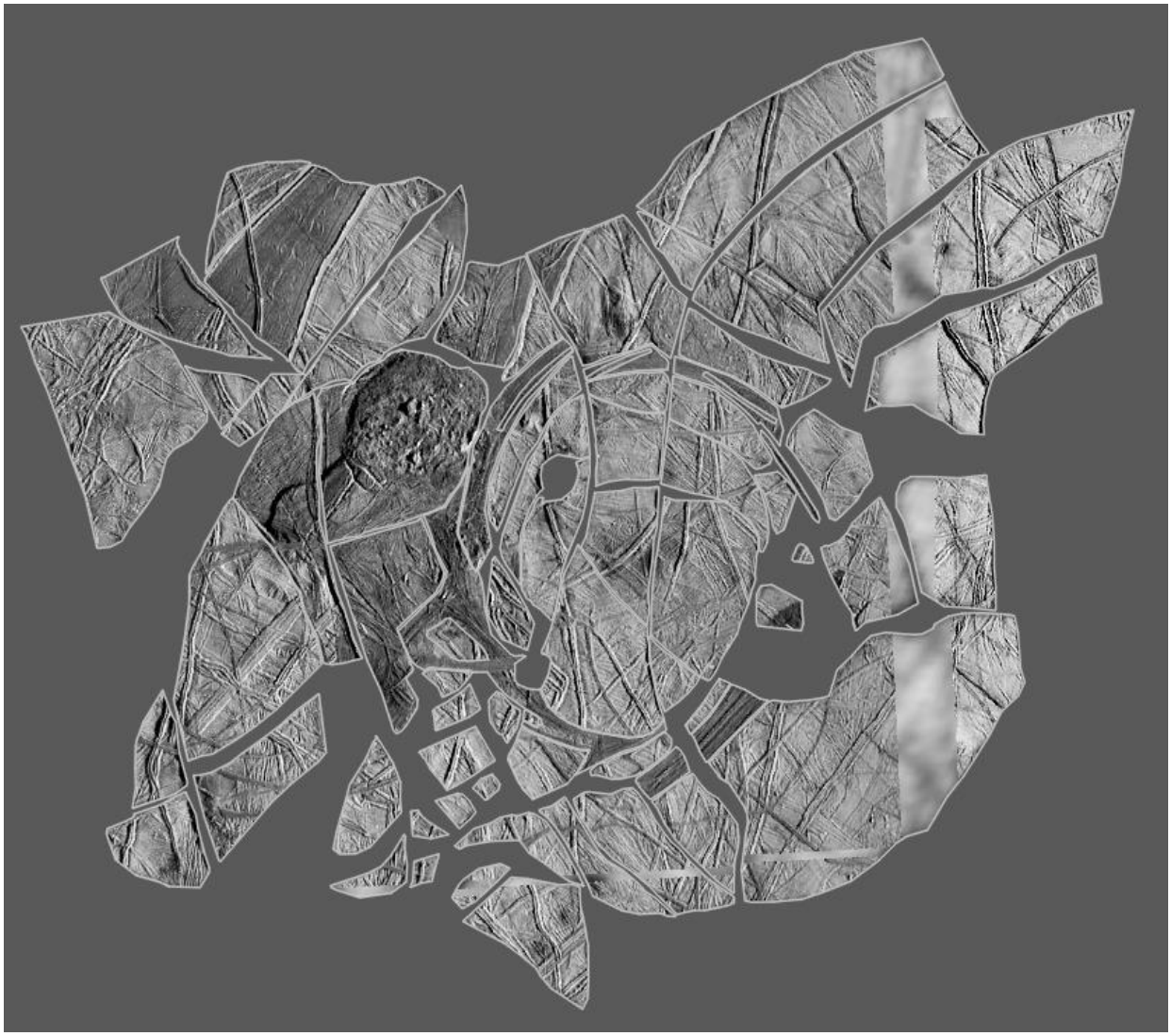

Figure 12-c: *Western Argadnel Regio at t = -20.*

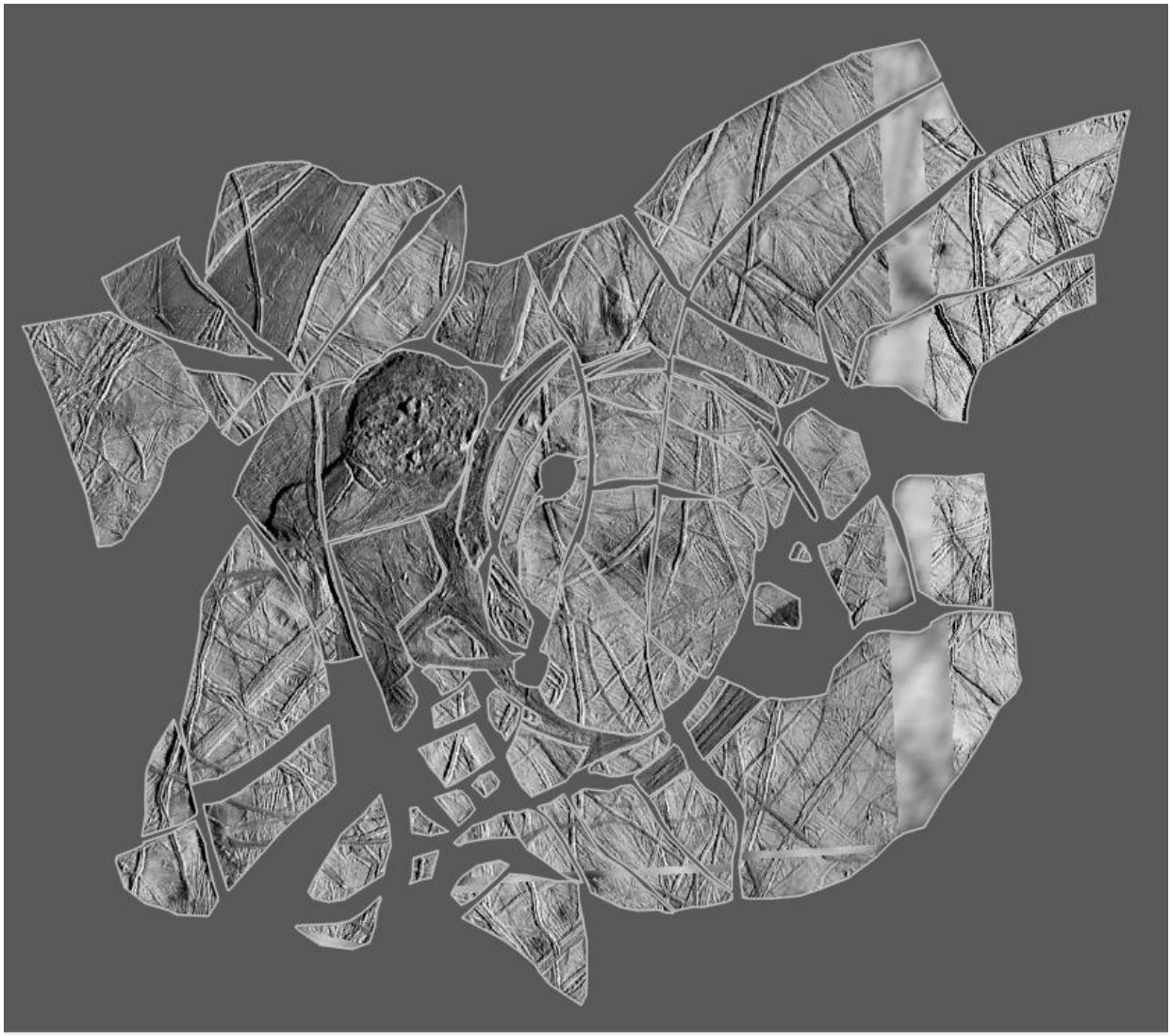

Figure 12-d: *Western Argadnel Regio at t = -30.*

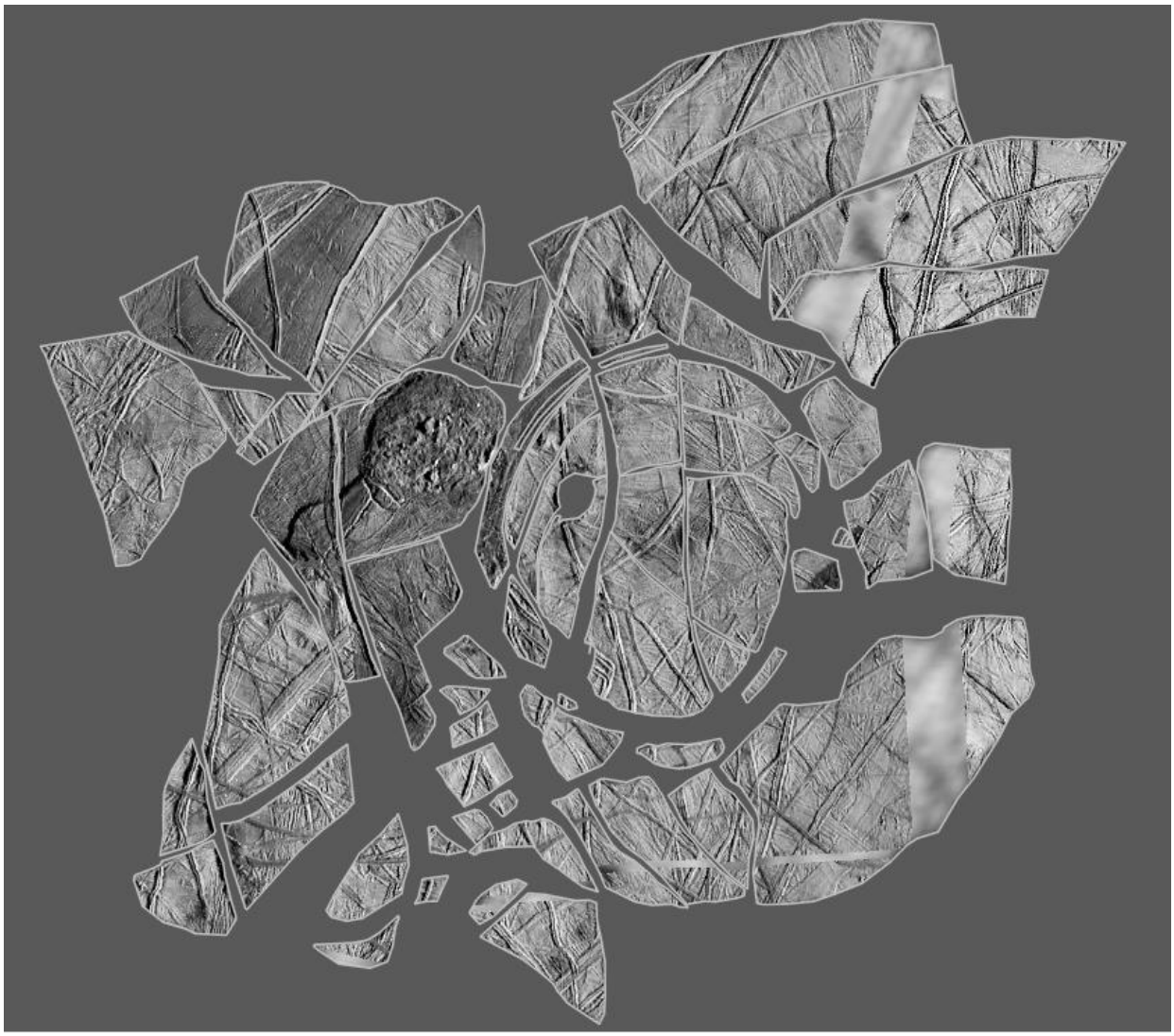

Figure 12-e: *Western Argadnel Regio at t = -40.*

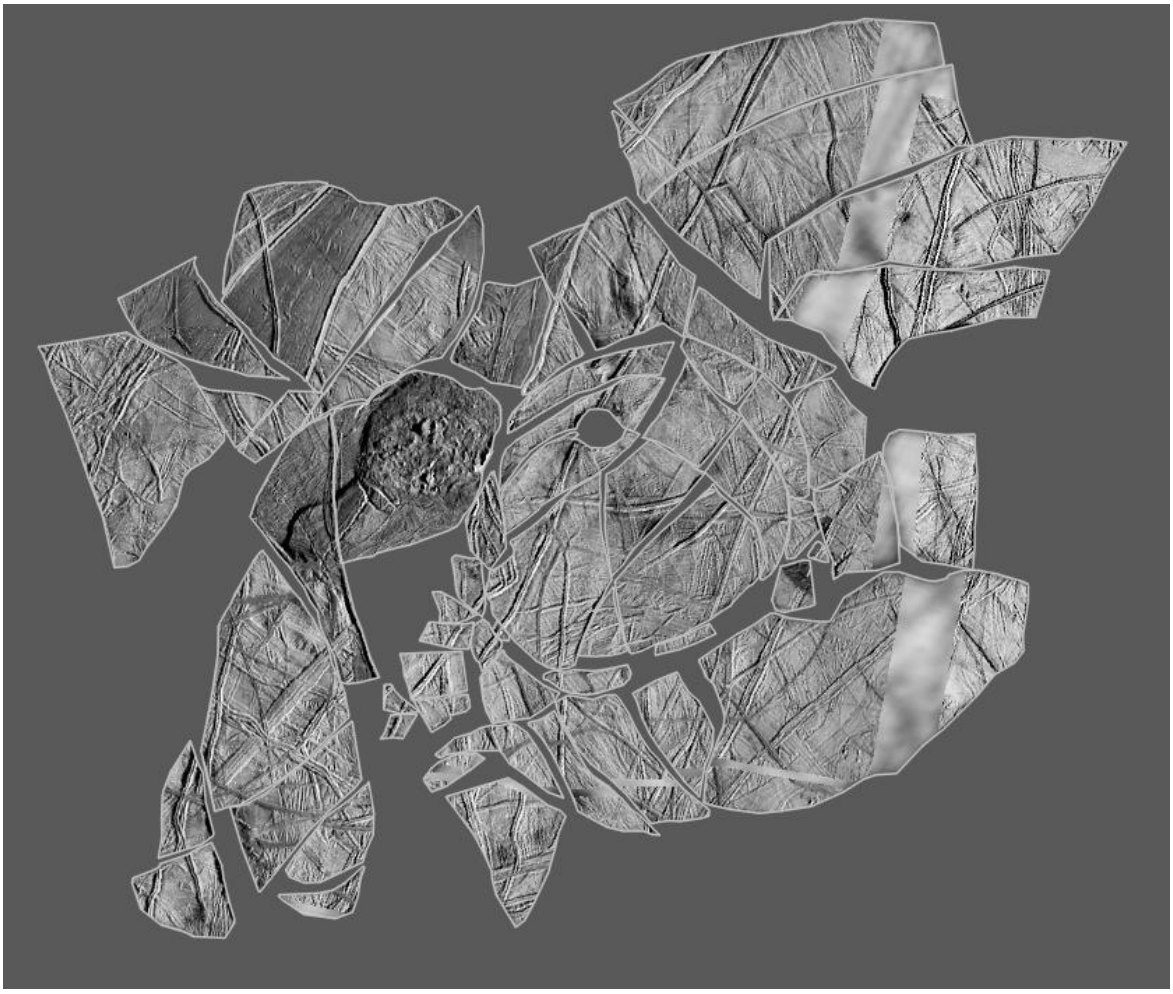

Figure 12-f: *Western Argadnel Regio at t = -50.*

4.4 Rotation and Translation

Most plates in the reconstructed area underwent some amount of rotation. Approximately 70 percent of the plates displayed clockwise rotation (positive values in Table 1) and the remaining 30 percent displayed anticlockwise rotation (negative values in Table 2). The largest amount of clockwise rotation recorded was approximately 85.99^{o} while the minimum was 0.10^{o}. The average amount of clockwise rotation was 20.29^{o} with a standard deviation of 22.61^{o} and standard error of 3.08^{o}. The anticlockwise rotated plates displayed a maximum rotation of 101.18^{o} and a minimum of less than 1°.

Table 1

Rotational Data from t = 0 to t = 50 recorded from GPlates interface. Negative values indicate anticlockwise rotation.

Plate ID	Lat	Lon	Angle of Rotation(^{0})	Plate ID	Lat	Lon	Angle of Rotation (^{0})
1	11.40	-37.49	-1.64	**42**	12.70	-40.23	37.19
2	7.71	-43.08	-1.64	**43**	12.59	-40.24	34.03
3	11.40	-37.49	-1.64	**44**	12.45	-40.12	33.65
4	11.40	-37.49	-1.64	**45**	12.56	-39.91	30.70
5	11.40	-37.49	-1.64	**46**	12.69	-40.01	30.11
6	12.35	-35.35	-1.65	**47**	12.81	-40.14	41.57
7	11.40	-37.49	-1.64	**48**	12.79	-40.13	39.70
10	20.56	-64.78	0.83	**49**	12.51	-39.13	11.06
11	20.56	-64.78	0.83	**50**	13.08	-37.83	9.50
12	20.56	-64.78	0.83	**51**	13.31	-39.45	-101.18
13	10.65	-41.85	-2.15	**52**	13.72	-39.62	85.99
14	14.88	-43.77	22.55	**55**	13.44	-39.09	32.51
15	14.88	-43.32	21.45	**56**	-12.20	146.04	-8.90
16	15.17	-45.03	15.77	**57**	12.87	-38.94	21.02
17	15.33	-45.08	15.77	**58**	-9.20	152.93	-3.89
18	15.72	-44.68	17.94	**59**	-7.99	157.58	-2.67
19	15.49	-45.95	14.10	**60**	-12.82	140.47	-20.39
20	15.72	-45.75	15.77	**61**	13.00	-39.28	16.61
21	70.29	86.42	-0.03	**62**	12.57	-38.74	12.61
22	15.50	-43.81	-1.30	**63**	13.48	-41.61	41.75
23	24.48	-135.32	-1.21	**64**	13.54	-41.01	27.18
25	12.38	-40.55	1.80	**65**	13.69	-41.32	35.38
26	29.22	-137.82	-0.25	**66**	13.45	-40.39	22.18
27	11.97	-45.93	-3.97	**67**	12.71	-37.44	10.84
28	-8.32	142.16	-16.99	**68**	13.75	-40.54	26.60
29	8.09	-37.33	14.50	**69**	10.42	-31.28	6.02
30	8.31	-38.12	17.19	**70**	-13.54	142.23	-15.56
31	8.25	-37.85	15.78	**71**	-0.44	170.84	-1.65
32	8.38	-37.63	16.86	**72**	-13.56	142.68	-5.49
33	9.84	-34.11	3.45	**73**	-14.87	140.24	-25.59
34	8.82	-37.46	19.07	**74**	12.27	-34.49	8.17
35	11.64	-37.98	19.76	**75**	18.61	54.24	0.10
36	12.30	-40.77	38.12	**76**	18.61	54.24	0.10
37	12.38	-40.72	37.51	**77**	18.61	54.24	0.10
38	12.60	-40.86	27.69	**78**	-56.04	20.07	0.38
39	12.45	-40.74	40.15	**79**	-13.77	144.08	-11.58
40	12.21	-39.91	21.46	**80**	-9.56	153.73	-4.32
41	12.65	-40.16	33.80	**81**	-14.50	117.02	1.85
42	12.70	-40.23	37.19	**82**	-13.15	144.71	-12.73
43	12.59	-40.24	34.03	**83**	11.42	-35.19	9.72
44	12.45	-40.12	33.65	**84**	9.50	-37.52	27.78
45	12.56	-39.91	30.70	**91**	9.97	-33.88	8.49

4.5 Piercing Point Distance Results

Piercing point measurement recorded and tracked in GPlates using with the "kinematics tool". A complete listing of measurements are provided in the Appendix in Table A. Average piercing point distance from these measurements across the reconstruction timespan show a general decrease in distance changes between piercing points except for a slight increase at t = -10 (Fig.13, Figs 12-2, and 12-f, Table.2, Appendix Table. A., Appendix Figs I.1 and I2).

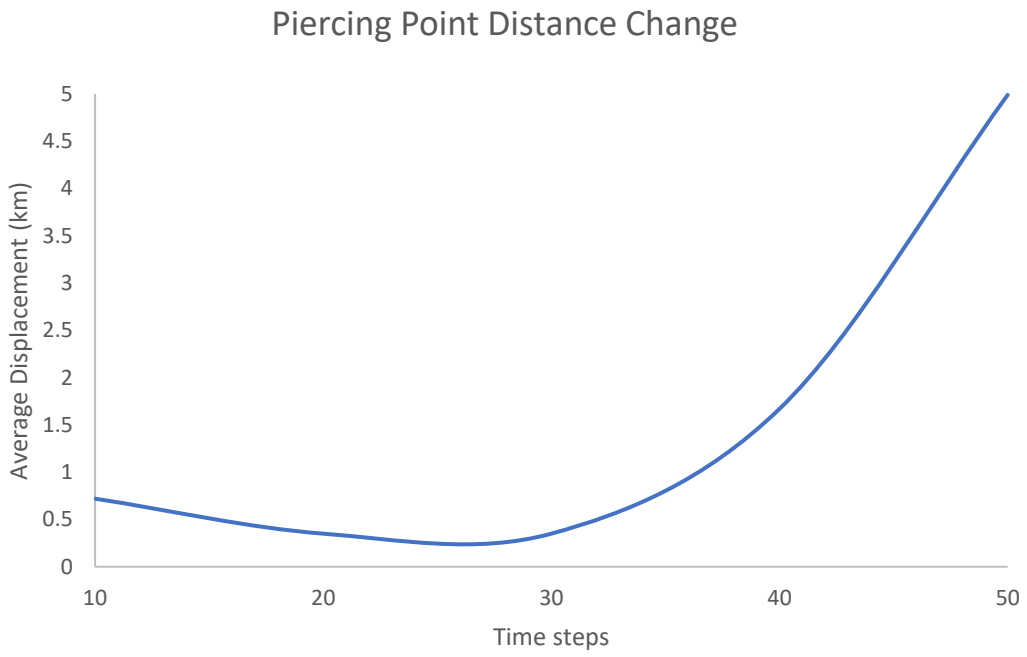

-

Table 2

Average Piercing Point Distance Changes over Timesteps.

Time step	Average (km)	St Dev (km)	Error (km)
t = 50 to t = 40	5.98	6.63	1.06
t = 40 to t = 30	1.67	2.16	0.35
t = 30 to t = 20	0.38	1.12	0.18
t = 20 to t = 10	0.35	1.13	0.18
t = 10 to t = 0	0.72	1.73	0.28

4.6 Surface Area Budget, Bands, and Deformation

Results of the reconstruction clearly revealed both surface area addition and removal within the designated study area (approximately 30,000 km^2). This study estimates that pull-apart bands surrounding the CF created approximately 1200 km^2 of surface area (Knox County has a total surface area of 1361.32 km^2) (Appendix Fig. J, and Table. B).

At t = -50, several gaps between plates remained after connecting piercing points and lateral offsets (Fig.12-f). From a summation of small rectangles within the gaps, the estimated missing surface area is approximately 200 km^2 in the interior of the CF at the earliest stage of reconstruction (blue shade in Fig. 14), and approximately 100 km^2 at t = -40. A removal of surface area was observed between two plates to the southeast of CF (plate ID 82 and 56) at the same timestep. Measurement of corresponding piercing points (piercing point ID 82s, and 56N) display an accommodation of 3.04 km of surface contraction Fig.14, and Appendix Table.C).

Other relatively small spaces between plates exist within the CF, but it is not possible for me to tell in these data if micro-gaps are real or are an artifact of plate shape definition and human error. The reconstruction shows that the interior of CF deformed significantly due to rotation during timesteps t = -50 to t = -40. This deformation can be observed as concentric fracture-like

features that extend from NW and W and intersect near the plate boundary of plates 91 and 51, to the southeast of CF. It is possible that a topographic increase between plate 36 and 37 could be recording contractional deformation. However, distinguishing between shadows and lower albedo material is challenging at this location. No quantitative topographic data were available for this study. A NW– SE trending, low albedo ridge extends from the SE boundary of plate 39 and extends approximately 41 km until termination at the boundary of plate 48 and plate 57 (exterior to CF). This ridge appears to be morphologically unique compared to other ridges and does not correlate to any other ridge segments. Piercing point distance measurements at timestep t = -50 to t = -40 indicate that this ridge has accommodated 0.65 km of lateral displacement (Appendix Table. C) (orange polylines in Fig.14).

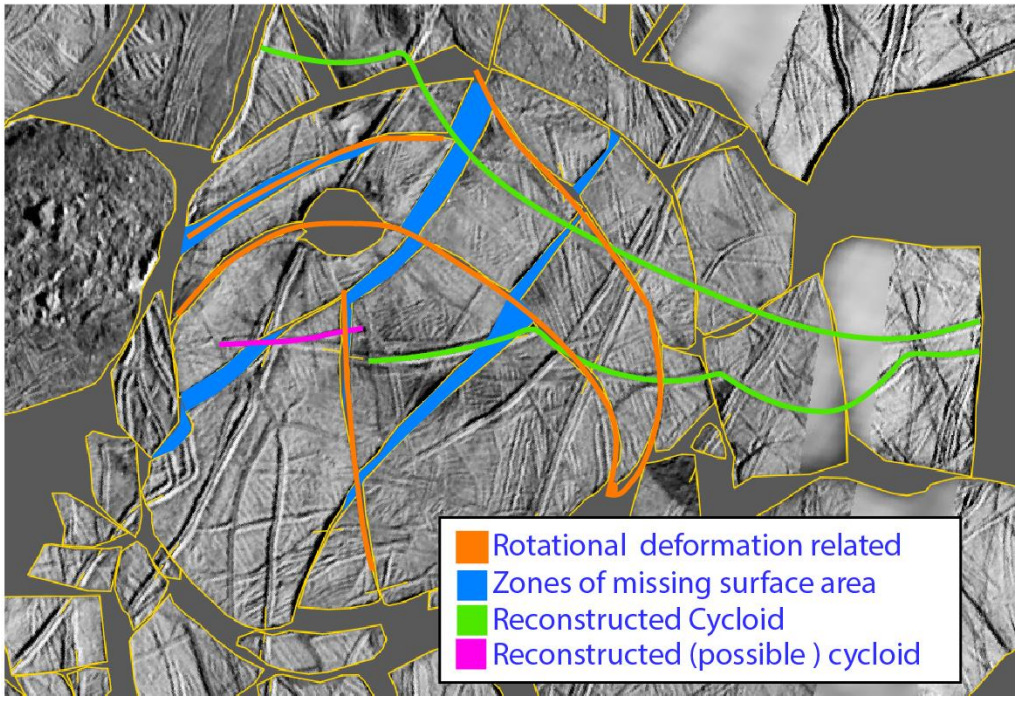

Figure 14: *Map of CF at timestep t = -50 illustrating deformational related features, missing surface area, and reconstructed cycloids.*

4.7 Instantaneous Axes of Rotation from t = -50 to t = -40

As previously described, the location of instantaneous axes of rotation can aid in determining operative mechanisms for rotation. If rotation was driven from lateral forcing at plate boundaries, IARs would be expected on the plate boundaries. If some subsurface flow was responsible for rotation, IARs would be located within bounding plates. Active plates for this timestep (t = -50 to t = -40) are illustrated in the Appendix (Fig. G.5). If we consider IAR location for each individual plate of the CF, the results show that all IARs except for plate 39, and 42 are found outside of their associated plate. For the individual plate system, vector normal lines generally do not intersect at one exact point. The intersections are staggered radially with varying distance for each plate's set of markers (see ellipses, Fig.15). The IAR of plate 42 is located on the junction of plate 42, and 43, 46, and 47. The IAR of plate 39 is located on the junction of plate 39, and 42, and 43. The IAR of plate 37 was located approximately 20 km from its associated plate boundary but on the border of plates 43 and 46. The remaining IARs of (36, 40, 41, 43, 44, 45, 46, 47, and 48) were found to be within other plates of the CF (Fig.15).

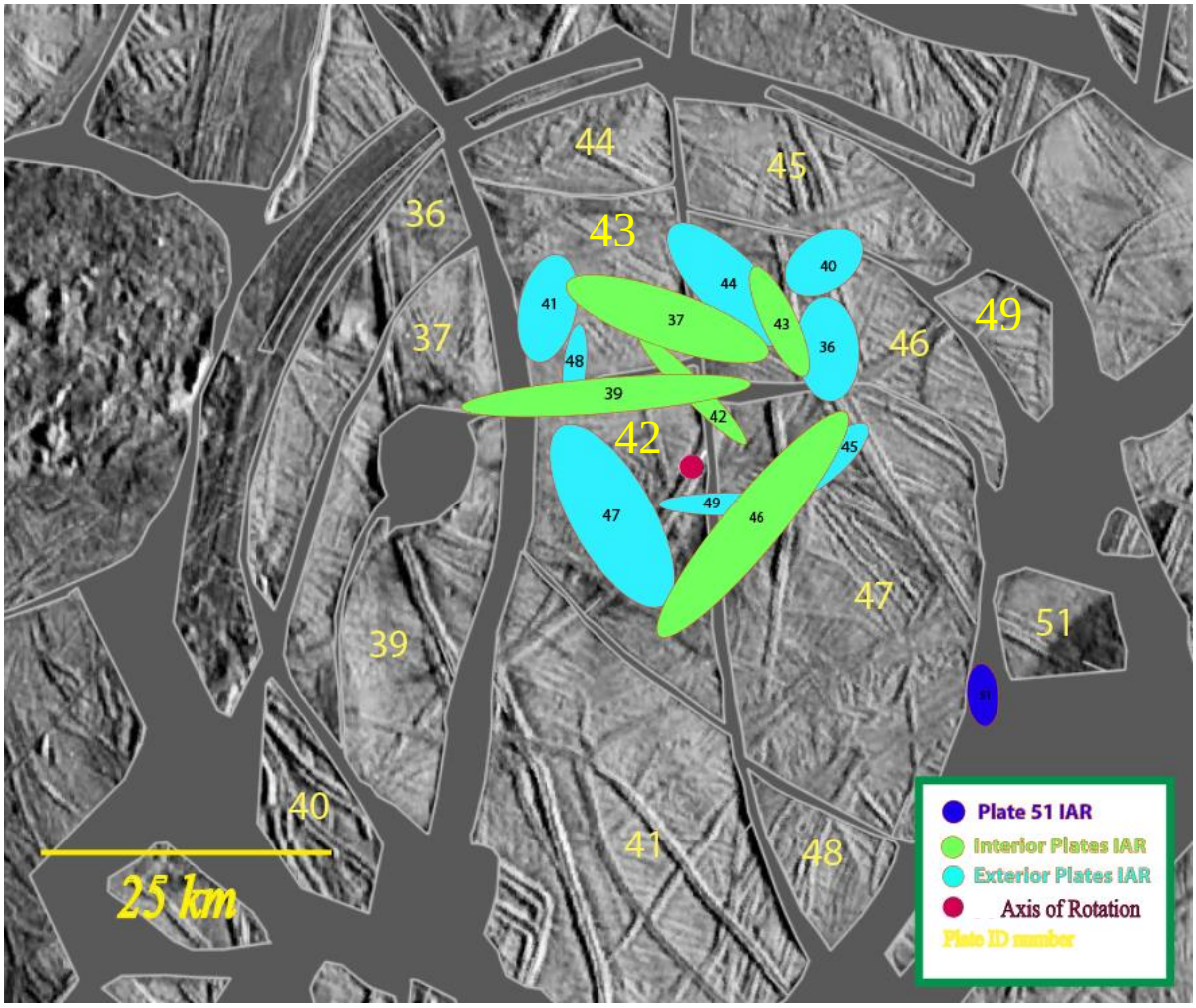

Figure 15: *IAR locations of the CF in western Argadnel Regio for individual plates. Yellow numbers represent the plate number and correspond with numbered IARs. The green ellipses represent IARs that are associated with plates (37, 39, 42, 43, and 46). Plate 51 is represented by the dark blue circle. IAR location and the tectonic reconstruction show that plate 51 rotated clockwise due to CF's anti-clockwise rotation. The axis of rotation was determined by observing that the latitude and longitude of the area marked by the red circle did not change during t = -50 to t =-40.*

The method treating the CF as one collective rotating system found approximately 230 intersections of vector normal lines within the interior of the CF. This method of equal distant marker measurement displayed some single IARs as close as approximately 3 km from the boundary of the CF, but the majority were found in clusters of IARs at varying densities of IARs and distances (~7 km – 50 km from the axis of rotation) within the CF (Fig.16). The results of the collective rotation system and individual plate rotating system appear to be similar in that the majority of IARs are approximately concentrated in the same geographic locations throughout the interior of the CF. Though visually complex, this method captures nuances of all combinations of interacting plates that compose the CF (Fig.16).

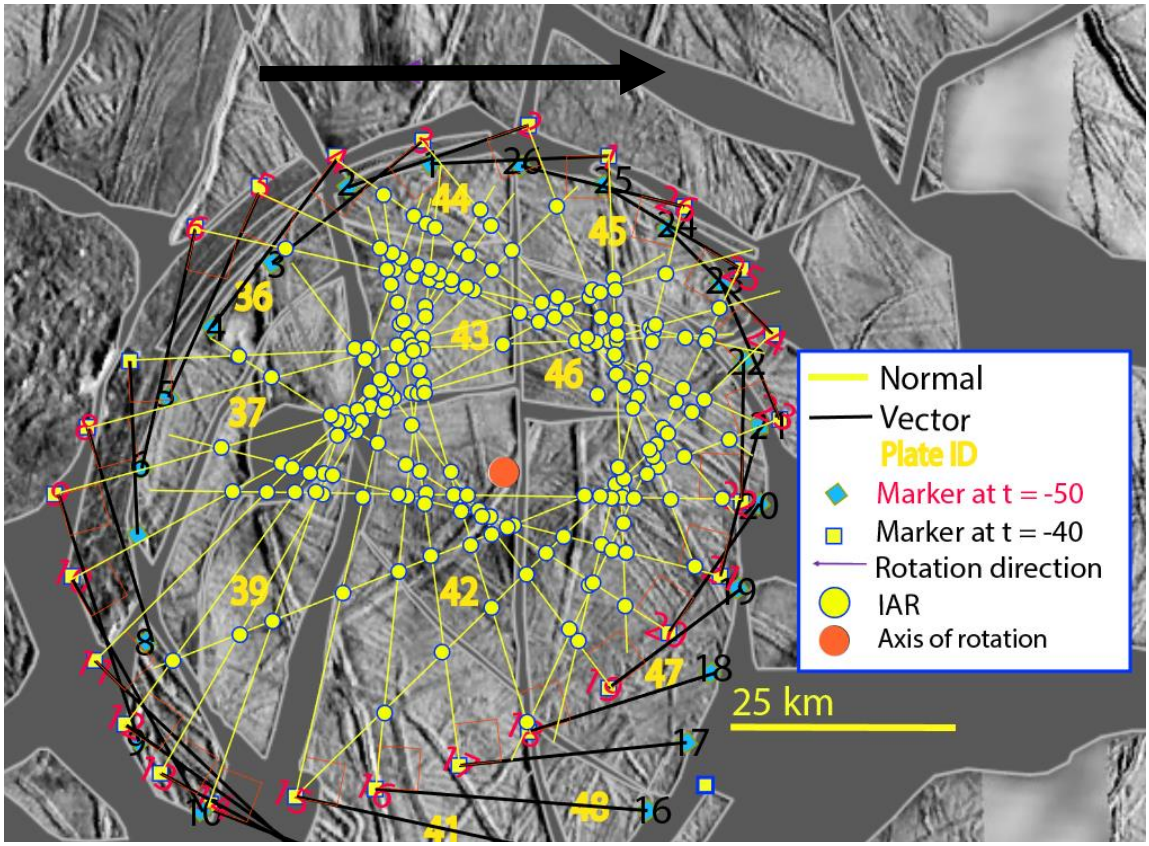

Figure 16: *IARs in the CF of Western Argadnel for a collective rotating system of plates. IARs are at intersection of normal lines from vector tails and noted by yellow circles with blue rims. Due to IAR clustering, the blue rims were used to help distinguish IARs. Markers were set at on the boundary of the CF at distances approximately 5 km apart. Small squares were used to assure proper alignment. The axis of rotation was determined by observing that the latitude and longitude of the area marked by the red circle did not change during t = -50 to t =-40.*

5. DISCUSSION AND IMPLICATIONS

5.1 Interpretation of Results

The location of the IARs identified in this work indicate that the axis of rotation of CF has undergone little to no translation during timestep t = -50 to t = 40; the overall motion of CF appears to be nearly purely rotational. To put it simply, the rotation of CF is analogous to a tire that is stuck in the mud. During remaining timesteps, plates that compose the CF display only lateral movement along double ridges from t = -40 to t = -30, and t = -10 to t = 0.

The observed distribution of IARs determined does not match either endmember that was introduced in the hypothesis of this thesis. Explanation for this occurrence may be related to overarching assumptions included in simplified models, such as spinning or slipping tires, and pinned block rotations or floating block rotation. First, these models assume that the behavior of the rotating bodies is rigid. In non-rigid body deformation, rotating blocks can be deformed either by dilation (change in volume) or distortion (change in original shape) (Hatcher 1995). Unfortunately, the Galileo SSI did not provide adequate resolution to see evidence of a change in volume near plate boundaries, though deformation related to volume change is common in terrestrial fault and shear zones. However, the missing surface area detected at t = -50 suggests that volume change did occur within plates that compose the CF (Fig.14).

The results of the tectonic reconstruction suggest that the overall system of CF in western Argadnel Regio deformed due to rotation. This interpretation of deformation as a result of rotation is based on several lines of evidence. First, the inner area of CF displays approximately 200 km^2 of missing surface area at t = -50 and decreases to approximately 100 km^2 by t = - 40. Second, the measurements of several piercing point pairs exhibit the accommodation of 0.38 km to 3.3 km right-lateral strike slip movement. Right-lateral displacements can be observed in places between all 11 plates that make up the CF. Third, two E-W trending concentric fractures and one NW – SE trending ridge exist in the internal structure of the CF and do not reconstruct to any exterior features at any point during the reconstruction.

5.2 Edge-Driven vs Shear Flow Within the Ice Shell

The reconstruction and measured locations of the IARs indicate that rotation of the CF as a collective group was not edge-driven during t = -50 to t = -40, but the rotations of some of the

plates at the center/interior of CF do appear to have been edge-driven. Analysis of the tectonic reconstruction tells us a multi-plate system rotated approximately 40° about a vertical axis (plate 42) with no measurable translation of the axis of rotation. IAR locations associated with plates along the outer radius of CF do not exhibit kinematic behavior of a system that is classically defined or characteristic of "edge-driven" tectonics. If the rotation of CF was driven by lateral forces from bounding plates, IARs would be located on the boundaries of plate margins rather an average of approximately 20 kilometers within the rotating plates as measured. However, "edge-driven" behavior was exhibited with plates 39, and 42. These plates are located in the interior the CF and are surrounded by outer plates of the CF. The IAR placement suggests that these two plates were in fact driven by lateral forces from bounding plates. Plate 51 appears to be completely "edge-driven" by the rotation of CF. This rotational behavior is analogous to a set of different sized, rotating simple gears.

5.3 Piercing Point Distance Analysis

The piercing point displacement distance change with respect to timesteps analysis could suggest that tectonic activity seems to generally decrease in tectonic movement with time, until the last timestep where there is a slight increase. As previously mentioned, absolute time on Europa is currently unknown and anyone of the five timesteps realistically could be augmented or diminished, greatly skewing the plot (Fig. 13). The nature and timing of chaos terrain emplacement is also unknown at this time. Therefore, these results do not imply a disagreement on the consensus that tectonic activity has changed overtime on Europa, changing from conditions for applicable for plate-like motion to chaos terrain emplacement. However, the occurrence of older examples of bright chaos terrain should be the focus of future studies. When considering relative timing of these modeled events, it could be possible to constrain time to some extent from band opening velocity models or material brightening (Prockter et al., 2002, Prockter et al., 2017). Many of the bands that are observable throughout Argadnel Regio display a relatively lower albedo than the plates that they embay as well as the albedo of many other regions on Europa. On Europa, it is thought that material brightens with age. This means that material that displays a low albedo is younger than material that displays a high albedo. The occurrence of dark albedo throughout Argadnel Regio (especially western Argadnel Regio) suggests that the entirety of the events modeled in this thesis could have taken place more recently in Europa's history.

5.4 The Evolution of Argadnel Regio

What drove rotation of the CF in western Argadnel? IAR locations suggest that overall rotation of the CF did not occur due to lateral forcing at plate boundaries from bounding plates. Could convective forces produce lateral flow vigorous enough initiate rotation? Previous investigations suggest that thermal convective forces produce a very small amount of stress (< 100 kPa) (Nimmo and Manga 2009, McKinnon 1999). However, other studies show convection due to compositional heterogeneity could produce up to 1 MPa of stress (Pappalardo and Barr 2004, Han and Showman 2005). Though this amount of stress is relatively small, the right combination of physical parameters such as grain size, and viscosity could conceivably initiate rotation (Schulson, 1987). Convection does therefore appear to be a possible source that is consistent with the rotations observed in this study, but it is not possible to conclusively determine the source. If convection is the driving force, then it could be expected that material from within the ice shell could be close to the surface in Argadnel Regio. Considering the ice shell is most likely greater than 10 km thick, it is unlikely that an unmanned submersible vehicle could penetrate this distance to sample the ocean directly. Therefore, Argadnel Regio could be a potential landing site for a future mission that aims to detect signs of life.

The presence of asymmetric pull-apart bands that surround the CF suggest another possible mechanism that drove rotation. Results of Stempel et al (2005), and Nimmo (2004) suggest that stress associated with band opening could be substantial (0.3 – 2 MPa). Band opening would especially hold if combined with other ongoing stresses. In fact, some models predict that band formation is directly related to nonsynchronous rotation (Stempel et al 2005). Diurnal stress magnitudes should be factored in with other stresses modeled due to Europa's 3.5-day orbital cycle. It is conceivable that a combination of stresses could initiate rotation, especially if preexisting fractures exist.

Regionally, the greater area of Argadnel Regio displays other features somewhat similar to the area that was reconstructed for this thesis and could suggest possible rotation of plates at a regional scale. Arcuate bands are observable throughout the region as well as several other circular structures vaguely similar to the CF. A series of four N-S trending saw-tooth shaped pull-apart bands are observable directly east of the CF. The geometry of these bands suggests these features could have formed by a combination of transtensional and anticlockwise rotational

movement, similar to the CF. It is conceivable that similar further analysis of eastern Argadnel Regio would yield similar results as this study. Unfortunately, the current data set is not suitable to make out surface features in any significant detail.

It has been suggested that the deformation in Argadnel Regio could be related to regional right – lateral strike slip motion and that the current state of Argadnel Regio is a result as a type of "meta-cataclasis" (Kattenhorn, *pers.comm*). On Earth, cataclasis can be observed in fault zones as material gets broken down into smaller components (i.e., comminution). If correct, this idea would involve regional deformation occurring as a result of Argadnel existing within a shear zone. As the larger plate began to fracture due to movement, heat flow would exploit zones of weakness yielding band formation and rotation of deformed material. In this model, band rotation could conceivably be accompanied by uplift due to thermal buoyancy (Schubert et al 2001). If no thermally buoyant force or other force existed at the time of rotation, then IARs would be expected to be on plate boundaries. This assumes that band formation is analogous to terrestrial mid-ocean ridge formation and forces can be produced laterally at a plate boundary. In all likelihood, a combination of both forces is conceivable.

Based on previous work by Prockter et al (2002) and Stempel et al (2005), this study assumes that Europan band formation is analogous to terrestrial mid-oceanic ridges and that slower spreading rates apply. Therefore, assuming spreading rates between (0.2 - 3.5 cm per year) and the average bandwidth (4.71 km) near the CF, the rotation of the CF could have taken place over a period of $1.3 \times 10^5 – 2.3 \times 10^6$ years.

5.5 Far Reaching Implications

The results of the reconstruction, and cross-cutting relationship mapping have several far-reaching implications. Overall, these results corroborate with the idea that Europa has undergone a transition in resurfacing style from a more tectonically active system to a more chaos-driven system (Prockter et al 2002). However, older bright chaos terrain mapped in my study area as well as in the "Wedges" in eastern Argadnel Regio. Parro et al (2016) suggest that regional conditions within the ice or below the ice shell have been favorable to chaos terrain intrusion at least twice in Argadnel Regio. The possible cyclical occurrence of chaos terrain intrusion does not necessarily reflect the characteristics of the entire ice shell on a global scale. In fact, the amalgam of results from this study and recent tectonic reconstructions suggest that plate-like

motions on Europa vary from regionally and appear to be episodic (Collins et al., 2018). With the current studies, it is interesting that in Argadnel Regio old chaos terrain is immediately followed by band formation. Is it possible that chaos intrusion and band spreading are related? If so, old chaos terrain could be the first gasp of heat from a single or multiple ascending thermal plume originating from within the ice shell or from the silicate surface.

Results of this research show that double ridges have many functions on Europa. Firstly, the results of the reconstruction corroborate the idea suggested that surface area contraction can be accommodated in smaller, discrete locations such as double ridges (Patterson et al., 2002, Culha et al., 2014). This occurrence does not solve the Europan surface area budget disparity at the same magnitude of subsumption bands. Nonetheless, combing the double ridge contraction with regional folding across the Europan surface (Prockter and Pappalardo 2000) could make a small contribution. Secondly, the transition of double ridges to bands, and double ridges to ridge complexes in our study area confirm that bands can possibly exploit preexisting weakness in double ridges during tectonic movement of plates (Prockter et al., 2002). This occurrence can be observed in Episode 1 in the double ridge that transitions to a "fast spreading" pull-apart band, and in Episode 5 in a double ridge that transitions to a small, low albedo ridge complex

The results of this study could be tested by future studies. Future studies will conceivably investigate the presence of chaos intrusions, old and young, when better data are available. Instruments such as the Radar for Europa Assessment and Sounding: Ocean to Near-surface (REASON) planned to be aboard NASA's Europa Clipper could detect the characteristics of chaos terrain intrusion, internal ice shell structure, and interface with chaos terrain and surrounding ice ("country ice"). REASON also could possibly detect subsurface structure that may accompany solid-state convection or the effects of plume emplacement. The Shallow Radar Sounder aboard the Mars Reconnaissance Orbiter has similar specifications to REASON and has been successful at identifying dome-like structures in the Martian south polar cap. Hopefully, data REASON will enable Europan scientist to provide answers to many of our questions to which currently remain elusive. It would also be useful to investigate the composition of Argadnel Regio, as composition would help put better constraints on the stratigraphy. Finally, it would be beneficial for future studies to tectonically reconstruct more regions of Europa with GPlates, especially eastern Argadnel Regio, and perform a similar kinematic analysis and compare results.

The same type of analysis could be completed polygonal ice blocks that were embayed and rotated during the event that created Conomara Chaos, Europa, investigated by Spaun et al., (1998). The kinematic analytical methodology outlined in this document could also be used on past tectonic reconstructions where significant rotation has been detected. Though terrestrial microplate rotation models (e.g., McKenzie and Jackson 1983, Lamb 1988, Schouten et al., 1993) have done well in describing a one microplate terrestrial system, future work with terrestrial methods may need to be more finely tuned to a complex system of multiple rotating plates that exist in western Argadnel Regio and potentially the greater Argadnel Regio area. This idea is clearly based on the fact that a significant portion of the presented results were not considered in the design of this hypothesis.

6. CONCLUSIONS

The objective of this research was to investigate the mechanisms behind microplate rotation in western Argadnel Regio. I have presented a tectonic reconstruction was presented within the study area that was used as the subject of kinematic analysis. The kinematic analysis determined that Argadnel Regio underwent significant episodes of tectonic plate movement and rotation of up to approximately 40 ° in an anticlockwise orientation. Lateral offset and piercing point analysis displayed a general waning of tectonic activity that transitioned to a more chaotic system. The IAR location results suggest that microplate rotation in the study area was driven by a combination of shear flow within the ice shell for the collective unit referred to as the CF in this document and edge-driven processes within the structure. This work offers an evolutionary model of western Argadnel Regio. Moving forward, plate tectonics, especially regarding microplate rotation, do not as yet have a unified mechanism that can describe the evolution of the Europan surface. Finally, a combination of stresses are interpreted to be responsible from CF's rotation during t = -50 to t = -40. Similar to previous studies of Europa, this work has likely posed more questions than answers. Missions such as the Europa Clipper, and an eventual lander will hopefully provide opportunities to collect more data that will help us answer Europa's mysteries. This study scratches the surface of one small portion.

REFERENCES

Balachandar, S. and Yuen, D.A., (1994). Three-dimensional fully spectral numerical method for mantle convection with depth-dependent properties. *Journal of Computational Physics*, *113*(1), pp.62-74.

Barr, A.C. and Showman, A.P., (2009). Heat transfer in Europa's icy shell. In *Europa* (pp. 405-430). University of Arizona Press Tucson.

Bills, B. G. (2005). Free and forced obliquities of the Galilean satellites of Jupiter. *Icarus*, *175*, 233-247.

Belton, M. J. S., and 33 colleagues (1996). Galileo's first images of Jupiter and the Galilean satellites. *Science* 274, 377–385.

Bierhaus, E.B., Zahnle, K., & Chapman, C.R. (2009). Europa's crater distributions and surface ages. In *Europa*, edited by R.T. Pappalardo, W.B. McKinnon & K.K. Khurana, Univ. Ariz. Press, 161-180.

Buck, W. R. (2006). The role of magma in the development of the Afro-Arabian Rift System. *GeologicalSociety, London, Special Publications*, *259*, 43-54.

Collins, G.C., Prockter, L. M., Patterson, G. W., Kattenhorn, S. A., Rhoden, A. R., Cooper, C. M. (2016). Reconstructions on Plate-like Motions provide clues to the behavior of Europa's Ice Shell. *48th LPSC*, LPI contribution no. 2083, p. 2094.

Collins, G., Nimmo, F. (2009). Chaotic terrain on Europa. In *Europa*, edited by R.T. Pappalardo, W.B. McKinnon, and K.K. Khurana, University of Arizona Press, Tucson, AZ, pp 259– 282.

Collins, G.C., Cutler, B. B., Brenes Coto, J. P., Prockter, L. M., Patterson, G. W., Kattenhorn, S. A., Rhoden, A. R., Cooper, C. M. (2016) Plate Motions on Europa from Castalia Macula to Falga Regio. *47th LPSC*, LPI contribution no. 1903, p.2533.

Culha, C., Hayes, A.G., Manga, M. and Thomas, A.M., (2014). Double ridges on Europa accommodate some of the missing surface contraction. *Journal of Geophysical Research: Planets*, *119*(3), pp.395-403.

Cronin, V. S. (1992). Types and kinematic stability of triple junctions. *Tectonophysics*, *207*, 287-301.

Crummett, W.P. and Western, A.B., (1994). *University physics: models and applications*. Wm. C. Brown.

Cutler, B., Collins, G., Prockter, L.M., Patterson, G.W., Kattenhorn, S.A., Rhoden, A., Cooper, C.M. **(**2015). Reconstructing plate motions on Europa with GPlates. *Eos, Trans. AGU* 96, Fall Meet. Suppl., Abstract P31B-2059.

Cutler, B., Collins, G.C., Prockter, L.M., Patterson, G., Kattenhorn, S.A., Figueredo, P.H., Greeley, R. (2004). Resurfacing history of Europa from pole-to-pole geological mapping. *Icarus* 167, 287–312.

Dombard, A. J., Patterson, G. W., Lederer, A. P., & Prockter, L. M. (2013). Flanking fractures and the formation of double ridges on Europa. *Icarus*, *223*, 74-81.

Euler, L. (1775). *Formulae* generales *pro* translatione quacunque corporum rigidorum. *Commentarii Academiae Scientiarum Imperalis Petropolitanae*, *20*, 189-207.

Figueredo, P.H., Chuang, F.C., Rathbun, J., Kirk, R.L. and Greeley, R.,(2002). Geology and origin of Europa's "Mitten" feature (Murias Chaos). *Journal of Geophysical Research: Planets*, *107*(E5).

Geissler, P. E., R. Greenberg[1], G. Hoppa, P. Helfenstein[2], A. McEwen, R. Pappalardo, R. Tufts, M. Ockert-Bell, R. Sullivan, R. Greeley, M. J. S. Belton[4], T. Denk, B. Clark, J. Burns, J. Veverka & the Galileo Imaging Team, (1998). Evidence for non-synchronous rotation of Europa. *Nature*, 391,368-370.

Goodman, J.C. and Lenferink, E., (2012). Numerical simulations of marine hydrothermal plumes for Europa and other icy worlds. *Icarus*, *221*(2), pp.970-983.

Greeley, R., 17 colleagues, (2000). Geologic mapping of Europa. *J. Geophys. Res.* 105.

Greenberg, R., Hoppa, G.V., Bart, G., Hurford, T.,(2003). Tidal stress patterns on Europa. Celest. Mech. *Dyn. Astron*, 87, 171–188.

Harada, Y. and Kurita, K., (2006). The dependence of surface tidal stress on the internal structure of Europa: The possibility of cracking of the icy shell. *Planetary and Space Science*, *54*(2), pp.170-180.

Hatcher, R.D., (1995). *Structural geology: Principles, concepts, and problems*. Macmillan Publishing Company.

Hoppa, G.V., Tufts, B.R., Greenberg, R., Hurford, T.A., O'Brien, D.P., Geissler, P.E. (2001). Europa's rate of rotation derived from the tectonic sequence in the Astypalaea region. *Icarus*, 153, 208–213.

Hurford T. A., Beyer R. A., Schmidt B., Preblich B., Sarid A. R.,and Greenberg, R. (2005). Flexure of Europa's lithosphere due to ridge-loading. *Icarus, 177,* 380–396.

Jackson, J. A., Molnar, P., (1990). Active faulting and block rotations in the Western Transverse Ranges, California, *J. Geophys. Res*. 95.

Kattenhorn, S., Hurford, T. (2009). Tectonics of Europa. In *Europa*, edited by R.T. Pappalardo, W.B. McKinnon, and K.K. Khurana, University of Arizona Press, Tucson, AZ, pp 199– 236.

Kattenhorn, S. A., Prockter, L.M. (2014). Evidence for subduction in the ice shell of Europa, Nat. Geosci., 7, 762–767.

Kargel, Jeffrey S.; Kaye, Jonathan Z.; Head, James W., III; Marion, Giles M.; Sassen, Roger; Crowley, James K.; Ballesteros, Olga Prieto; Grant, Steven A.; Hogenboom, David L. (2000). Europa's Crust and Ocean: Origin, Composition, and the Prospects for Life. *Icarus*, 148, 226–265.

Katz, R. F., Ragnarsson, R., & Bodenschatz, E. (2005). Tectonic microplates in a wax model of sea-floor spreading. *New Journal of Physics*, *7*, 37.

Khurana, K.K., M. G. Kivelson, D. J. Stevenson, G. Schubert, C. T. Russell, R. J. Walker & C. (1998). Induced magnetic fields as evidence for subsurface oceans in Europa and Callisto. *Nature*, 395, 777- 780.

Klein, E.M., Smith, D.K., Williams, C.M. and Schouten, H., (2005). Counter-rotating microplates at the Galapagos triple junction. *Nature*, *433*(7028), p.855.

Lamb, S.H., (1987). A model for tectonic rotations about a vertical axis. *Earth and Planetary Science Letters*, *84*(1), pp.75-86.

Lamb, S.H., (1988). Tectonic rotations about vertical axes during the last 4 Ma in part of the New Zealand plate-boundary zone. *Journal of structural geology*, *10*(8), pp.875-893.

Lamb, S.H. and Bibby, H.M., 1989. The last 25 Ma of rotational deformation in part of the New Zealand plate-boundary zone. *Journal of structural geology*, *11*(4), pp.473-492.

Larson, R.L., Searle, R.C., Kleinrock, M.C., Schouten, H., Bird, R.T., Naar, D.F., Rusby, R.I., Hooft, E.E. and Lasthiotakis, H., 1992. Roller-bearing tectonic evolution of the Juan Fernandez microplate. *Nature*, *356*(6370), p.571.

McKenzie, D. P., & Morgan, W. J. (1969). Evolution of triple junctions. *Nature*, *224*, 125-133.

McKenzie, D. and Jackson, J., (1983). The relationship between strain rates, crustal thickening, palaeomagnetism, finite strain and fault movements within a deforming zone. *Earth and Planetary Science Letters*, *65*(1), pp.182-202

Nimmo, F. and Manga, M., (2009). Geodynamics of Europa's icy shell. In *Europa* (pp. 381-404). University of Arizona Press Tucson.

Nimmo, F. (2004). Dynamics of rifting and modes of extension on icy satellites. J. Geophys. Res., 109, E01003

Naar, D.F. and Hey, R.N., (1991). Tectonic evolution of the Easter microplate. *Journal of Geophysical Research: Solid Earth*, *96*(B5), pp.7961-7993.

Nimmo, F., (2004). Stresses generated in cooling viscoelastic ice shell: Application to Europa. *J. Geophys. Res.* 109.

Nimmo, F., Manga, M. (2009). Geodynamics of Europa's icy shell. In: Pappalardo, R., McKinnon, W., Khurana, K. (Eds.), Europa. Arizona Press Space Science Series, pp. 119–134.

Pappalardo, R.T., Head, J.W., Greeley, R., Sullivan, R.J., Pilcher, C., Schubert, G., Moore, W.B., Carr, M.H., Moore, J.M., Belton, M.J.S., Goldsby, D.L. (1998). Geological evidence for solid-state convection in Europa's ice shell. Nature 391, 365–367.

Pappalardo, R. T., & Sullivan, R. J. (1996). Evidence for separation across a gray band on Europa. *Icarus*, *123*, 557-567.

Patterson, G.W. and Pappalardo, R.T., (2002), March. Compression across ridges on Europa. In *Lunar and Planetary Science Conference* (Vol. 33).

Parro, L.M., Ruiz, J. and Pappalardo, R.T., (2016). Timing of chaotic terrain formation in Argadnel Regio, Europa, and implications for geological history. *Planetary and Space Science*, *130*, pp.24-29.

Peale S. J. and Lee M. H. (2002). A primordial origin of the Laplace relation among the Galilean satellites. *Science*, 298, 593–597.

Perkins R. P. Patterson G. W. Prockter L. M. Collins G. C. Kattenhorn S. A. (2017). An Analysis of Plate Motions on Europa Associated with the Formation of Astypalaea and Libya Lineae *48th LPSC*. p.2576.

Prockter, L. M., Shirley, J. H., Dalton, J. B., & Kamp, L. (2017). Surface composition of pull-apart bands in Argadnel Regio, Europa: Evidence of localized cryovolcanic resurfacing during basin formation. *Icarus*, *285*, 27-42.

Prockter, L.M., Head, J.W., Pappalardo, R.T., Sullivan, R.J., Clifton, A.E., Giese, B., Wagner, R. and Neukum, G., (2002). Morphology of Europan bands at high resolution: A mid-ocean ridge-type rift mechanism. *Journal of Geophysical Research: Planets*, *107*(E5).

Prockter, L.M. and Pappalardo, R.T., (2000). Folds on Europa: Implications for crustal cycling and accommodation of extension. *Science*, *289*(5481), pp.941-943.

Randall, K., Lamb, S. and Mac Niocaill, C., (2011). Large tectonic rotations in a wide zone of Neogene distributed dextral shear, northeastern South Island, New Zealand. *Tectonophysics*, *509*(3-4), pp.165-180.

Reinbolt, J., (2013). *Instantaneous Center of Zero Velocity*. PDF. Mechanical Engineering 231. University of Tennessee, Knoxville. September 19, 2013.

Rezza C. A. Collins G. C. Prockter L. M. Patterson G. W. Rhoden A. R. (2017). Multi-Stage Reconstruction of Plate Motions South of Castalia Macula, Europa. *48th LPSC*. p.2283

Riley, J., Hoppa, G.V., Greenberg, R., Tufts, B.R. and Geissler, P., (2000). Distribution of chaotic terrain on Europa. *Journal of Geophysical Research: Planets*, *105*(E9), pp.22599-22615.

Rudolph, M.L. and Manga, M., (2012). Effects of anisotropic viscosity and texture development on convection in ice mantles. *Journal of Geophysical Research: Planets*, *117*(E11).

Sarid, A.R., Greenberg, R., Hoppa, G.V., Hurford, T.A., Tufts, B.R. and Geissler, P., (2002). Polar wander and surface convergence of Europa's ice shell: Evidence from a survey of strike-slip displacement. *Icarus*, *158*(1), pp.24-41.

Schenk, P. M., & McKinnon, W. B. (1989). Fault offsets and lateral crustal movement on Europa: Evidence for a mobile ice shell. *Icarus*, *79*, 75-100.

Schenk, P., Pappalardo R. T. (2004) Topographic variations in chaos on Europa: Implications for diapiric formation. Geophys. Res. Lett., 31.

Schenk, P., Matsuyama, I., & Nimmo, F. (2008). True polar wander on Europa from global-scale small-circle depressions. *Nature*, *453*, 368.

Schmidt, B. E., Blankenship, D. D., Patterson, G. W., & Schenk, P. M. (2011). Active formation of' chaos terrain' over shallow subsurface water on Europa. *Nature*, *479*, 502.

Schouten, H., Klitgord, K.D. and Gallo, D.G. (1993). Edge driven microplate kinematics. *J. Geophys. Res*. 98.

Schubert, G., Turcotte, D.L. and Olson, P., (2001). *Mantle convection in the Earth and planets*. Cambridge University Press.

Schulson, E.M., (2001). Brittle failure of ice. *Engineering fracture mechanics*, *68*(17-18), pp.1839-1887.

Smith, B. A., L. A. Soderblom, T. V. Johnson, A. P. Ingersoll, S. A. Collins, E. M. Shoemaker, G. E. Hunt, H. Masursky, M. H. Carr, M. E. Davies, A. F. Cook II, F. Boyce, G. E. Danielson, T. Owen, C. Sagan, R. F. Beebe, F. Veverka, R. G. Shom, J. F. McCauley, D. Morrison, G. A. Briggs, V. E. Suomi, (1979). The Jupiter system through the eyes of Voyager 1. *Science*, 203, 13–31.

Soderlund, K. M., Schmidt, B. E., Wicht, J., & Blankenship, D. D. (2014). Ocean-driven heating of Europa's icy shell at low latitudes. *Nature Geoscience*, *7*, 16.

Sotin, C., Tobie, G., Wahr, J., McKinnon, W.B., McKinnon, W.B. and Khurana, K.K., (2009). Tides and tidal heating on Europa. *Europa, edited by RT Pappalardo, WB McKinnon, and KK Khurana, University of Arizona Press, Tucson*, pp.85-118.

Spaun, N.A., Head, J.W., Collins, G.C., Prockter, L.M. and Pappalardo, R.T., (1998). Conamara Chaos region, Europa: Reconstruction of mobile polygonal ice blocks. *Geophysical research letters*, *25*(23), pp.4277-4280.

Stempel M. M., Barr A. C., and Pappalardo R. T. (2005) Model constraints on the opening rates of bands on Europa. Icarus, 177, 297–304.

Turcotte, D. L., and Schubert, J. (2014). *Geodynamics, third edition*. New York, Wiley

Schubert, G., Turcotte, D.L. and Olson, P., (2001). *Mantle convection in the Earth and planets*. Cambridge University Press.

APPENDIX

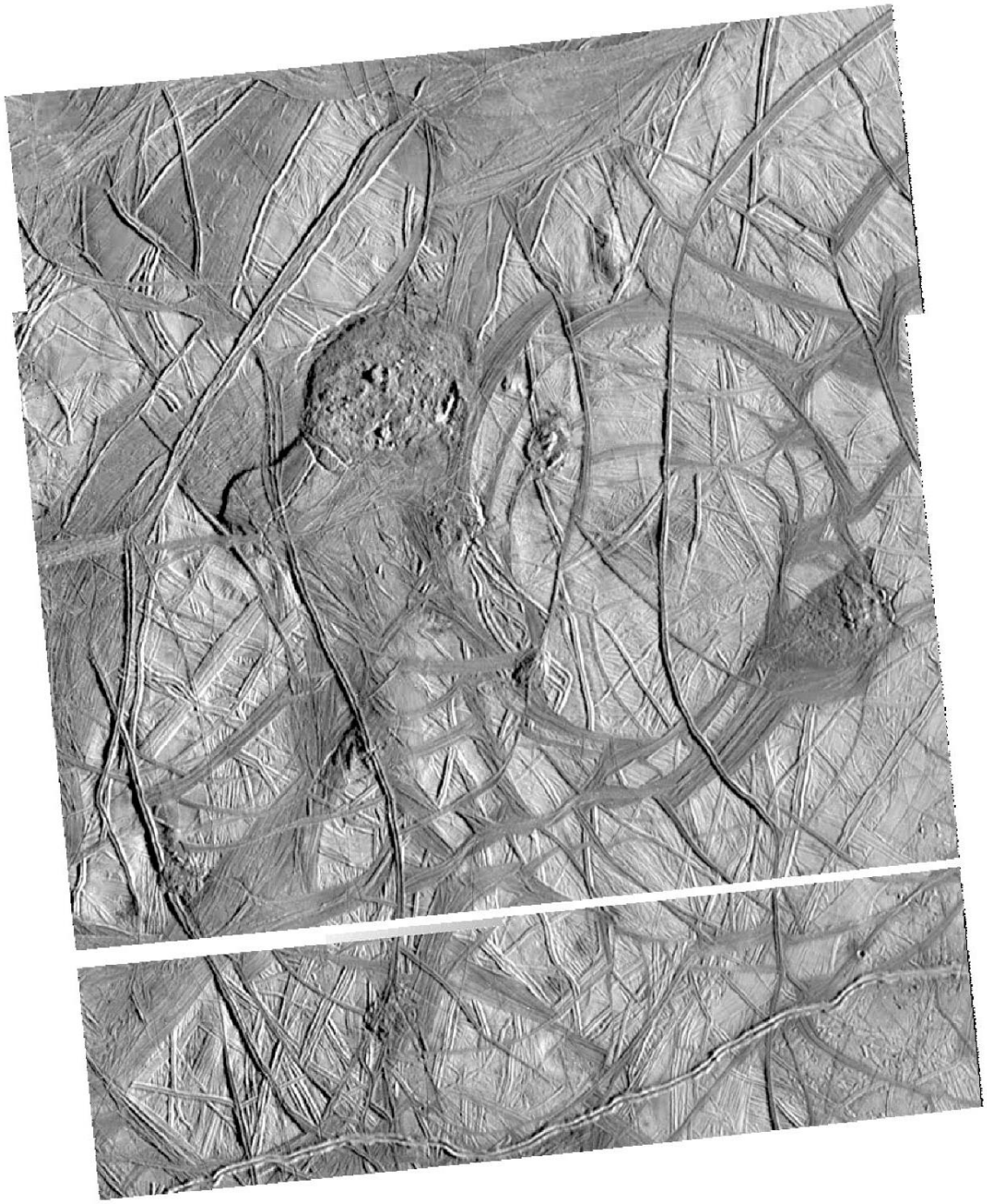

Figure A: *Sinusoidal projected mosaic of western Argadnel Regio from images E17ESREGMAP01(s-clock number* s0466664226, and s0466664239). *Processed in ISIS3.*

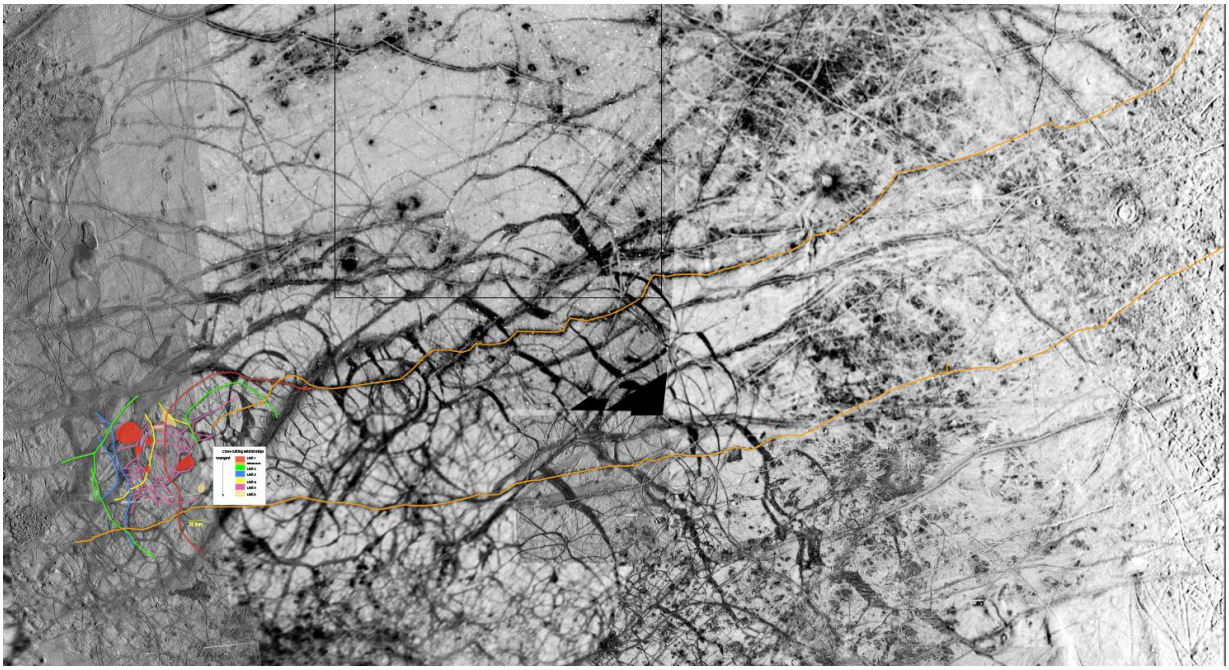

Figure B: *Extended view of the cross-cutting relationship map (Fig.9). The reference double ridges are symbolized by the orange polylines and extend approximately 1600 km. The reference double ridges are cross-cut by features in Episode 1 and cross-cut features in Episode 2 and 3.*

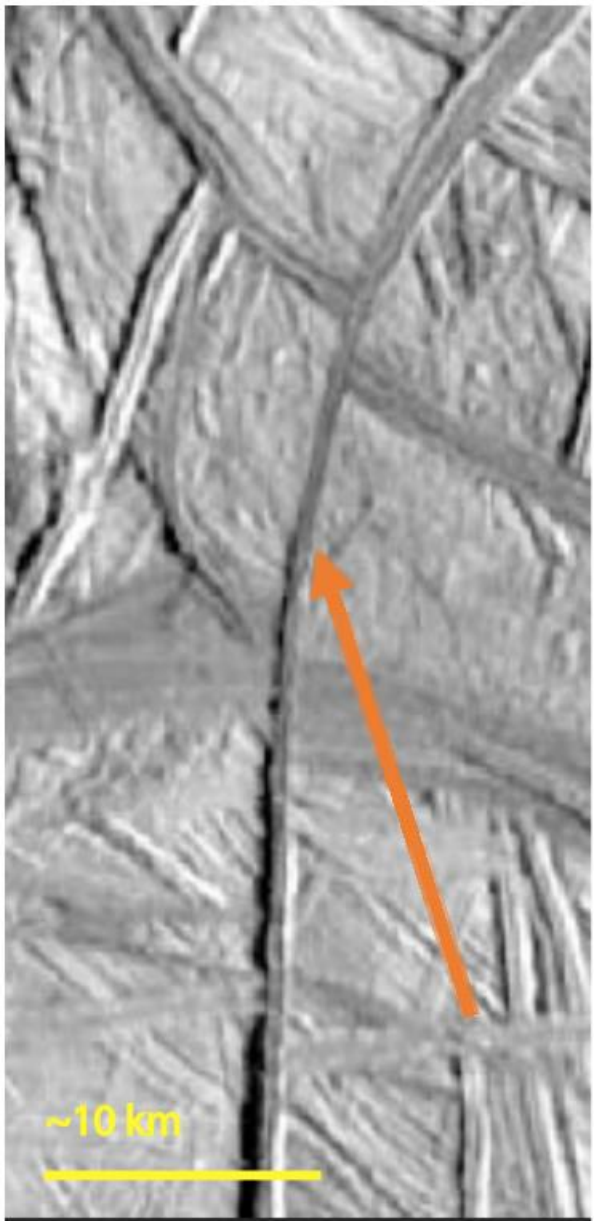

***Figure C**: Zoomed in view of the double ridge in Episode 1 that transforms into a band.*

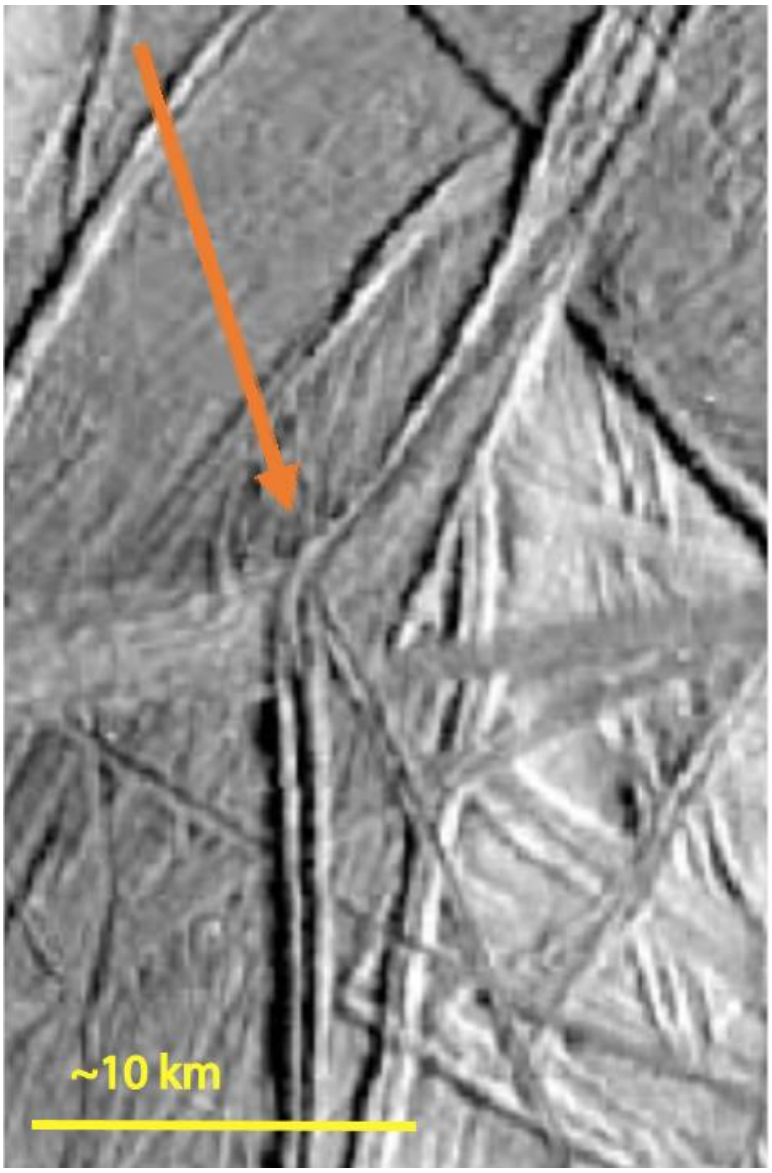

***Figure D**: Zoomed in view that displays the two distinct morphologies near a triple junction with lower albedo, band-like feature Episode 2.*

***Figure E**: Zoomed in view of the double ridge in Episode 4 that transforms into a small section of a ridge complex.*

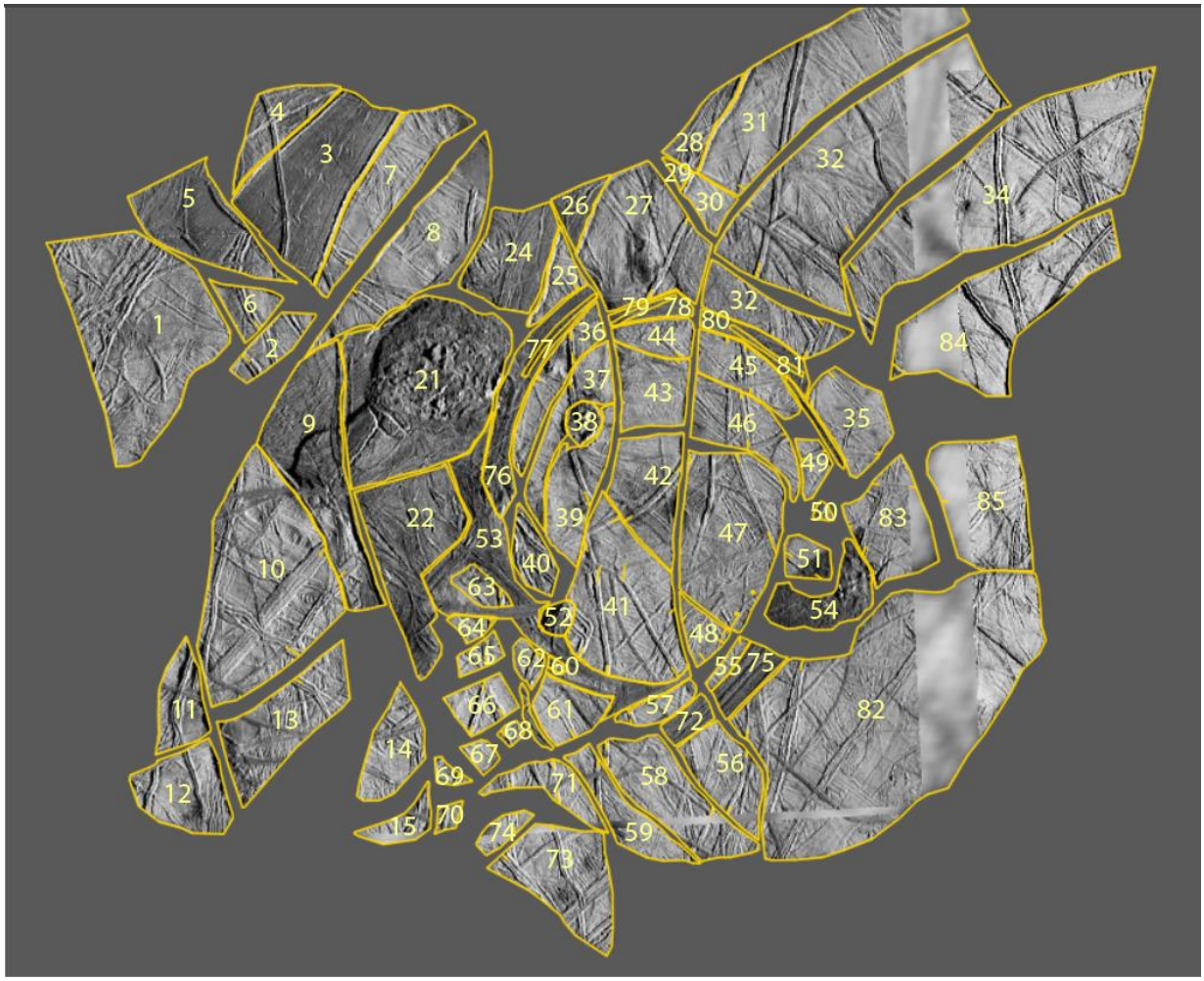

Figure F: *Defined plates in GPlates. Yellow numbers correlate to plate identification number. Plates are outlined by yellow polylines. Plates 21, 38, 52-54, and 75-81 represent bands and chaos terrain.*

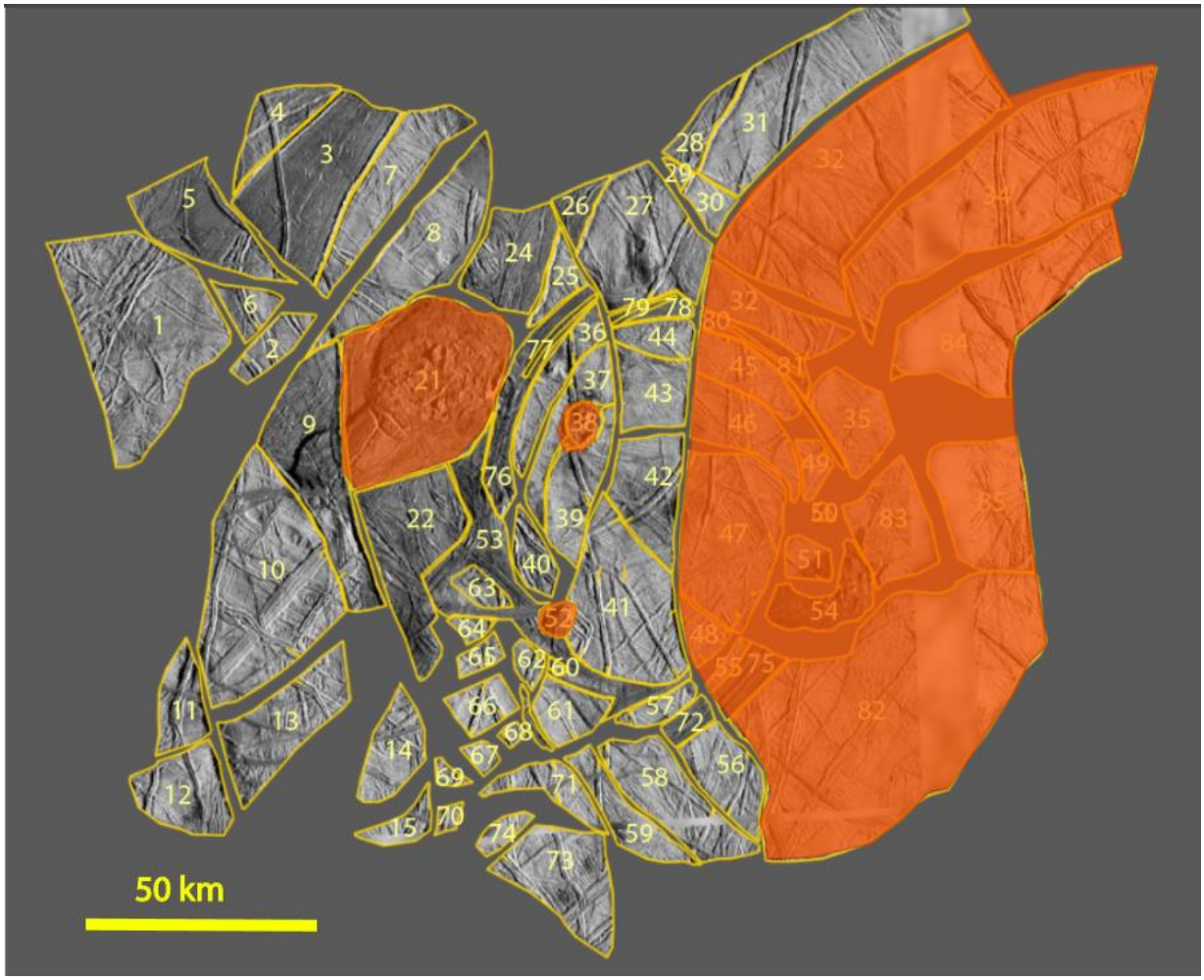

Figure G.1: *Illustration of active surfaces from t = 0 to t = -10. Active surfaces are symbolized by red polygons.*

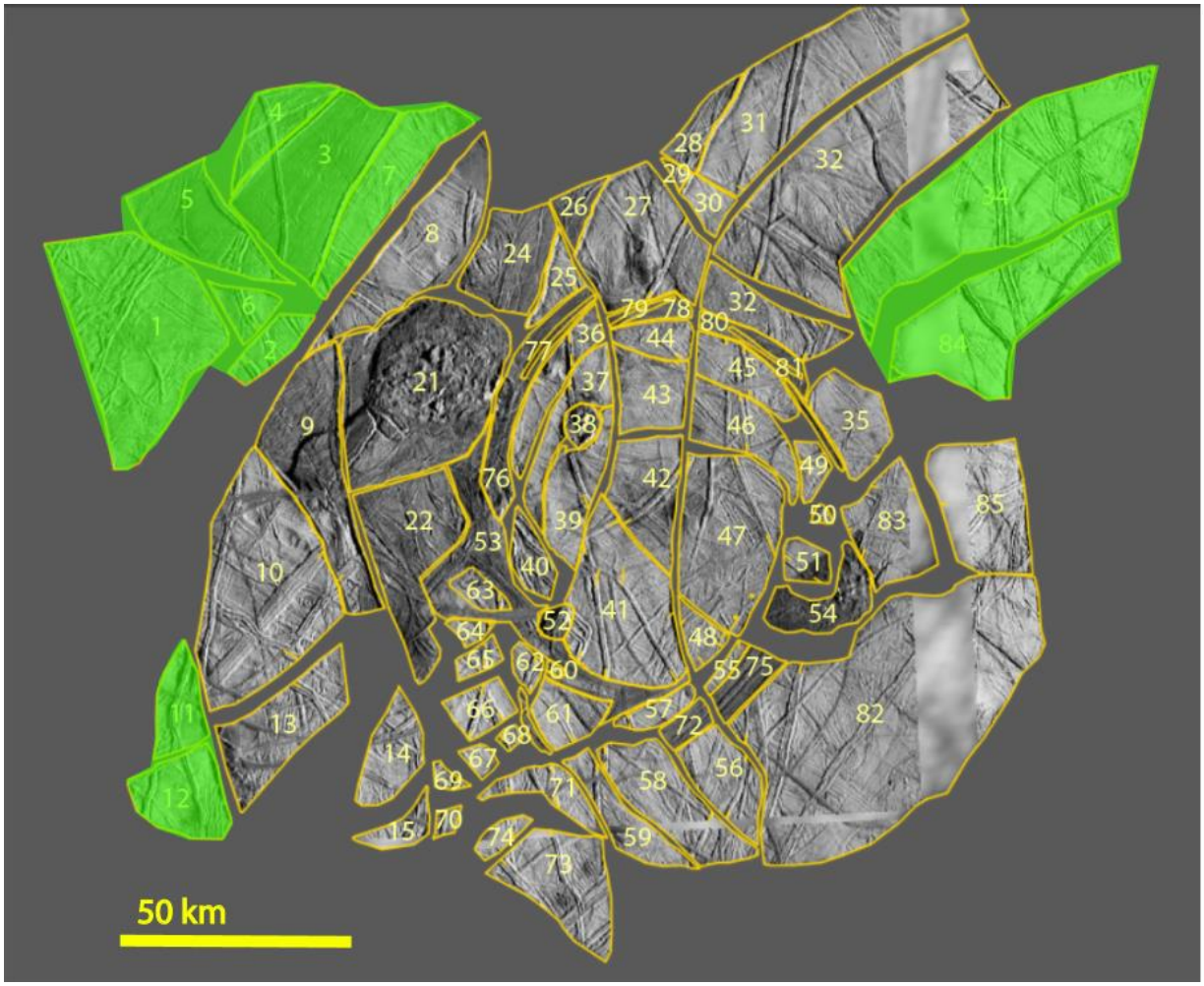

Figure G.2: *Illustration of active surfaces from t = -10 to t = -20. Active surfaces are symbolized by green polygons.*

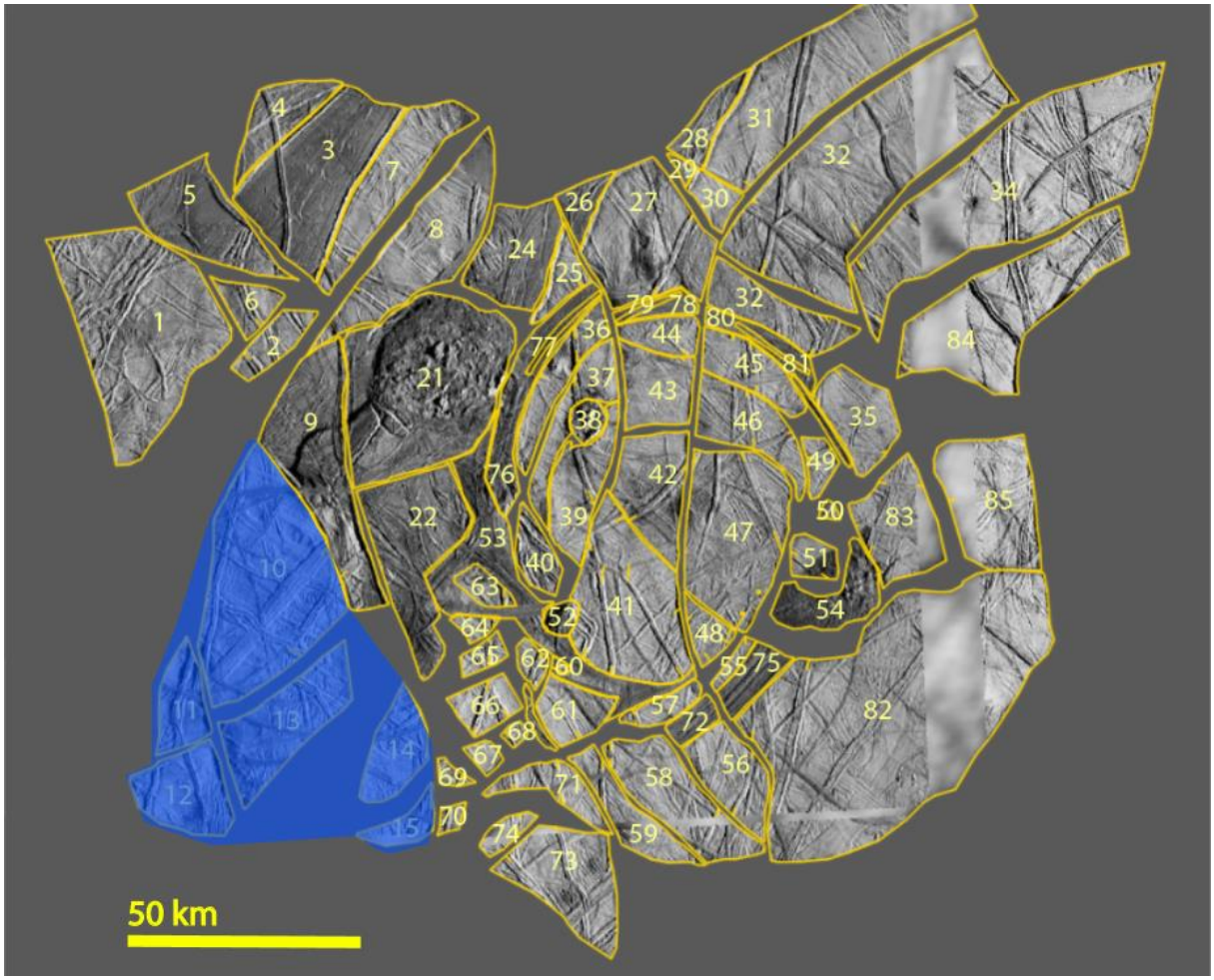

Figure G.3: *Illustration of active surfaces from t = -20 to t = -30. Active surfaces are symbolized by blue polygons.*

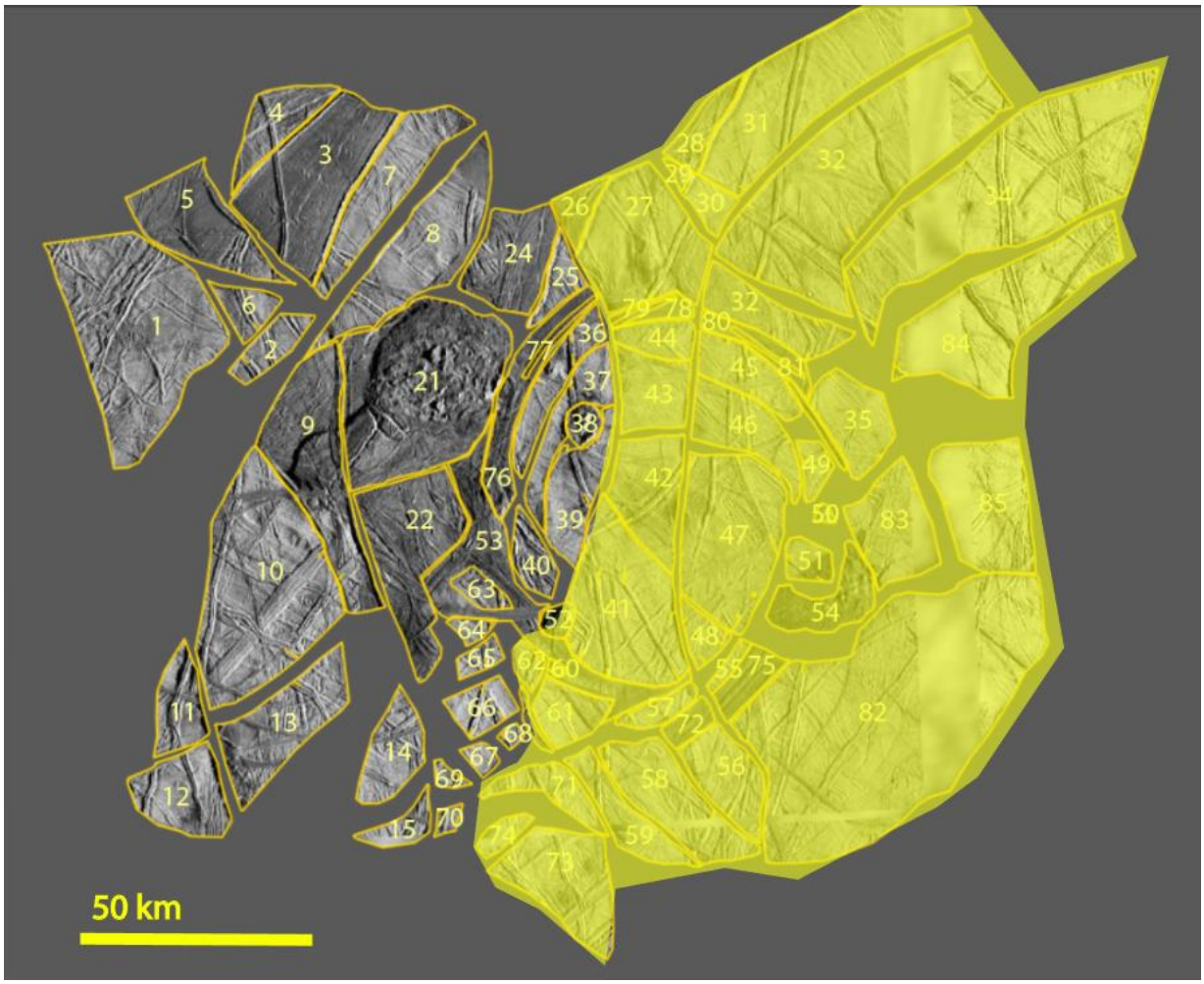

Figure G.4: *Illustration of active surfaces from t = -30 to t = -40. Active surfaces are symbolized by yellow polygons.*

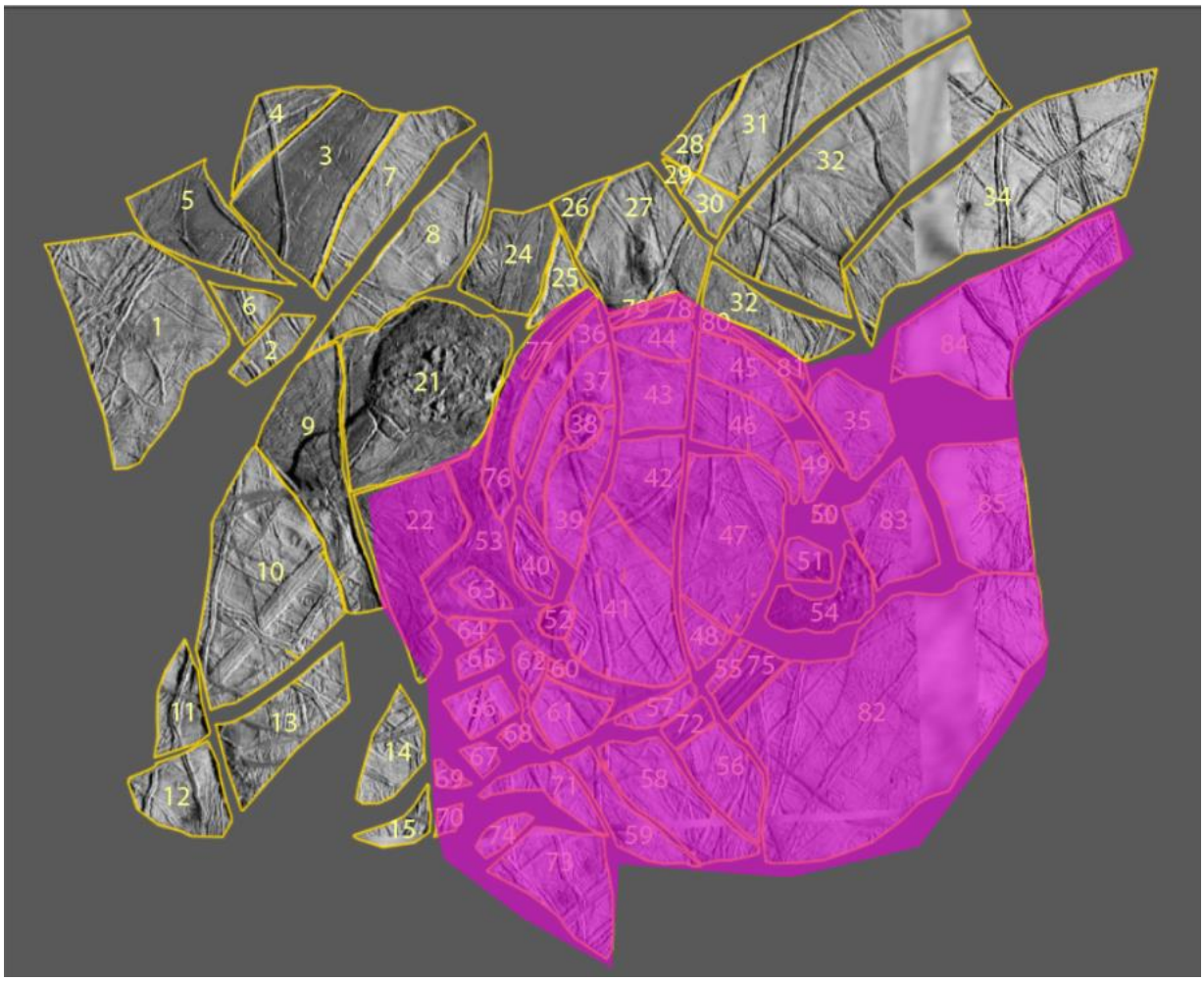

Figure G.5: *Illustration of study area at t = -40 to t = -50. Active surfaces are symbolized by the pink polygon.*

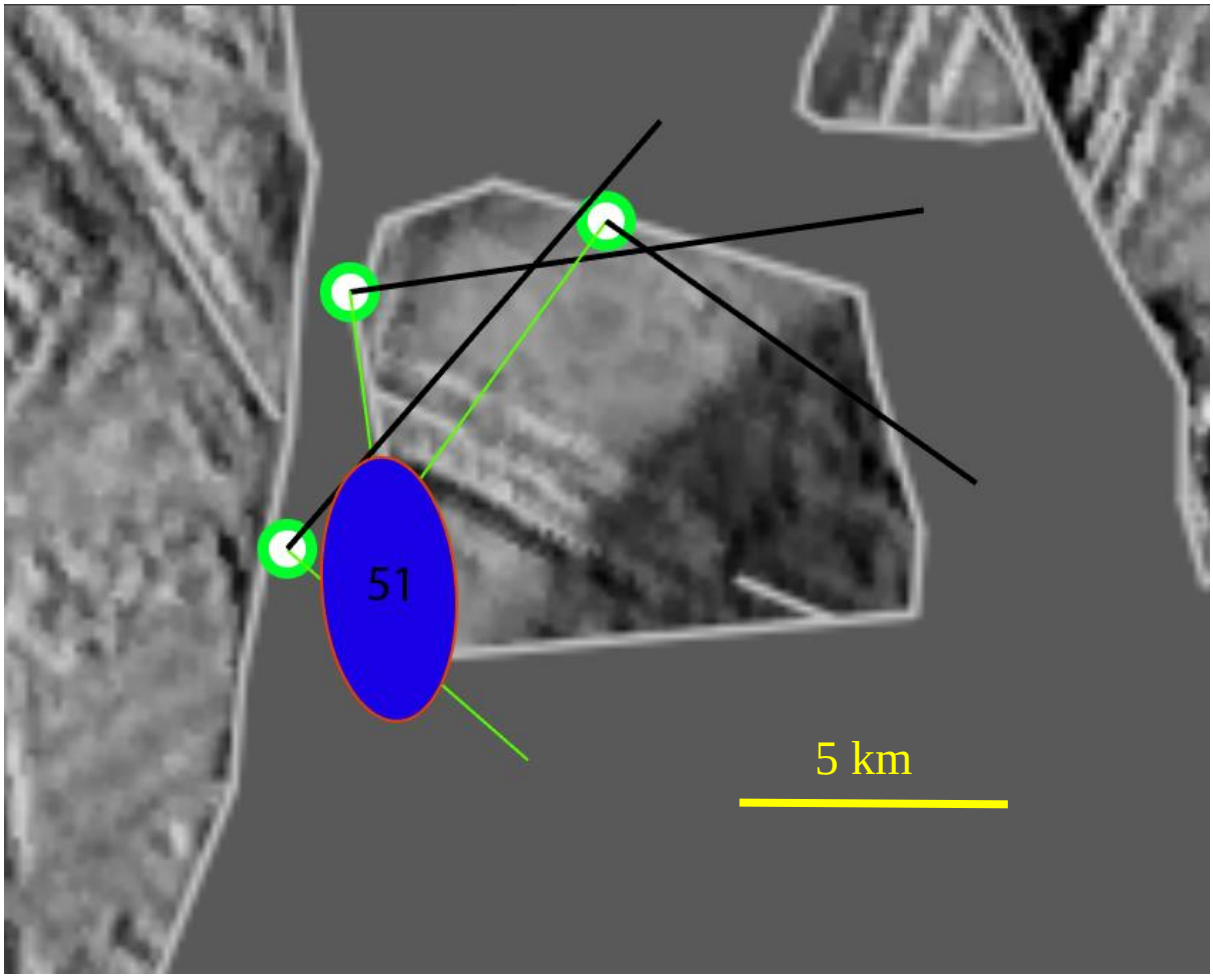

Figure H: *Plate 51 to the east of the CF. The white circles with green borders indicate markers for measurements. Black lines represent vectors. Green lines represent normal lines projected from vector tails. The blue ellipse represents the IARs. Plate 51 rotated ~100° clockwise as the CF rotated anticlockwise.*

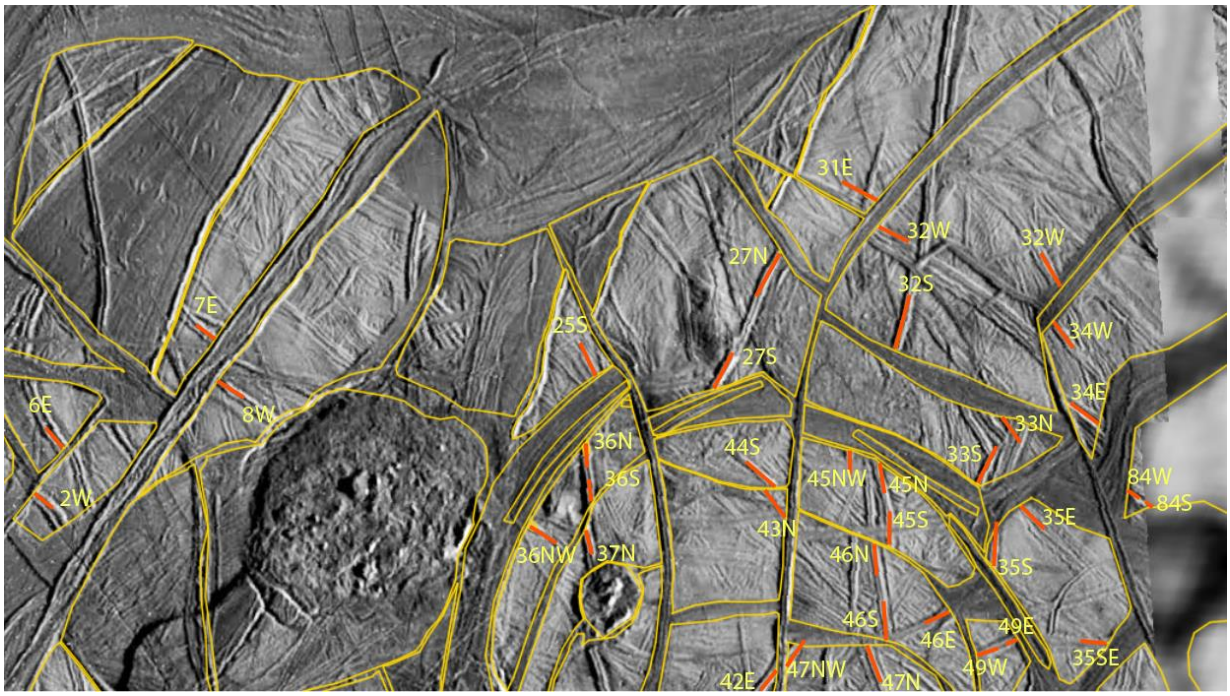

Figure I.1: *Piercing point locations recorded in GPlates in the northern portion of the study area. The yellow numbers and characters refer to plate ID number and approximate geographic location on the plate. The changes in distance over all timesteps are located on Table A.*

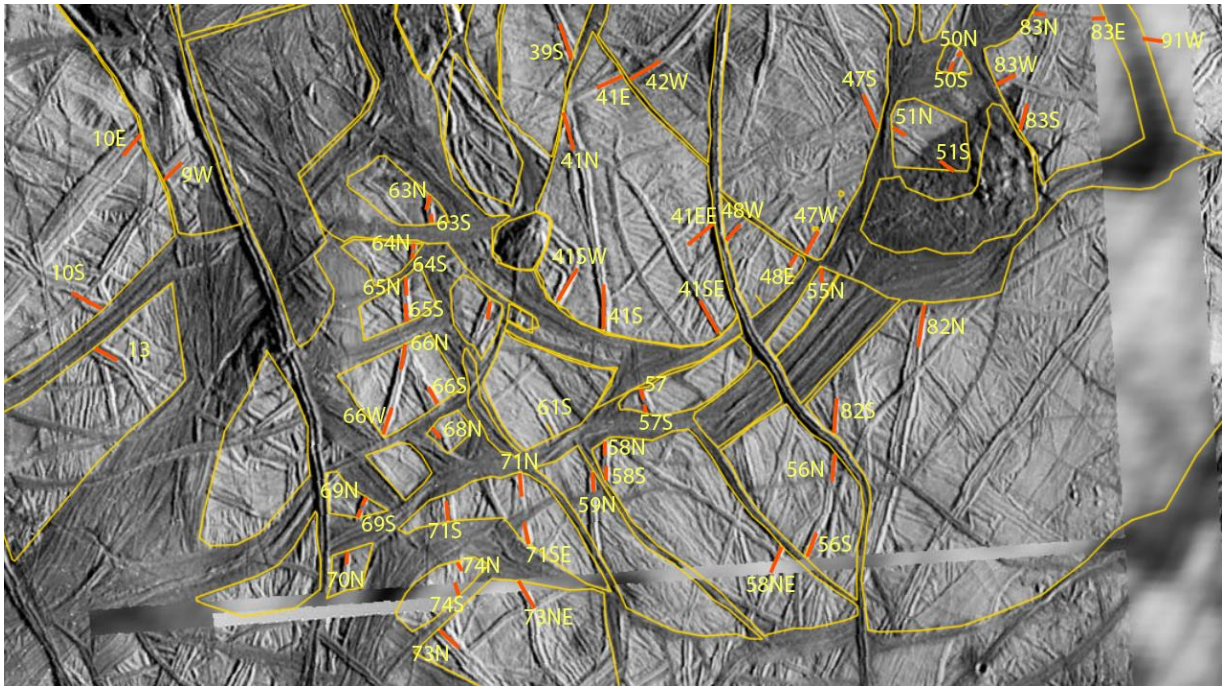

Figure I.2: *Piercing point locations recorded in GPlates in the southern portion of the study area. The yellow numbers and characters refer to plate ID number and approximate geographic location on the plate. The changes in distance over all timesteps are located on Table A.*

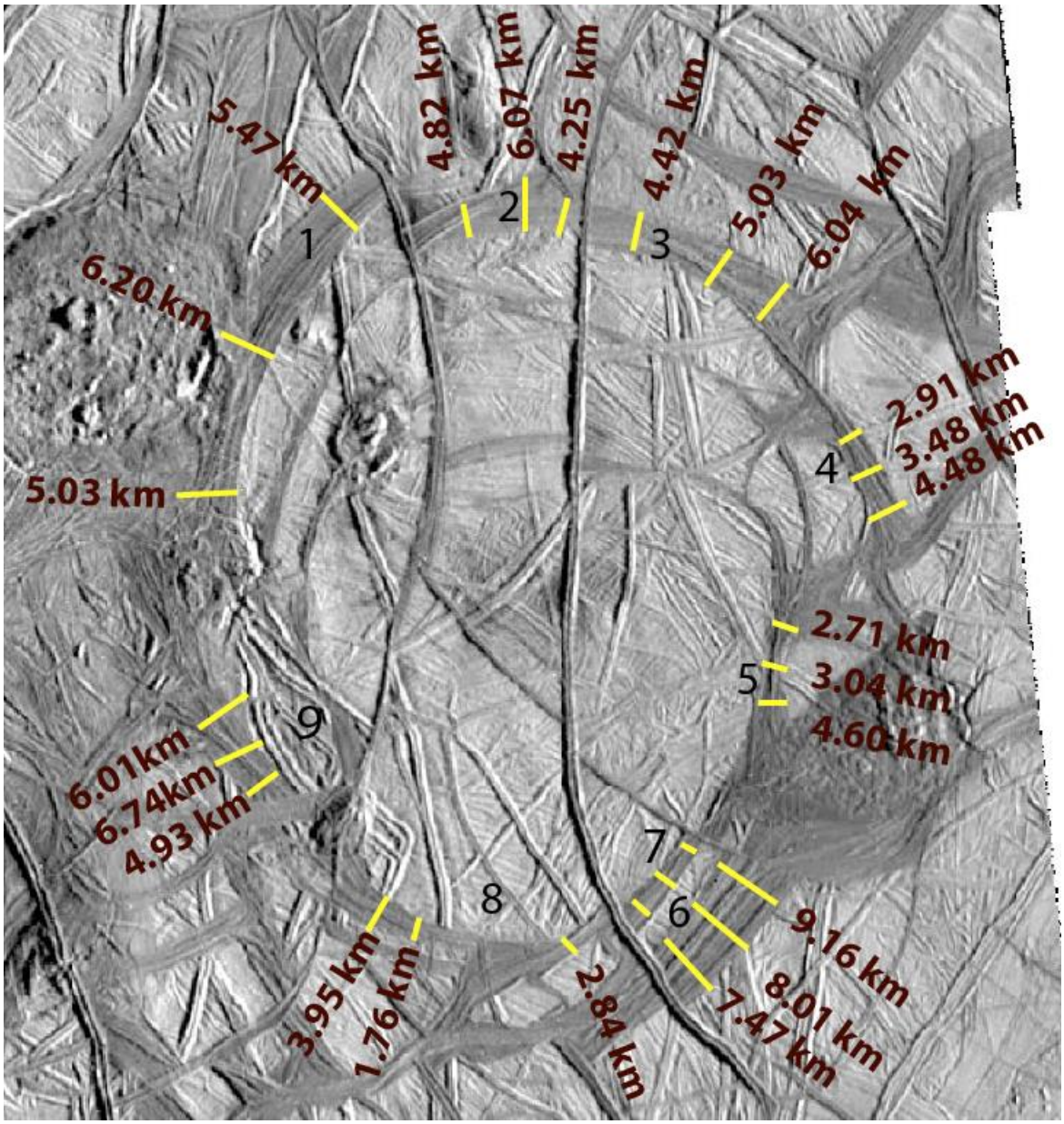

Figure J: *Band measurements around the CF (Appendix Table.C). Black number correlate to band ID measurement number. Yellow lines indicate place of measurement along the width of bands. Brown numbers correlate to measurements.*

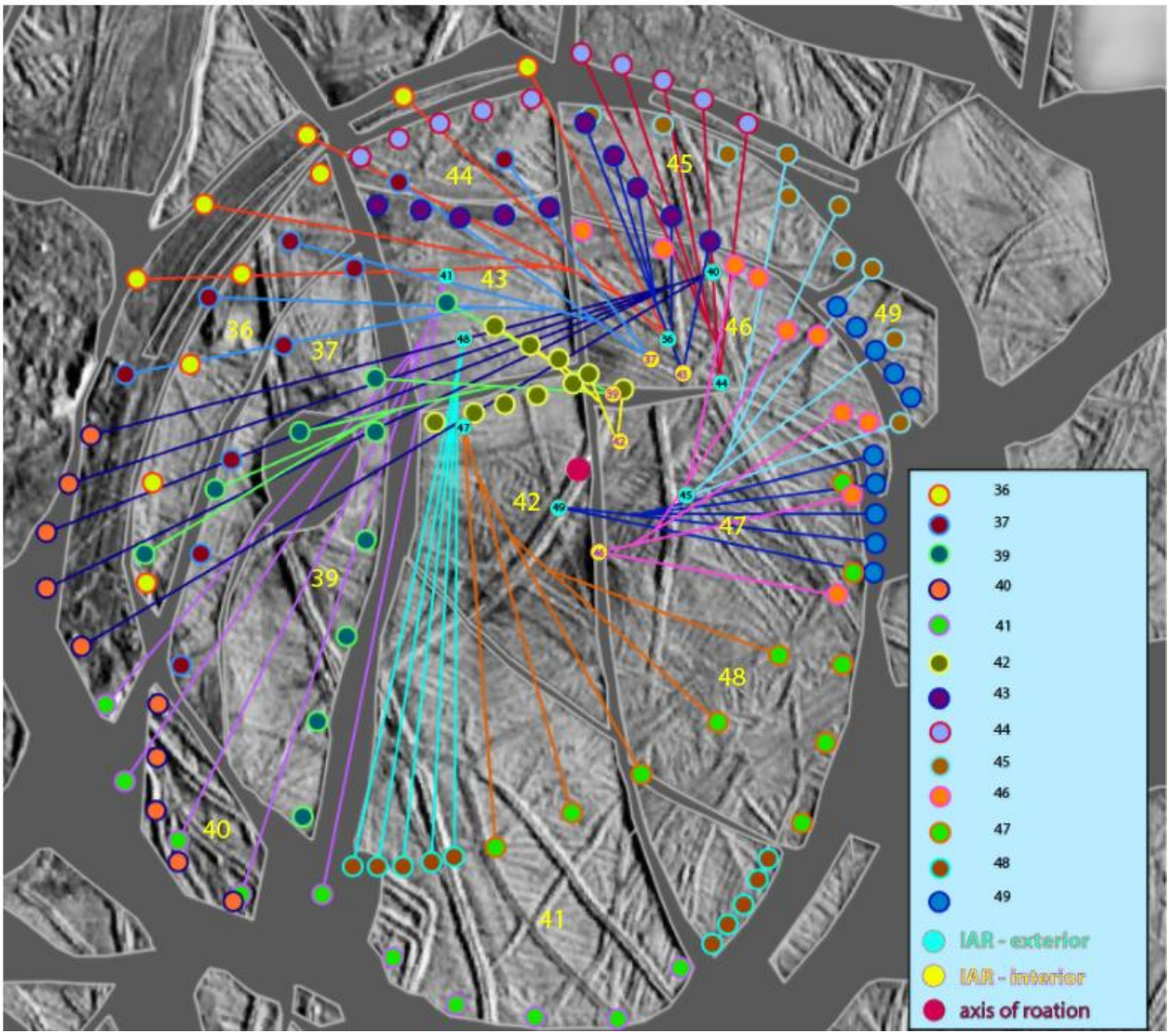

Figure K: *CF at t = -40. IAR location illustration with displacement markers, and normal lines at t = -40. Yellow numbers on image indicate plate ID. Black numbers in key correspond to plate number/adjacent symbol that was used as a marker at t = -50, and t =-40. Numbered circles in within the CF indicate the furthest IAR location of the associated parent plate. The axis of rotation was determined by observing that the latitude and longitude of the area marked by the red circle did not change during t = -50 to t =-40.*

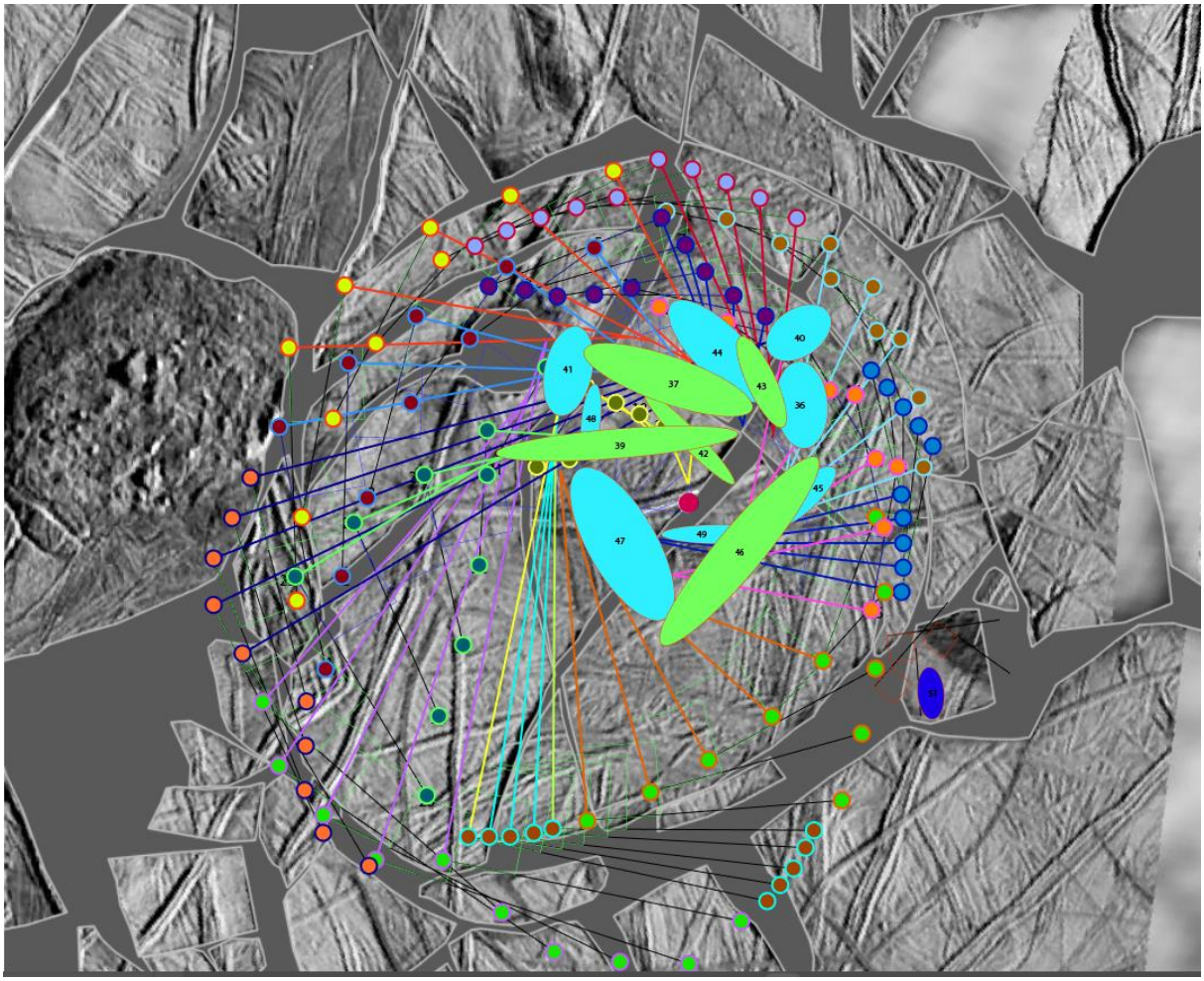

Figure L: *CF at t = -50. IAR location illustration with displacement markers, squares for alignment, vectors, and normal lines. IARs locations are symbolized by ellipses.*

TABLE A. *Complete table of piercing point measurements from GPlates. Measurements were tracked in GPlates with the "Kinematics Tool". Change in distance for each timestep was calculated by subtracting distances of the younger timestep from the older. For example, distances from piercing points at t = -40 were subtracted from distances at t = -50. Distances change was only reported in rows of the first listed piercing point pair.*

Pair	Ppoint	Timestep	lat	lon	Distance Total	Δ Distance
31E, 32W	31E	50	-9.6646	139.111	0.272019866	0
	31E	40	-10.0306	139.5035	3.443823303	3.1718034
	31E	30	-10.4289	139.6134	1.595046823	-1.8487765
	31E	20	-10.4289	139.6134	2.183342878	0.5882961
	31E	10	-10.4289	139.6134	2.183342878	0
	31E	0	-10.4289	139.6134	3.445424017	1.2620811
	32W	50	-9.6743	139.1134		
	32W	40	-10.1551	139.5257		
	32W	30	-10.4591	139.6644		
	32W	20	-10.4961	139.6578		
	32W	10	-10.4961	139.6578		
	32W	0	-10.5542	139.6308		
32s, 27N	32S	50	-10.2942	139.0454	1.695135828	0
	32S	40	-10.7627	139.6681	20.08087807	18.385742
	32S	30	-11.0716	139.7831	19.99547103	-0.085407
	32S	20	-11.1086	139.7766	20.38389884	0.3884278

Table A Continued

Pair	Ppoint	Timestep	lat	lon	Distance Total	Δ Distance
	32S	10	-11.1086	139.7766	20.38389884	0
	32S	0	-11.1667	139.7495	20.72311404	0.3392152
	27N	50	-10.3558	139.0365		
	27N	40	-10.4294	138.9993		
	27N	30	-10.6957	139.1412		
	27N	20	-10.6957	139.1412		
	27N	10	-10.6957	139.1412		
	27N	0	-10.6957	139.1412		
32E, 34W	32E	50	-10.1829	139.931	1.20107932	0
	32E	40	-10.3717	140.4684	5.066138206	3.8650589
	32E	30	-10.7109	140.5989	1.768570924	-3.2975673
	32E	20	-10.7479	140.5925	4.045762481	2.2771916
	32E	10	-10.7479	140.5925	4.045762481	0
	32E	0	-10.8061	140.5656	5.066852759	1.0210903
	34W	50	-10.2268	139.9351		
	34W	40	-10.557	140.4526		
	34W	30	-10.7758	140.5975		
	34W	20	-10.8955	140.5759		
	34W	10	-10.8955	140.5759		
	34W	0	-10.9907	140.5426		
34E, 84W	34E	50	-10.7822	140.0067	1.858979231	

Table A Continued

Pair	Ppoint	Timestep	lat	lon	Distance Total	Δ Distance
	34E	40	-11.0486	140.7254	3.075976712	1.2169975
	34E	30	-11.292	140.8182	9.715545012	6.6395683
	34E	20	-11.3968	140.8297	7.003899203	-2.7116458
	34E	10	-11.3968	140.8297	9.716835353	2.7129362
	34E	0	-11.4921	140.7964	9.716196794	-0.0006386
						-9.7161968
	84W	50	-10.8436	140.037		
	84W	40	-11.1432	140.7882		
	84W	30	-11.6218	140.9566		
	84W	20	-11.6218	140.9566		
	84W	10	-11.7173	140.9894		
	84W	0	-11.8126	140.9561		
84s, 33N	84S	50	-10.9734	140.1148	5.367491404	0
	84S	40	-11.2323	140.9119	18.32898847	12.961497
	84S	30	-11.7086	141.0823	21.87516872	3.5461803
	84S	20	-11.7086	141.0823	21.74061198	-0.1345567
	84S	10	-11.7961	141.1204	23.58956798	1.848956
	84S	0	-11.8914	141.0872	23.8317297	0.2421617
						-23.83173
	33N	50	-11.1461	140.2114		
	33N	40	-11.1386	140.2328		
	33N	30	-11.385	140.3323		
	33N	20	-11.4335	140.3177		

Table A Continued

Pair	Ppoint	Timestep	lat	lon	Distance Total	Δ Distance
	33N	10	-11.4335	140.3177		
	33N	0	-11.4802	140.2988		
33s, 45NW	33S	50	-11.4771	140.0907	1.43928405	0
	33S	40	-11.4796	140.1459	19.86104583	18.421762
	33S	30	-11.7225	140.232	19.13947822	-0.7215676
	33S	20	-11.771	140.2174	18.97321994	-0.1662583
	33S	10	-11.771	140.2174	18.97321994	0
	33S	0	-11.8177	140.1985	18.08918973	-0.8840302
	45NW	50	-11.526	140.0703		
	45NW	40	-11.3011	139.4249		
	45NW	30	-11.6307	139.5208		
	45NW	20	-11.6307	139.5208		
	45NW	10	-11.6307	139.5208		
	45NW	0	-11.679	139.5353		
45N, 35s	45N	50	-11.6442	140.1726	0.870777256	0
	45N	40	-11.3317	139.5798	20.94333507	20.072558
	45N	30	-11.686	139.6686	21.18232861	0.2389935
	45N	20	-11.686	139.6686	21.18232861	0
	45N	10	-11.686	139.6686	21.18232861	0
	45N	0	-11.7297	139.6849	20.97175822	-0.2105704
	35S	50	-11.6171	140.1899		
	35S	40	-11.5604	140.3286		
	35S	30	-12.1287	140.3218		
	35S	20	-12.1287	140.3218		
	35S	10	-12.1287	140.3218		

Table A Continued

Pair	Ppoint	Timestep	lat	lon	Distance Total	Δ Distance
	35S	0	-12.2239	140.2882		
35SE, 83N	35SE	50	-12.1553	140.6424	0.660607107	0
	35SE	40	-12.0117	140.871	6.117123997	5.4565169
	35SE	30	-12.4852	140.9347	6.959115668	0.8419917
	35SE	20	-12.4852	140.9347	6.959115668	0
	35SE	10	-12.4852	140.9347	6.959115668	0
	35SE	0	-12.5805	140.9013	6.959012311	-0.0001034
	83N	50	-12.1557	140.6672		
	83N	40	-12.2275	140.9344		
	83N	30	-12.7355	140.8825		
	83N	20	-12.7355	140.8825		
	83N	10	-12.7355	140.8825		
	83N	0	-12.8308	140.8491		
83E, 91W	83E	50	-12.2238	141.0403	0.620903297	0
	83E	40	-12.2819	141.3099	2.122869917	1.5019666
	83E	30	-12.741	141.2628	3.236404748	1.1135348
	83E	20	-12.741	141.2628	3.236404748	0
	83E	10	-12.741	141.2628	6.565558446	3.3291537
	83E	0	-12.8363	141.2295	6.565923325	0.0003649
	91W	50	-12.2281	141.0632		
	91W	40	-12.3303	141.3724		
	91W	30	-12.7766	141.379		

Table A Continued

Pair	Ppoint	Timestep	lat	lon	Distance Total	Δ Distance
	91W	20	-12.7766	141.379		
	91W	10	-12.8434	141.4865		
	91W	0	-12.9387	141.4533		
83W, 49E	83W	50	-12.4983	140.437	0.221827171	0
	83W	40	-12.5784	140.7175	21.9024028	21.680576
	83W	30	-13.1114	140.7146	23.57944365	1.6770409
	83W	20	-13.1114	140.7146	22.54048828	-1.0389554
	83W	10	-13.1114	140.7146	21.64891207	-0.8915762
	83W	0	-13.2066	140.6811	18.29667829	-3.3522338
	49E	50	-12.496	140.429		
	49E	40	-11.8779	140.3139		
	49E	30	-12.3495	140.2937		
	49E	20	-12.3868	140.3052		
	49E	10	-12.4175	140.3176		
	49E	0	-12.5793	140.4351		
83S, 50N	83S	50	-12.7461	140.5219	0.728903508	0
	83S	40	-12.8229	140.8119	8.54186177	7.8129583
	83S	30	-13.3415	140.8416	13.78299614	5.2411344
	83S	20	-13.3415	140.8416	13.78299614	0
	83S	10	-13.3415	140.8416	13.78299614	0
	83S	0	-13.4368	140.8081	13.78467815	0.001682

Table A Continued

Pair	Ppoint	Timestep	lat	lon	Distance Total	Δ Distance
	50N	50	-12.7716	140.5136		
	50N	40	-12.9469	140.5165		
	50N	30	-12.9469	140.5165		
	50N	20	-12.9469	140.5165		
	50N	10	-12.9469	140.5165		
	50N	0	-13.0421	140.4829		
49W, 46E	49W	50	-12.5476	140.2054	0.563318147	0
	49W	40	-12.0562	140.1748	3.188903877	2.6255857
	49W	30	-12.4876	140.1127	2.540667066	-0.6482368
	49W	20	-12.5204	140.1207	3.340008052	0.799341
	49W	10	-12.5478	140.1305	4.093789861	0.7537818
	49W	0	-12.6719	140.2257	6.999441739	2.9056519
	46E	50	-12.5331	140.1903		
	46E	40	-12.0004	140.0696		
	46E	30	-12.4248	140.0421		
	46E	20	-12.4248	140.0421		
	46E	10	-12.4248	140.0421		
	46E	0	-12.4564	140.0824		
51N, 50s	51N	50	-12.9091	140.4208	1.100464966	0
	51N	40	-13.3085	140.5091	6.957483536	5.8570186
	51N	30	-13.5375	140.5766	13.43675073	6.4792672

Table A Continued

Pair	Ppoint	Timestep	lat	lon	Distance Total	Δ Distance
	51N	20	-13.5375	140.5766	13.43675073	0
	51N		-13.5279	140.4595	12.79960735	-0.6371434
	51N	0	-13.4466	140.1359	11.05451159	-1.7450958
	50S	50	-12.8718	140.4367		
	50S	40	-13.0581	140.4576		
	50S	30	-13.0581	140.4576		
	50S	20	-13.0581	140.4576		
	50S	10	-13.0581	140.4576		
	50S	0	-13.1533	140.424		
51s, 82N	51s	50	-13.239	140.2013	3.698004295	0
	51s	40	-13.6888	140.4066	11.90729271	8.2092884
	51s	30	-13.8971	140.4131	9.449798777	-2.4574939
	51s	20	-13.8971	140.4131	9.449798777	0
	51s	10	-13.9098	140.3636	9.088451333	-0.3613474
	51s	0	-13.6567	140.4777	18.86527331	9.776822
	82N	50	-13.3747	140.1982		
	82N	40	-14.1024	140.2611		
	82N	30	-14.2428	140.384		
	82N	20	-14.2428	140.384		
	82N	10	-14.2428	140.384		
	82N	0	-14.338	140.3502		
45s, 46N	45s	50	-12.0387	140.0143	0.572527489	0

Table A Continued

Pair	Ppoint	Timestep	lat	lon	Distance Total	Δ Distance
	45s	40	-11.7372	139.7056	2.209348299	1.6368208
	45s	30	-12.1064	139.724	2.064356939	-0.1449914
	45s	20	-12.1064	139.724	2.064356939	0
	45s	10	-12.1064	139.724	2.064356939	0
	45s	0	-12.1481	139.754	2.065403195	0.0010463
	46N	50	-12.0573	140.0043		
	46N	40	-11.7392	139.6228		
	46N	30	-12.0916	139.648		
	46N	20	-12.0916	139.648		
	46N	10	-12.0916	139.648		
	46N	0	-12.1357	139.6775		
46s, 47N	46s	50	-12.5165	139.8329	1.092092253	0
	46s	40	-12.2035	139.779	2.344699369	1.2526071
	46s	30	-12.5754	139.7193	1.688000723	-0.6566986
	46s	20	-12.5754	139.7193	1.688000723	0
	46s	10	-12.5754	139.7193	1.688000723	0
	46s	0	-12.617	139.7647	2.858737953	1.1707372
	47N	50	-12.5552	139.8222		
	47N	40	-12.2201	139.6926		
	47N	30	-12.597	139.6598		
	47N	20	-12.597	139.6598		
	47N	10	-12.597	139.6598		
	47N	0	-12.6444	139.6609		

Table A Continued

Pair	Ppoint	Timestep	lat	lon	Distance Total	Δ Distance
47NW, 42E	47NW	50	-12.3881	139.4367	4.66505835	0
	47NW	40	-12.3865	139.3069	1.350551513	-3.3145068
	47NW	30	-12.7086	139.2534	2.348760738	0.9982092
	47NW	20	-12.7086	139.2534	2.348760738	0
	47NW	10	-12.7086	139.2534	2.348760738	0
	47NW	0	-12.7689	139.2584	1.452828261	-0.8959325
	42E	50	-12.4315	139.2671		
	42E	40	-12.4256	139.2757		
	42E	30	-12.7808	139.2051		
	42E	20	-12.7808	139.2051		
	42E	10	-12.7808	139.2051		
	42E	0	-12.7808	139.2051		
42W, 41E	42W	50	-12.5447	138.5994	1.315896315	0
	42W	40	-12.9553	138.8694	0.664133824	-0.6517625
	42W	30	-13.265	138.7423	1.252458445	0.5883246
	42W	20	-13.265	138.7423	1.252458445	0
	42W	10	-13.265	138.7423	1.252458445	0
	42W	0	-13.265	138.7423	1.252458445	0
	41E	50	-12.5228	138.5553		
	41E	40	-12.9561	138.8444		
	41E	30	-13.2427	138.701		
	41E	20	-13.2427	138.701		
	41E	10	-13.2427	138.701		
	41E	0	-13.2427	138.701		

Table A Continued

Pair	Ppoint	Timestep	lat	lon	Distance Total	Δ Distance
39s, 41N	39s	50	-12.4489	138.2293	2.092035219	
	39s	40	-13.16	138.4314	3.575485433	1.4834502
	39s	30	-13.16	138.4314	7.515547374	3.9400619
	39s	20	-13.16	138.4314	7.515547374	0
	39s	10	-13.16	138.4314	7.515547374	0
	39s	0	-13.16	138.4314	7.515547374	0
	41N	50	-12.519	138.1972		
	41N	40	-13.1758	138.5652		
	41N	30	-13.4342	138.4004		
	41N	20	-13.4342	138.4004		
	41N	10	-13.4342	138.4004		
	41N	0	-13.4342	138.4004		
41sw, 63N	41sw	50	-13.3482	137.6273	0.6723539	0
	41sw	40	-14.1687	138.6691	26.4000832	25.727729
	41sw	30	-14.4322	138.4018	23.40511269	-2.9949705
	41sw	20	-14.4322	138.4018	23.40511269	0
	41sw	10	-14.4322	138.4018	23.40511269	0
	41sw	0	-14.4322	138.4018	23.40511269	0
	63N	50	-13.351	137.6021		
	63N	40	-13.8939	137.7113		
	63N	30	-13.8939	137.7113		
	63N	20	-13.8939	137.7113		
	63N	10	-13.8939	137.7113		
	63N	0	-13.8939	137.7113		

Table A Continued

Pair	Ppoint	Timestep	lat	lon	Distance Total	Δ Distance
41se,57N	41SE	50	-13.9196	138.2844	0.574824956	0
	41SE	40	-14.1999	139.5524	14.50910586	13.934281
	41SE	30	-14.5489	139.2786	13.57102697	-0.9380789
	41SE	20	-14.5489	139.2786	13.57102697	0
	41SE	10	-14.5489	139.2786	13.57102697	0
	41SE	0	-14.5489	139.2786	13.57102697	0
	57N	50	-13.9406	138.2823		
	57N	40	-14.5377	139.1274		
	57N	30	-14.8401	138.8608		
	57N	20	-14.8401	138.8608		
	57N	10	-14.8401	138.8608		
	57N	0	-14.8401	138.8608		
63s, 64N	63s	50	-13.4651	137.5094	0.261425798	0
	63s	40	-14.0391	137.7203	3.645675552	3.3842498
	63s	30	-14.0391	137.7203	3.645675552	0
	63s	20	-14.0391	137.7203	3.645675552	0
	63s	10	-14.0391	137.7203	3.645675552	0
	63s	0	-14.0391	137.7203	3.645675552	0
	64N	50	-13.4711	137.5017		
	64N	40	-14.1401	137.6298		
	64N	30	-14.1401	137.6298		

Table A Continued

Pair	Ppoint	Timestep	lat	lon	Distance Total	Δ Distance
	64N	20	-14.1401	137.6298		
	64N		-14.1401	137.6298		
	64N	0	-14.1401	137.6298		
64s, 65N	65N	50	-13.5816	137.4243	1.638965044	0
	65N	40	-14.3075	137.5931	2.698556088	1.059591
	65N	30	-14.3075	137.5931	2.698556088	0
	65N	20	-14.3075	137.5931	2.698556088	0
	65N	10	-14.3075	137.5931	2.698556088	0
	65N	0	-14.3075	137.5931	2.698556088	0
	64s	50	-13.5362	137.4649		
	64s	40	-14.2143	137.6277		
	64s	30	-14.2143	137.6277		
	64s	20	-14.2143	137.6277		
	64s	10	-14.2143	137.6277		
	64s	0	-14.2143	137.6277		
65s, 66N	65s	50	-13.7809	137.3022	1.290458811	0
	65s	40	-14.5387	137.6126	3.102909653	1.8124508
	65s	30	-14.5387	137.6126	3.102909653	0
	65s	20	-14.5387	137.6126	3.102909653	0
	65s	10	-14.5387	137.6126	3.102909653	0
	65s	0	-14.5387	137.6126	3.102909653	0

Table A Continued

Pair	Ppoint	Timestep	lat	lon	Distance Total	Δ Distance
	66N	50	-13.827	137.291		
	66N	40	-14.6525	137.6079		
	66N	30	-14.6525	137.6079		
	66N	20	-14.6525	137.6079		
	66N	10	-14.6525	137.6079		
	66N	0	-14.6525	137.6079		
60s, 62N	60s	50	-13.6666	137.7262	0.383533179	0
	60s	40	-14.2568	138.3386	5.026958589	4.6434254
	60s	30	-14.5441	138.1984	5.458632659	0.4316741
	60s	20	-14.5441	138.1984	5.458632659	0
	60s	10	-14.5441	138.1984	5.458632659	0
	60s	0	-14.5441	138.1984	5.458632659	0
	62N	50	-13.678	137.7177		
	62N	40	-14.1807	138.1652		
	62N	30	-14.4068	138.0477		
	62N	20	-14.4068	138.0477		
	62N	10	-14.4068	138.0477		
	62N	0	-14.4068	138.0477		
57s, 58N	57s	50	-14.0697	138.27	2.864590586	0
	57s	40	-14.6668	139.1157	13.06153644	10.196946
	57s	30	-14.9648	138.8974	6.924878705	-6.1366577
	57s	20	-14.9648	138.8974	6.924878705	0

Table A Continued

Pair	Ppoint	Timestep	lat	lon	Distance Total	Δ Distance
	57s	10	-14.9648	138.8974	6.924878705	0
	57s	0	-14.9648	138.8974	6.924878705	0
	58N	50	-14.1552	138.3331		
	58N	40	-14.8601	138.662		
	58N	30	-15.1114	138.6824		
	58N	20	-15.1114	138.6824		
	58N	10	-15.1114	138.6824		
	58N	0	-15.1114	138.6824		
58s, 59n	58s	50	-14.3651	138.3281	1.077278152	0
	58s	40	-15.07	138.6616	2.234680929	1.1574028
	58s	30	-15.3211	138.6919	2.281100932	0.04642
	58s	20	-15.3211	138.6919	2.281100932	0
	58s	10	-15.3211	138.6919	2.281100932	0
	58s	0	-15.3211	138.6919	2.281100932	0
	59N	50	-14.4044	138.3326		
	59N	40	-15.0638	138.5769		
	59N	30	-15.2698	138.6233		
	59N	20	-15.2698	138.6233		
	59N	10	-15.2698	138.6233		
	59N	0	-15.2698	138.6233		
58NE, 56s	58ne	50	-14.7236	139.2555	1.77154684	0

Table A Continued

Pair	Ppoint	Timestep	lat	lon	Distance Total	Δ Distance
	58ne	40	-15.4091	139.5999	4.482065626	2.7105188
	58ne	30	-15.6185	139.6463	3.621155263	-0.8609104
	58ne	20	-15.6185	139.6463	3.621155263	0
	58ne	10	-15.6185	139.6463	3.621155263	0
	58ne	0	-15.6185	139.6463	3.621155263	0
	56s	50	-14.6841	139.3089		
	56s	40	-15.4927	139.7469		
	56s	30	-15.6701	139.7735		
	56s	20	-15.6701	139.7735		
	56s	10	-15.6701	139.7735		
	56s	0	-15.6701	139.7735		
56N, 82s	56n	50	-14.1709	139.5289	6.036913728	0
	56n	40	-14.9558	139.8955	2.99418503	-3.0427287
	56n	30	-15.13	139.9091	5.15431427	2.1601292
	56n	20	-15.13	139.9091	5.15431427	0
	56n	10	-15.13	139.9091	5.15431427	0
	56n	0	-15.13	139.9091	2.523466171	-2.6308481
	82s	50	-13.9614	139.6033		
	82s	40	-14.8459	139.8953		
	82s	30	-14.9425	139.9352		
	82s	20	-14.9425	139.9352		
	82s	10	-14.9425	139.9352		

Table A Continued

Pair	Ppoint	Timestep	lat	lon	Distance Total	Δ Distance
	82s	0	-15.0377	139.9011		
71s, 74N	71s	50	-14.6487	137.5057	0.711466011	
	71s	40	-15.468	137.8383	8.231600963	7.520135
	71s	30	-15.5524	137.8663	5.817839804	-2.4137612
	71s	20	-15.5524	137.8663	5.817839804	0
	71s	10	-15.5524	137.8663	5.817839804	0
	71s	0	-15.5524	137.8663	5.817839804	0
	74N	50	-14.6737	137.5135		
	74N	40	-15.757	137.9298		
	74N	30	-15.757	137.9298		
	74N	20	-15.757	137.9298		
	74N	10	-15.757	137.9298		
	74N	0	-15.757	137.9298		
13, 10s	13W	50	-14.8007	136.1096	0.734598004	0
	13W	40	-14.9967	136.0491	5.640286923	4.9056889
	13W	30	-14.9967	136.0491	6.182834139	0.5425472
	13W	20	-14.7226	135.9509	5.639989349	-0.5428448
	13W	10	-14.7226	135.9509	5.639989349	0
	13W	0	-14.7226	135.9509	5.639989349	0
	10S	50	-14.7923	136.0831		
	10S	40	-14.7923	136.0831		
	10S	30	-14.7698	136.0448		
	10S	20	-14.5178	135.9821		

Table A Continued

Pair	Ppoint	Timestep	lat	lon	Distance Total	Δ Distance
	10S	10	-14.5178	135.9821		
	10S	0	-14.5178	135.9821		
7E, 8W	7E	50	-11.4092	136.2733	1.293936972	0
	7E	40	-11.4092	136.2733	1.293936972	0
	7E	30	-11.4092	136.2733	1.293936972	0
	7E	20	-11.4092	136.2733	1.293936972	0
	7E	10	-11.2342	136.2776	5.760071912	4.4661349
	7E	0	-11.2342	136.2776	5.760071912	0
	8w	50	-11.4437	136.3066		
	8w	40	-11.4437	136.3066		
	8w	30	-11.4437	136.3066		
	8w	20	-11.4437	136.3066		
	8w	10	-11.4437	136.3066		
	8w	0	-11.4437	136.3066		
2W, 6E	2w	50	-12.0697	135.5115	0.286940951	0
	2w	40	-12.0957	135.4897	1.548965639	1.2620247
	2w	30	-12.0961	135.5125	0.745603123	-0.8033625
	2w	20	-12.0984	135.5169	1.08255338	0.3369503
	2w	10	-12.0281	135.385	7.246405327	6.1638519
	2w	0	-12.0281	135.385	7.246405327	0

Table A Continued

Pair	Ppoint	Timestep	lat	lon	Distance Total	Δ Distance
	6E	50	-12.0593	135.5132		
	6E	40	-12.0454	135.5168		
	6E	30	-12.069	135.5164		
	6E	20	-12.0667	135.5414		
	6E	10	-11.803	135.5298		
	6E	0	-11.803	135.5298		
41EE, 48W	41EE	0	-13.4117	138.5628	0.376533153	0
	41EE	40	-13.6364	139.4324	2.171622852	1.7950897
	41EE	30	-13.9766	139.2171	0.601543887	-1.570079
	41EE	20	-13.9766	139.2171	0.601543887	0
	41EE	10	-13.9766	139.2171	0.601543887	0
	41EE	0	-13.9766	139.2171	3.129273519	2.5277296
	48W	50	-13.41	138.5769		
	48W	40	-13.6958	139.4871		
	48W	30	-13.9983	139.2213		
	48W	20	-13.9983	139.2213		
	48W	10	-13.9983	139.2213		
	48W	0	-14.0736	139.2805		
73N, 74s	73N	50	-14.9827	137.5173	3.703192717	
	73N	40	-16.1079	137.829	5.484692786	1.7815001
	73N	30	-16.1079	137.829	5.484692786	0
	73N	20	-16.1079	137.829	5.484692786	0

Table A Continued

Pair	Ppoint	Timestep	lat	lon	Distance Total	Δ Distance
	73N	10	-16.1079	137.829	5.484692786	0
	73N	0	-16.1079	137.829	5.484692786	0
	74s	50	-14.8491	137.4914		
	74s	40	-15.9336	137.9338		
	74s	30	-15.9336	137.9338		
	74s	20	-15.9336	137.9338		
	74s	10	-15.9336	137.9338		
	74s	0	-15.9336	137.9338		
73n, 74s	73n	50	-14.9827	137.5173	3.703192717	0
	73n	40	-16.1079	137.829	5.484692786	1.7815001
	73n	30	-16.1079	137.829	5.484692786	0
	73n	20	-16.1079	137.829	5.484692786	0
	73n	10	-16.1079	137.829	5.484692786	0
	73n	0	-16.1079	137.829	5.484692786	0
	74s	50	-14.8491	137.4914		
	74s	40	-15.9336	137.9338		
	74s	30	-15.9336	137.9338		
	74s	20	-15.9336	137.9338		
	74s	10	-15.9336	137.9338		
	74s	0	-15.9336	137.9338		

Table A Continued

Pair	Ppoint	Timestep	lat	lon	Distance Total	Δ Distance
66s, 68N	66s	50	-14.1693	137.3386	0.743538954	0
	66s	40	-14.9519	137.7862	3.308870674	2.5653317
	66s	30	-14.9519	137.7862	3.308870674	0
	66s	20	-14.9519	137.7862	3.308870674	0
	66s	10	-14.9519	137.7862	3.308870674	0
	66s	0	-14.9519	137.7862	3.308870674	0
	68N	50	-14.1965	137.3409		
	68N	40	-15.072	137.7675		
	68N	30	-15.072	137.7675		
	68N	20	-15.072	137.7675		
	68N	10	-15.072	137.7675		
	68N	0	-15.072	137.7675		
66W, 69N	66W	50	-14.2247	137.0025	1.382412707	00
	66W	40	-15.1266	137.4958	8.993948272	7.6115356
	66W	30	-15.1266	137.4958	8.993948272	0
	66W	20	-15.1266	137.4958	8.993948272	0
	66W	10	-15.1266	137.4958	8.993948272	0
	66W	0	-15.1266	137.4958	8.993948272	0
	69N	50	-14.2658	136.9718		
	69N	40	-15.4491	137.4227		
	69N	30	-15.4491	137.4227		
	69N	20	-15.4491	137.4227		
	69N	10	-15.4491	137.4227		

Table A Continued

Pair	Ppoint	Timestep	lat	lon	Distance Total	Δ Distance
	69N	0	-15.4491	137.4227		
69s, 70N	69s	50	-14.3617	136.9231	2.277008096	0
	69s	40	-15.5495	137.3844	4.970167278	2.6931592
	69s	30	-15.5495	137.3844	4.041902829	-0.9282644
	69s	20	-15.5495	137.3844	4.041902829	0
	69s	10	-15.5495	137.3844	4.041902829	0
	69s	0	-15.5495	137.3844	4.041902829	0
	70N	50	-14.3776	137.0078	23.22518869	
	70N	40	-15.7319	137.3877	57.82132253	
	70N	30	-15.6805	137.4567	58.09493376	
	70N	20	-15.6805	137.4567	65.56820931	
	70N	10	-15.6805	137.4567	65.56820931	
	70N	0	-15.6805	137.4567	65.56820931	
					0	
10, 9	10	50	-13.8996	136.2799	1.222933161	0
		40	-13.8996	136.2799	1.222933161	0
		30	-13.8834	136.2696	1.032871813	-0.1900613
		20	-13.6227	136.1667	7.331082065	6.2982103
		10	-13.6227	136.1667	7.331082065	0
		0	-13.6227	136.1667	7.331082065	0
	9	50	-13.8589	136.2994	3666.596677	

Table A Continued

Pair	Ppoint	Timestep	lat	lon	Distance Total	Δ Distance
		40	-13.8589	136.2994	3666.596677	
		30	-13.8589	136.2994	3666.596677	
		20	-13.8589	136.2994	3666.596677	
		10	-13.8589	136.2994	3666.596677	
		0	-13.8589	136.2994	3666.596677	

Table B: *Table of band measurements that surround the CF. Measurements were conducted with the GPlates "Measurement tool".*

CF Bands	Width (km)	Avg for each (km)	Length (km)	Area ($km^{2)}$
1	5.4707	5.57	58	322.9614
	6.201			
	5.0332			
2	4.842	5.06	20.1	101.6551
	6.0706			
	4.2598			
3	4.4191	5.16	31.14	160.7623
	5.0269			
	6.0417			
4	2.9173	3.62	22.83	82.74734
	3.476			
	4.4802			
5	2.7105	3.45	14.61	50.40645
	3.0397			
	4.6002			
6	9.1618	8.21	18.03	148.057
	8.014			
	7.4593			
7	2.3716	2.76	12.91	35.68238
	2.3671			
	3.5531			
8	2.8373	2.85	17.1	48.70137
	1.7596			
	3.9472			0
9	4.9295	5.89	34.4	202.7754
	6.7447			
	6.0097			

Table C: *Table of missing surface area calculation for interior of CF. These measurements were calculated by the summation of smaller rectangles within the gaps of the CF at t = -50.*

L (km)	W (km)	Area (km^2)
33.2103	2.35	78.04421
15.5	1.2	18.6
12.2	2.5	30.5
3.2	1.3	4.16
14.4	3.3	47.52
7.6	4.7	35.72
	Total	214.5442

VITA

Chad Melton was born in Dallas, TX September 15, 1978 and was raised in Cleveland, TN. After 13 years as a professional touring and teaching musician, Chad returned to the University of Tennessee to in Jan of 2013 to study geology and planetary sciences. Chad graduated the University of Tennessee with a B.S. in Geology and Environmental Sciences in August of 2016 and a M.S. in August of 2018. Chad accepted a post-masters position in UAV remote sensing at Oak Ridge National Lab.